Human Blood-Related Diseases Investigated by High Speed and High Resolution Fluorescence Microscopy

By

DEANNA LYNN WOLFSON

B.S. (Physics, Worcester Polytechnic Institute) 2006

M.S. (Applied Science, University of California, Davis) 2008

DISSERTATION

Submitted in partial satisfaction of the requirements for the degree of

DOCTOR OF PHILOSOPHY

in

BIOPHYSICS

in the

OFFICE OF GRADUATE STUDIES

of the

UNIVERSITY OF CALIFORNIA

DAVIS

Approved:

Dr. Thomas Huser

Dr. Sebastian Wachsmann-Hogiu

Dr. Satya Dandekar

Committee in Charge

2013

ProQuest LLC.
789 East Eisenhower Parkway
P.O. Box 1346
Ann Arbor, MI 48106 - 1346

Acknowledgements

Creativity, and thus the ability to connect the dots between the pages of books in entirely different libraries, can be developed through the encouragement to think and to be different. Not only did my mother accept who I was (astronomical stubbornness aside), but for as long as I can remember she actively encouraged and demonstrated creativity, as well as instilled in me a love of reading and critical thinking. I credit my objectivity to my father, the chief scientist in the family. Although I hated hearing it growing up, one of the greatest lessons he taught me is that “Life is not fair.” From this, I learned to accept that which I cannot change, and to work with what I was given. Between him, my mother, and MacGyver, I developed the skills necessary to build a parachute from a pack of chewing gum and a staple remover, rather than simply giving up when found in a bad situation. To my brother: Thank you for making sure the gum and staple remover were always there when I needed them, without ever having to ask. To my sister: Every time my ill-conceived parachute has failed, you have been right there to (first laugh at me and then) pick me up, reassure me that I’m still awesome, and threaten the gum manufacturer for making a faulty product. You too are awesome. To my cats: Thank you for letting me take care of you, and for all of your ‘help’ while I was typing.

Family extends beyond simple genetics, and I am grateful for the love and support from those who, despite the lack of shared DNA, have always treated me as family. To Alice, Emily, Lydia, Bob, and Arlette; Claire; and Steve and Cyndi: Thank you for teaching me to not let obstacles get in my way, to understand that there is more than

one way to define success, and to enjoy life no matter how it is given to me. To my boyfriend: Thank you for believing in me, and for teaching me to believe in myself.

As my family has prepared me to go into the world as an adult, the Center for Biophotonics Science and Technology (CBST) has prepared me for life as a scientist. Some of my greatest joy in science comes from bringing technologies and concepts from one field, and combining or applying them to another in order to solve a problem. Not only was I fortunate to have access to powerful techniques and stable funding through CBST, but I was also given the flexibility to work on a variety of projects in collaboration with many outstanding scientists and physicians. I have learned much from each of them, and will actively seek to include in my career the same type of balanced, interdisciplinary sharing of skills and expertise I experienced as a graduate student at CBST.

I owe a debt of gratitude to all those who have helped me over the years, including my professors, fellow graduate students, postdocs, undergraduates, administrative staff, friends, family, and many more, but there are several individuals to whom I am especially indebted. In particular, I would like to thank Dr. Gregory McNerney, for showing me the ropes of the lab and the disc golf course; Dr. Benjamin Dale, for my HIV training; Dr. Balpreet Ahluwalia, for his collaboration and esteem; and Ana Popovich, for all of her hard work and trust. To Dr. Frank Chuang, who first introduced me to CBST: Thank you for taking the time to teach me not only the practical aspects of developing a new research program, but also how to balance a career as a scientist with a life beyond work. To Dr. Sebastian Wachsmann-Hogiu, who taught me the fundamentals of biophotonics and continues to be a valuable source of wisdom:

Thank you for sharing your knowledge and insight, for guiding me in my academics and research, and for challenging me to always understand several levels beyond what I think I need to know. Thank you for keeping your expectations high, and for helping me to continuously aim higher. Finally, to my advisor, Dr. Thomas Huser: Thank you for everything. It has been a privilege to work with you, and I know the many lessons I have learned will stay with me throughout my career. I admire your breadth of knowledge and how elegantly you apply it across disciplines, and am further impressed that the same person can also be so incredibly generous and kind-hearted. You have not only provided support and guidance, but exemplified the type of scientist I aspire to be.

Abstract

A major hurdle in health research is to not just identify disease components, but identify how they work together dynamically. Recent developments in optical microscopy now allow for high speed, high resolution, and multicolor imaging of live cells which can be used to better understand these interactions. The work here shows advances in both human immunodeficiency virus (HIV) and red blood cell (RBC) research enabled by novel combinations of optical imaging techniques.

It was previously believed that productive infection of HIV occurred only when the viral core entered the cell after fusion of the viral membrane with the plasma membrane. By using live, multicolor, 3D imaging from a spinning disk confocal microscope (SDCM) and flow cytometry, an alternative entry pathway has been demonstrated: rather than fuse directly with the plasma membrane, HIV particles entering cells through a virological synapse first undergo endocytosis, and then must mature before they can release their core into the cytoplasm through fusion with the endosomal membrane. This entry method offers some protection from neutralizing antibodies, and has significant implications for targeted therapies.

While important, the low throughput of imaging single transfer events inspired the development of a new microscope designed to initiate more cellular interactions. Optical tweezers are capable of precisely trapping and moving cells in suspension, but previous implementations did not allow trapped objects to be imaged in 3D. The system described here combines a SDCM with feedback-sensitive holographic optical tweezers (HOT), allowing multiple independently-controlled objects to be simultaneously trapped and imaged in 3D.

Besides increasing experimental throughput, the SDCM-HOT system is a powerful tool for studying the direct effects of trapping on cells. Contrary to studies using 2D imaging methods, SDCM-HOT data shows that RBCs in optical traps are simply rotated, rather than folded in half. Furthermore, these experiments led to the discovery that the most prevalent shape of healthy RBCs in suspension is a bowl, rather than donut shape, and common cell preparation techniques caused significant cellular deformations. With additional research, this technique shows potential for both basic discovery and for identifying disease states, such as malaria or anemia.

Video captions

Video 7.1 3D rendering of SIM image of HIV transfer to actin-labeled cells. HIV (GFP-Gag, green) is transferred simultaneously through two virological synapses. Viral particles are visible both inside and outside the actin (red) cytoskeleton.

Video 7.2 3D rendering of SIM image of HIV transfer to a cell with an oppositely polarized MTOC. . HIV (GFP-Gag, green) is transferred across a virological synapse to a donor cell. Although the microtubule bundle (tubulin, red) is directly opposite the virological synapse, this is not representative of the bulk data. Most studies have shown the MTOC to preferentially polarize towards the synapse.

Video 7.3 3D rendering of SIM image of HIV transfer through an elongated cell. In addition to forming synapses with its closest neighbors, HIV-infected cells have been observed to occasionally form elongated connections with cells up to 100 μm away. This video shows both examples, as an HIV-infected cell simultaneously transfers viral material (GFP-Gag, green) to both a nearby cell and to a target cell approximately 30

μm away. The infected cell can be visualized by its tubulin (red), which stretches the full distance between cells.

Video 7.4 3D rendering of SIM image of HIV transfer to tubulin-labeled cells. HIV (GFP-Gag, green) is transferred simultaneously through two virological synapses. In one cell the microtubule bundle (tubulin, red) is polarized towards the synapse, while the other cell is ambiguous.

Video 8.1 RBCs imaged in brightfield appear to narrow while being optically trapped, but return to normal when released. Paraformaldehyde-fixed RBCs are optically trapped, moved within the field of view, and then released. Although in 2D it appears as though the cells are folding, in reality they are simply realigning such that their narrower profile faces the camera. Cells about to be trapped are indicated with arrows and all cells are released at approximately 33 seconds. Increased relative playback speed is indicated by the text in the lower right corner.

Video 8.2 An RBC appears as a 'bowl' shape in 3D. A DiI-labeled red blood cell resting on a coverslip is first imaged, and then rendered in 3D. Approximately 75% of resting RBCs take this form.

Video 8.3 An RBC appears as a 'donut' shape in 3D. A DiI-labeled red blood cell resting on a coverslip is first imaged, and then rendered in 3D. Approximately 25% of resting RBCs take this shape.

Video 8.4 A trapped RBC appears as a 'shell' shape in 3D. An optically-trapped RBC is first imaged using autofluorescence, and then rendered in 3D.

Table of Contents

Chapter 1 Introduction

Optical techniques are by their very nature one of the original techniques used to diagnose human ailments; even our primitive ancestors could look at a broken bone or bloody wound to determine they were injured. Modern techniques, such as the staining and microscopic imaging of suspected cancer tissue by pathologists, are far more sophisticated, but still rely significantly on optical evaluation. Visual inputs are used in a myriad of human evaluations required for every day decisions, so their familiar and trusted nature makes them easily adaptable to diagnostic and research settings.

While modern medicine can cure many ailments, there are major diseases whose mechanisms are unknown, there is no cure, and often times only a few of the symptoms can be treated. Proteomics and genetics have become popular tools for diagnostics and basic research in medicine, including cancer research and research into human immunodeficiency virus (HIV) infection, but they only give a snapshot of a system at a single time point. Although these techniques are useful for understanding the components of disease, they are unable to demonstrate how many parts of a system interact in time.

In the late 1950's, two discoveries were made that, although they didn't appear to be useful at the time, revolutionized science and medicine. First, luminescence in a lowly form of sea creature was reported in 1955 [4], followed by the invention of the optical laser in 1958 [5]. Green fluorescent protein (GFP), originally from jellyfish, is now a key component of many live and fixed biological experiments, ranging from labeling intracellular components to the engineering of green fluorescent puppies whose color can be chemically switched on and off [6]. The laser is now a critical component in a

multitude of techniques, including laser eye surgery, atomic force microscopy, and, of course, optical microscopy. Although each advance is powerful on its own, combining techniques amplifies the influence far beyond the sum of the parts. Optical microscopy, especially live-cell imaging, can be used to move beyond simply identifying individual disease components and towards understanding the dynamic and complex interactions within biological systems.

Thirty years ago, HIV was identified as the causative, infectious agent of acquired immunodeficiency syndrome (AIDS). In 1987 azidothymidine (AZT) became the first drug approved for use in treating HIV by the FDA [7], and it is still in use today in combination with other HIV medications. Despite the quarter-century since then, there is still no cure for HIV and the most successful vaccine tested showed only ~30% efficacy [8]. While several features of the virus, including a high mutation rate, make vaccine development difficult, a bigger problem may be a lack of understanding of how the virus interacts with its host.

Fundamental mechanisms of HIV infection are still actively being discovered. Less than 10 years ago, HIV was thought to infect new cells primarily as a cell-free virus. Cell-to-cell transfer had been proposed by 1992 [9], but the characterization of this process through a 'virological synapse' did not occur until the early 2000's [10-15]. Since then, it's been shown to be 3-4 orders of magnitude more efficient than cell-free methods [16-18]. Furthermore, because of the virus's characterization as being pH-independent [19], it was assumed to productively infect cells only via plasma membrane fusion [17, 20, 21]. In the past five years, evidence (including that in Chapter 6, [3]) has been emerging that cellular entry by endocytosis is a viable route, and possibly even the

favored pathway [16, 19, 21-25]. This research has significant implications towards the development of targeted anti-HIV therapies, much of which was enabled through optical microscopy techniques.

Red blood cell (RBC)-related health also has several needs that can be addressed using optical techniques. Recently there has been increasing interest on evaluating transfusion blood to enhance patient outcomes [26, 27]. Red blood cells live up to 120 days in their originating body [28], but circulating blood is a mix of old, new, and middle-aged cells. When the stresses of harvesting and preserving donated blood are added to the duration of storage prior to transfusion, the effective average RBC age is increased and function decreased, resulting in a loss of up to 30% of transfused cells within a few hours of patient transfusion [29]. Although not all studies have shown statistically significance in patient outcomes, differences have been noted in several specialties [30], such as cardiac surgery [31].

The aging of RBCs has been strongly linked to cell deformability, which depends on the membrane composition, surface to volume ratio, and density of hemoglobin [29]. Although deformability can be directly measured using micropipette aspiration, this technique is time- and labor-intensive, and not suited to high-throughput applications. A much better alternative is optical trapping, where a cell is trapped and deformed using one or more tightly focused lasers. This technique has already been used to investigate many different aspects of RBC deformability [32-35], and is adaptable to both high throughput and multimodal techniques. By using holographic optical tweezers, which allow the generation and manipulation of many concurrent optical traps, multiple cells

can be simultaneously evaluated, and cells can be held stably in microfluidic-derived flow conditions or dragged to create an artificial flow velocity by the tweezers.

Optical trapping not only has potential for helping to evaluate the integrity of stored blood samples for transfusion, but also for studying both healthy and diseased cell states. RBC shape is linked to cell health for stored blood [29], cellular age [28], and genetic diseases such as sickle cell anemia. In Chapter 8, the utility of combining optical trapping with 3D imaging becomes apparent with previously inaccessible analysis of RBC shape, which can easily be expanded to evaluate diseased cell states.

In summary, optical techniques are highly relevant to both basic research and diagnostic applications. Advances enabled by these techniques, a few of which are discussed in this work, have the potential to save billions to trillions of dollars in health care costs, as well as millions of lives and countless hours of patient suffering.

Chapter 2 Biology of selected blood-related systems

2.1 Human immunodeficiency virus

Human immunodeficiency virus (HIV) is the retrovirus responsible for causing acquired immunodeficiency syndrome (AIDS). There are approximately 34 million adults in the world currently living with HIV, with 1.7 million deaths and another 2.5 million new infections each year. Although the new infection rate has decreased 20% overall in the last decade, some areas including northern Africa and the middle east have experienced climbs in new infection rates [36]. Education and medications have helped combat the spread of HIV, but the most successful vaccine to date had only ~30% efficacy [8]. The low efficacy appears to be caused by structural differences in a viral protein critical to binding to and infecting new cells [37], so the goal of smarter and more effective designs should be supported by additional research on the viral-cellular interaction. As HIV-1 is the predominant form of HIV worldwide, it is the focus of the following research.

Host infection

HIV is transferred between hosts through bodily fluid, including blood, breast milk, and semen. It can be transferred as free virus, such as in blood plasma, within infected cells, or in both forms [20]. The risk of contracting HIV depends on many factors, including the infection stage of the host, variations of the virus itself, and the transmission method. Transfusions with infected blood are more than 90% likely to cause infections in the recipient, but most types of sexual intercourse with an infected person have less than a 1% risk of infection [20].

The majority of people develop flu-like symptoms 1-4 weeks after their initial infection, during the acute phase [20, 38]. The appearance of anti-HIV antibodies signals the beginning of the ‘primary’ or ‘early’ stage of infection, during which the amount of circulating virus is reduced to a viral set point. Typically, but not always, this is followed by a long latency period that lasts months to years [39].

During the acute stage of infection, production of CD8+ T (white blood) cells is significantly increased, CD4+ T cells are depleted, and large amounts of HIV can be found circulating in the blood. Relatively lower levels of viral production during this period, compared person-to-person through blood tests, are correlated with a longer time before onset of AIDS [20]. This has also been shown to be true in gut-associated lymphoid tissue (GALT) [38, 40]. GALT is of particular interest to HIV research as it is an early target of infection, acts as a viral ‘reservoir’ during the latency stage [38, 41], and often fails to recover from CD4+ T cell depletion even when circulating CD4+ T cell levels improve [41, 42].

Both dendritic cells and T cells can be infected with HIV. Dendritic cells located near the point of viral entry, such as in the vagina, are typically considered to be the initial targets of HIV. These cells are susceptible to both the CCR5-binding (R5) and CXCR4-binding (X4) variants of HIV, which allows them to be both receptive to the more prevalent R5 in initial infection, and help ramp up production of X4 in the early stage. Long term, the major targets of HIV infection are CD4+ T lymphocytes, in both the gut and elsewhere. While only a subset of these is susceptible to R5, all CD4+ T cells can be infected with X4-HIV. During acute infection, >90% of productively infected cells are the R5-susceptible resting memory T cells, which can live up to 2 weeks while

producing new virus. Activated T cells produce virus approximately 5 times faster, but die within a day or two [39]. Significant depletion of CD4+ T cells results in immunodeficiency, and AIDS patients become highly susceptible to diseases that a healthy individual could otherwise survive.

Viral replication and transfer

HIV-1 hijacks the host cell's own replication machinery to produce new viral proteins. These proteins then accumulate at the plasma membrane of the cell before budding off into individual, immature virions 100-130 nm in diameter [2, 20, 43]. A lipid membrane obtained from the host cell supports the envelope (Env) proteins gp120 (the protein of interest in the vaccine trial mentioned above [37]) and gp41. Viral protease (PR) cleaves the structural Gag protein into three main components: the membrane-supporting matrix (MA), the conical-shaped viral capsid (CA) and the RNA-bound nucleocapsid (NC) protein (see Figure 2.1). When in contact with a target cell, gp120 binds to and induces a conformational change in CD4 on the cell surface, exposing binding sites for coreceptors such as CCR5 or CXCR4 [21, 44, 45]. The mature virion then either enters the cell through endocytosis and undergoes fusion (described further in Chapter 6, [3]) or fuses at the cell membrane [14, 20], releasing the capsid and its contents (collectively called the core) into the cytoplasm. Partial capsid disassembly and reverse transcription of the RNA into double-stranded DNA lead to the formation of the 56 nm preintegration complex (PIC) [46]. There, the viral protein integrase (IN) incorporates the viral genome into the host's, leading to the eventual production of new virions. Additional 'helper' viral proteins Vif, Vpr, Tat, Rev, Vpu, and Nef support the

replication and infection cycle, but not all are always necessary for productive infection or virion formation [20, 22].

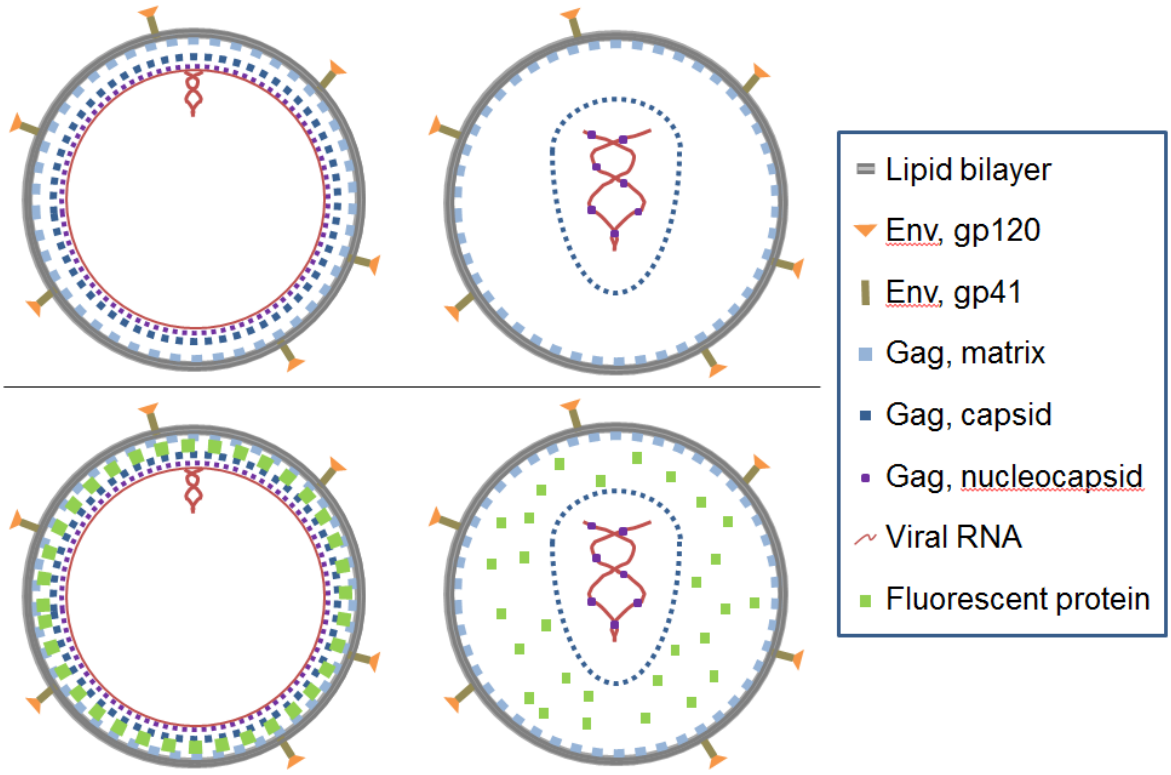

Figure 2.1 Structure of HIV. HIV assembles at the surface of its host cell before budding off as an immature virion (left). GFP (bottom) can be encoded into the Gag protein, so when the virus matures (right) it will be cleaved along with the separate parts of Gag. Although no longer bound directly, GFP is physically constrained between the matrix and capsid substructures until viral fusion occurs [1, 2].

Historically, emphasis has been placed on cell-free viral particles when examining HIV-1 infection, particularly from a pathological point of view [20, 47, 48], but research has shown there are far more viruses in infected cells in the body than there are free viruses in the blood [20]. Additionally, cell-cell infection routes are estimated to be anywhere from 5 to 18,000 times more effective than cell-free methods [17, 49, 50], potentially due to protection from neutralizing antibodies [50, 51]. Consequently, much more research now focuses on viral spread through direct cell-cell contact via cellular

protrusions such as nanotubes or synapses. The first reported transfer of HIV in this nature was between an infected dendritic cell and an uninfected T cell [52], but the term *virological synapse* refers more generally to the stable, adhesive point of contact used to transfer virus between an infected cell to an uninfected cell [50]. Viral transmission through the synapse is facilitated by a higher concentration of CD4 and viral co-receptors [50], and by increased cytoskeletal dynamics [12, 13, 15]. The virological synapse has some similarities to the commonly observed immunological synapse between antigen-presenting cells and lymphocytes, including some adhesion molecules like LFA-1, ICAM, and talin [13, 14] and the maintenance of independent membranes [13], but also includes a number of viral proteins [12, 50, 53-56], is less structured [14], and involves different cellular behavior [50].

Electron and fluorescence microscopy have both shown preferential, but non-exclusive, budding of HIV-1 virions at the synapse [55]. Both fusion at the plasma membrane [44, 57] and endocytic uptake [22, 24, 58] have been shown with HIV-1 virions, and the path to productive infection of a target cell likely varies with cell type and possibly with viral strain. Typically, pH-independent viruses have been seen to enter cells through fusion with the cell membrane and pH-dependent viruses enter through endocytosis followed by fusion with the endosome [19]. Because HIV-1 was early on characterized as pH-independent [19], it historically was assumed to infect via plasma membrane fusion [17, 20, 21]. Although multiple groups testing both pathways failed to see productive infection via endocytosis [57, 58], others have recently had more success in demonstrating this route. In one study, Miyauchi, et.al., directly compared the entry pathways and found that only endocytic pathways were productive, and

surface-fused virions failed to release their contents into the cell [22]. In a separate paper, they showed that a fusion-related Env confirmation change was protected from an externally-added inhibitory peptide, indicating that fusion does not occur at the plasma membrane [23]. Their data, combined with evidence from both older [55] and newer studies (Chapter 6 and [3]), build a strong argument for productive endocytic pathways for not only HIV-1, but potentially other pH-independent viruses [19, 22].

2.2 Red blood cells

Red blood cells, also called erythrocytes or RBCs, originate as pluripotent hematopoietic stem cells; the differentiation process occurs in the bone marrow and takes approximately four days before the cells enter the blood stream. At the time of entry, RBCs are still immature and maintain a slightly oversized, anucleated, spherical shape as well as a small amount of RNA. They transform into a biconcave shape after 1-2 days [28], often described as a “donut” shape 6-8 μm in diameter and 1-2 μm thick [34, 59]. Over time they gradually shrink, lose membrane flexibility, and produce less ATP. When their energy needs are no longer met the cell cannot maintain Na^+ and K^+ gradients can no longer be maintained and the membrane will rupture, called hemolytic anemia [60]. RBCs typically survive in the blood stream for about four months before their reduced flexibility causes them to be filtered out by macrophages in the spleen [28].

RBCs’ small size, lack of a nucleus, and high deformability allow them to squeeze through capillaries that are only ~2 μm in diameter, making them ideal vessels to transport oxygen throughout the body. The main content of RBCs is hemoglobin [61], an oxygen-binding, tetrameric protein whose four subunits are each bound to a

separate, iron-containing heme group. Oxygen binds to hemoglobin when its environment is higher in pH or O_2 concentration, such as in the lungs, and is released in areas with lower pH, lower O2, and higher CO2 [60]. Oxygen binding in hemoglobin is cooperative: the first oxygen to bind to a heme is the least energetically favored, and the conformation changes caused by binding make it successively easier for each additional oxygen to bind to another heme in the same tetramer [60].

The membrane of RBCs has been highly studied, in part because intact membranes are easy to obtain by swelling and draining the cells through hemolysis. The skeleton is composed primarily of the fibrous protein spectrin, which forms a pentameric or hexameric array attached to the membrane through a variety of proteins, including actin and the integral membrane proteins band 3, which is responsible for passive ion transport transmembrane, and glycophorin A. It is thought that the residual charge of glycophorin A prevents RBCs from sticking to one another, but it is also the receptor used during malarial infection [61].

Structural proteins produce the donut shape of RBCs, but deformities in these can lead to spherical or ellipsoidal cells, which leads to shortened cell lifetimes and oftentimes to anemia in the patient [28]. Sickle cell anemia is characterized by crescent-shaped, elongated RBCs, and is often accompanied by lower total RBC count. A single amino acid mutation in two of the four subunits of hemoglobin is responsible for this disease. The change in the protein structure leads to aggregation of hemoglobin into nearly crystalline structures, eventually rupturing the cells [60]. RBC morphology can also be influenced by environmental conditions; stomatocytes are uniconcave RBCs

with a single, often elongated depression in the center, and can be induced by the effects of decreased salt, pH, or cholesterol on the membrane [62].

Chapter 3 Basics of modern microscopy

3.1 Introduction to fluorescence

When an electron is excited from a ground state, if it has the opposite spin as the paired ground state electron it's referred to as a singlet state; an electron with the same spin as the left-behind ground state electron is referred to as being in a triplet state. Light emitted during relaxation of the electron is called luminescence, and further designated as either fluorescence when returning from the singlet state or phosphorescence when returning from the triplet state. Because the returning electron has complementary spin to the ground state paired electron, fluorescence is a much faster process than phosphorescence [63]. The energy (E) released by the electron's decay is directly proportional to the frequency of the light (v), and thus inversely proportional to the wavelength (λ) of the released photon:

$$E = h\nu = \frac{hc}{\lambda}$$

Where h is Planck's constant and c is the speed of light.

In addition to electronic states, molecules have many vibrational and rotational energy states. The energy of an excited vibrational state is less than that of an electronic state, and vibrational states essentially 'stack' on top of electronic states to form a much broader, essentially continuous range of excited state energies, as shown in the Jablonski diagram in Figure 3.1. This leads to a continuous spectrum of photons that can be absorbed to excite the molecule, and a continuous spectrum of emitted photons from relaxation. Once excited, an electron can decay to a lower vibrational state before relaxation, losing small amounts of energy along the way. The loss of energy results in a longer, red-shifted wavelength of emitted light than was absorbed to

excite the molecule. Because the electrons have much lower mass than the nuclei of the atoms in the fluorescent molecule (fluorophore), the transitions between states occur much faster than the nuclei move. This effect, called the Franck-Condon principle, results in the energy between states to be essentially identical for both absorption and emission of photons, and is why absorption and emission spectra appear to be mirror images of each other.

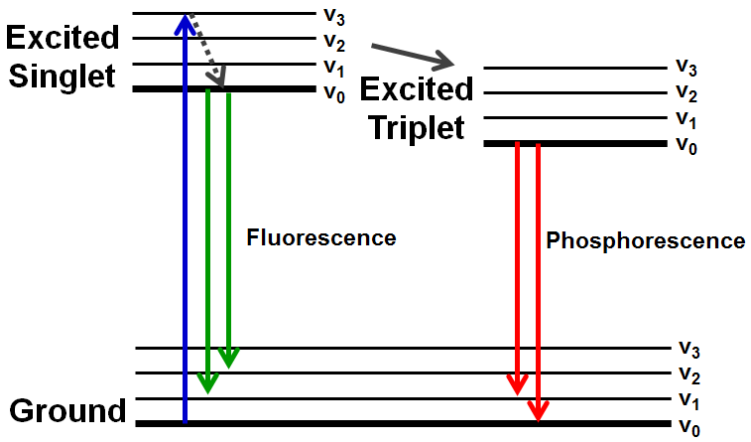

Figure 3.1 Jablonski diagram. Horizontal lines indicate allowable energy states within a molecule. Electrons residing in the ground state can be excited (blue) to a higher energy state by absorption of a photon. Electrons can easily transition between vibrational states (v0 – v3), and typically lose energy before decaying to the ground state through emission of a fluorescent photon (green). Alternatively, excited electrons can transfer through intersystem crossing to an excited triplet state. Decay from a triplet state through emission of a phosphorescent photon (red) is much more difficult and thus slower than decay from a singlet state.

3.1 Introduction to microscopy

The most basic microscope is simply a lens that magnifies an image of whatever lies at its focal plane. Compound microscopes use multiple lenses for greater magnification, and frequently allow for further modifications of the light passing through it. Fluorescence microscopes, for example, separate the light by wavelength to travel along different paths. Typically, compound microscopes contain an objective (a single

unit composed of many lenses) to focus on and magnify samples by 2-100X, and another lens to focus the image through an eyepiece and/or onto a camera. Microscopes can be both upright, where the objective is positioned above the sample, or inverted with the objective below the sample. Most modern microscopes use infinity-corrected objectives; with these, light is collimated before the objective allowing for multiple optical elements to be placed in the path and for the distance between the sample and camera to be adjusted without requiring changes to the lenses or alignment. For brightfield imaging, white light is focused onto the sample by a condenser lens located opposite the objective from the sample (see Figure 3.2) [64]. When a complete 2D image is collected at once, such as described above using a camera, the technique is referred to as widefield microscopy. Additional techniques that build up an image over time are described later on in this chapter.

3.2 The diffraction limit

When light travels through matter it will interact with its environment and spread out. If light passing through a pinhole is imaged onto a flat 2D surface, the point source of light will appear as a series of concentric rings with decreasing radial intensity, called an Airy disk [64, 65]. Similarly, the 3D spread of light generated from a point source is called a point spread function (PSF) [65]. Most samples of interest are not infinitely small point sources of light separated by relatively large distances, and the PSFs from each point in a sample will overlap causing the distinction between points to blur.

Imagine the pattern of light emitted from a sample to be represented by a combination of sinusoidal waves of varying spatial frequencies. Diffraction causes the different frequencies to bend at different angles, and whenever light travels through

some form of aperture the higher spatial frequency information about the original source of light is lost, thus causing blurring between distinct sources of light. The smallest distance two objects need to be apart in order to be identified individually is referred to as the diffraction limit. For resolution in x and y, this is approximately half of the wavelength of light, but more formally is defined by:

$$d_{x,y} = j\frac{\lambda}{NA}$$

Where λ is the wavelength of light, NA is the numerical aperture of the system (which takes into account both the index of refraction of the medium and the angles allowed by the objective), and j is a coefficient that changes depending on which criterion is used for determining resolution. For the Rayleigh resolution limit j is 0.61 [64], and with the Abbe criterion j is 0.5 [66]. Resolution is worse in z, and the definition of z resolution (or depth of field) is:

$$d_z = \frac{2n\lambda}{NA^2}$$

Where n is the index of refraction of the medium between the sample and objective [67, 68]. For powerful visible light microscopes, the diffraction limit is typically ~200 nm in x and y, and ~500 nm in z. Although that is sufficient for studying some biological applications, such as distinguishing individual mitochondria (500+ nm in diameter [69]), it is insufficient for many other applications including studying actin fine structure (~10 nm in diameter [70]) or identifying single human immunodeficiency viruses (~120 nm in diameter [20]), particularly in cases where there is a need for high resolution in all three dimensions.

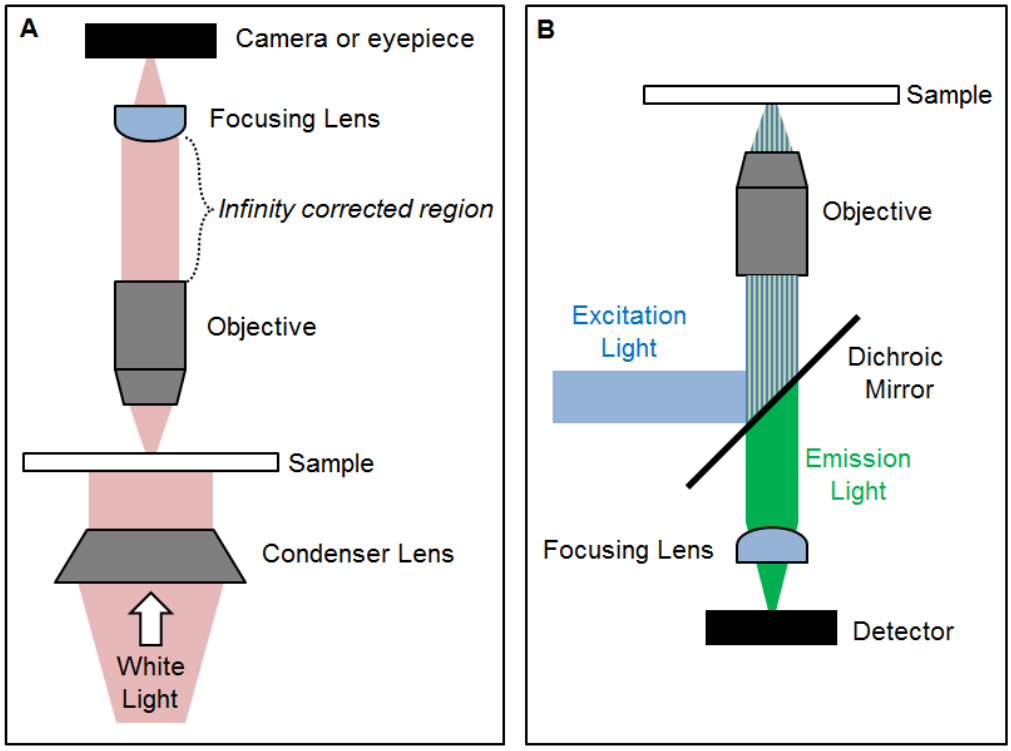

Figure 3.2 Microscope layout. Modern compound microscopes typically use both an objective and a focusing lens to magnify an image of a sample onto an eyepiece, detector, or camera. Infinity-corrected objectives allow multiple optical elements to be placed prior to the objective without causing distortions or changing the distance between the sample and detector. On the left (A), white light illuminates a sample for brightfield imaging. On the right (B), excitation and emission light are separated using a dichroic mirror for fluorescence imaging.

3.3 Fluorescence microscopy

In fluorescence microscopy, both the excitation and emission light typically travel through the same objective instead of using a separate condenser lens. Excitation comes either from a laser, which provides single-wavelength, coherent light; or from incoherent white light that has been filtered to allow a range of wavelengths covering 10+ nm of the spectrum. A dichroic mirror, which reflects light below a certain wavelength threshold and transmits longer wavelengths, reflects the excitation light to the objective. When both scattered and fluorescently-emitted light return through the objective, only the red-shifted fluorescence will pass through the dichroic mirror and

travel to the detector. Dichroic mirrors are not very efficient, so emitted light is often directed through a clean-up filter to limit the amount of scattered excitation light that reaches the detector. A schematic of this separation of light can be seen in Figure 3.2.

3.4 Spinning disk confocal microscopy (SDCM)

Scanning confocal microscopy (SCM) improves resolution over wide field techniques by focusing emitted light through a pinhole, shown in Figure 3.3, thus blocking the majority of light that originates from outside the focal plane. When the pinhole is smaller than an Airy disk, the resolution is improved to [67]

$$d_{con,x,y} = 0.4\frac{\lambda}{NA}$$

And

$$d_{con,z} = \frac{1.4\mathrm{n}\lambda}{NA^2}$$

Because the pinhole rejects light outside of the focal region, only a single spot can be imaged at a time, and an entire image must be built up by scanning across the sample pixel-by-pixel (or voxel-by-voxel). This time-consuming process can sometimes take minutes for a single plane, and means that SCM is not very useful for capturing the dynamics of many fast-moving biological systems. Furthermore, in order to gain the 1.4X maximum improvement in lateral resolution, the pinhole must be much smaller than the focal spot, rejecting far more light than practical for most samples [71].

Spinning disk confocal microscopy (SDCM) improves upon SCM by splitting a single excitation beam into many smaller beams that are each focused through their own individual pinhole. The incoming excitation beam hits a literally spinning pair of disks, one with hundreds of pinholes to split the beam, and another with hundreds of

microlenses to focus the returning fluorescence emission through the pinholes. As the disk spins, the excitation light is essentially 'scanned' across the sample by the moving positions of the pinholes and lenses. The limitation on the imaging speed changes from the slow scanning of the pinhole with SCM to frequently only the camera readout speed using SDCM. Although the improvement in lateral resolution is relatively small compared to wide field techniques, the gain in axial resolution combined with the significantly increased speed make SDCM a powerful tool for imaging live cells.

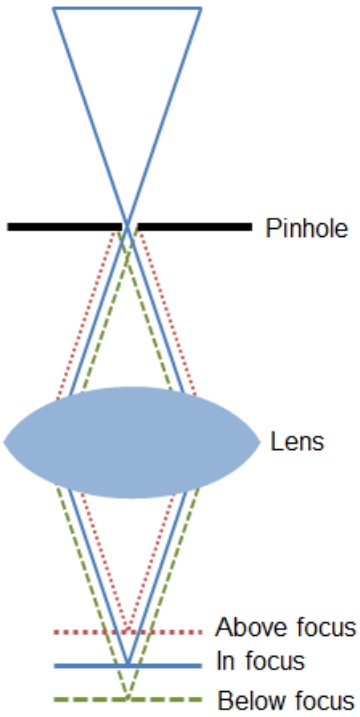

Figure 3.3 Confocal filtering. When light from a sample is focused through a small pinhole, the majority of out-of-plane light is blocked. Scanning confocal microscopy uses this effect to achieve high axial resolution images by scanning the lens, pinhole, and a detector to build up the image pixel-by-pixel.

3.5 Super resolution imaging

As noted by Mats Gustaffson, the diffraction limit described above has three basic assumptions: 1) emission collection through a single objective lens, 2) even

illumination throughout the sample, and 3) linear, single-photon absorption and emission [71]. Several techniques have been developed in the last few decades to overcome the diffraction limit. 4Pi microscopy addresses assumption one by interfering wavefronts from two separate objective lenses, thus sharpening the PSF, and also by collecting the emission light through the two lenses [65, 71]. Structured illumination microscopy uses loophole two by encoding higher resolution data in optical beat frequencies, and the third point is exploited by multiphoton techniques such as STED and PALM. Following is a discussion of the basic principles of a few common super resolution techniques. As each method has advantages and drawbacks that must be balanced for the needs of individual experiments, these selection considerations are also highlighted below and in multiple other publications [65, 66, 71, 72].

Structured illumination microscopy (SIM)

Moiré patterns are seen when two patterns are overlapped, interfering with each other to form a third (moiré) pattern with a lower spatial frequency. The moiré pattern changes when the original two are rotated or translated with respect to each other, as shown in Figure 3.4. When one of the original patterns is well characterized, and the moiré pattern is analyzed at enough phase and angle shifts, the second pattern can also be characterized even if it was originally unknown. SIM uses this principle by using a literal structured illumination on the sample instead of wide field illumination. This striped illumination pattern is rotated, with respect to the sample, to three different angles and moved across five (in 3D, only three in 2D) phase displacements. The corresponding diffraction-limited moiré pattern is recorded by the microscope camera, and the sample image is mathematically reconstructed from the 15 images. Because

the moiré pattern can be up to 2X lower in resolution than the patterned sources, but is recorded at the diffraction limit, the sample image can be reconstructed with resolution up to 2X higher than the diffraction limit. Details on implementation, reconstruction, and the underlying theory can be elsewhere [71, 73-75].

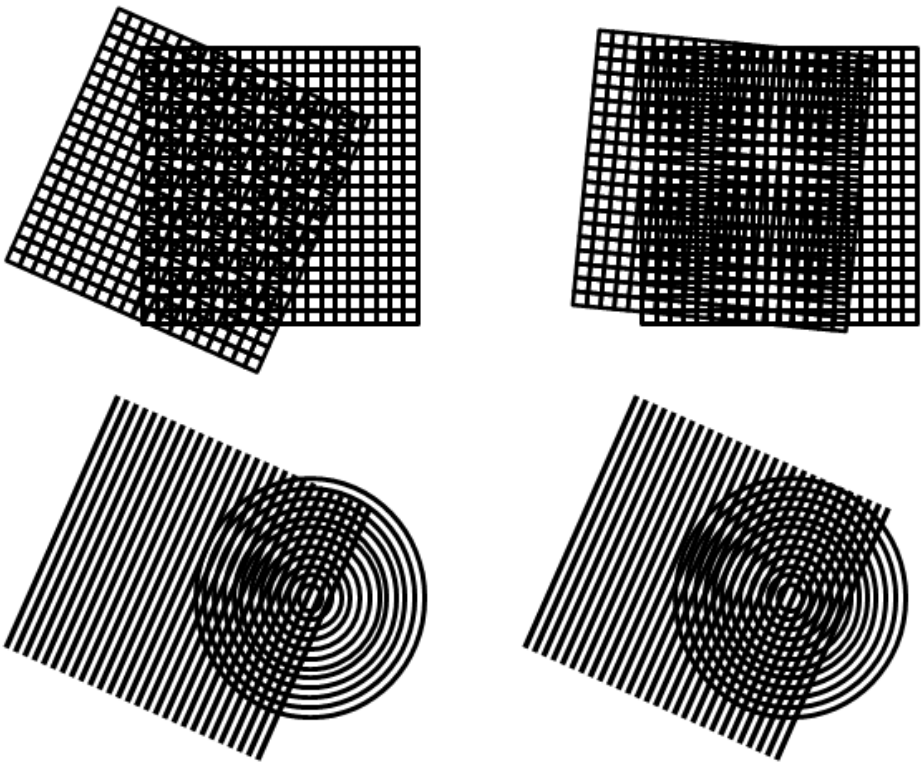

Figure 3.4 Moiré patterns. Two overlapping patterns create a third, lower spatial frequency pattern. The third pattern changes when the angle between the first two patterns changes (top, left to right) and when they are translated (bottom, left to right). The patterns can be, but do not need to be identical to show this effect.

The reconstruction of SIM images requires a significant amount of computation after acquisition, and the algorithm used assumes that the sample has not moved during the acquisition of the 15 moiré patterns; any movement (or significant photobleaching) will lead to strong artifacts in the output image. Besides the extra acquisition time compared to conventional wide field methods, the required 15 acquisitions per reconstructed z-plane (120 images per micron imaged in the z-plane)

result in significantly more photobleaching of the sample, particularly since high signal-to-noise ratios are needed. This makes live imaging particularly difficult, as most samples' emission will have diminished below usable intensities after imaging only a few time points (approximately 10-20 μm of total imaging thickness across time points for even good samples). Artifacts and reconstruction errors are fairly common and can be caused by a variety of sample or imaging conditions. As another example, SIM does not work particularly well in thick samples because the striped illumination pattern is easily distorted as it passes through inhomogeneous media. One advantage of SIM over other super resolution techniques, such as PALM, is the ability to use the same fluorophores as conventional microscopy; however, extra consideration towards photostability and brightness are still required. SIM results in a maximum of a 2X improvement in resolution, which is the least of the methods compared here, but has significant advantages in ease of sample preparation, multichannel imaging, compatibility for multimodal imaging, and frequently in acquisition speed.

Localization microscopy

The position of an isolated fluorophore can be very precisely located by fitting its emission to its PSF, typically a Gaussian profile. The precision is approximately equal to the standard deviation of the PSF divided by the square root of the number of photons detected [76]. Photoactivated localization microscopy (PALM) [77] and stochastic optical reconstruction microscopy (STORM) [78] both operate by limiting the number of active fluorophores in an otherwise densely-populated sample. Before the fluorophores will emit, they need to first be activated with a wavelength of light different from the excitation (typically a shorter wavelength). Using low intensity activation light will ensure

that only a few probes will activate at a time. The fluorophores will continue to emit until photobleached or switched into another dark state, and new fluorophores will be activated. Many, potentially thousands, of frames will be recorded by the camera to keep the emitting fluorophores temporally separated. Afterwards, PSFs will be fitted to the recorded points and all of the frames will be collapsed into a single composite image.

The need to temporally isolate the fluorophores naturally leads to a long time to capture a single image. When the technique was first discovered, 2D PALM images took several hours to acquire [77]. Since then, advances in both fluorescent probes and instrumentation have reduced the time to minutes, but because precision is dependent on the number of photons collected, the need for speed needs to be balanced with the desire for precision. These slow acquisition speeds have also inhibited 3D imaging. However, several methods have been developed to encode 3D positioning information into the 2D recorded image. Huang, et al. used a cylindrical lens to add astigmatism to their PSFs; while the centroid of the fluorophore's recorded shape still provided axial localization, the ellipticity and orientation of the altered shape could be used to determine axial localization [79]. Similarly, Pavani et al. encode axial information in a 'double helix', which splits a single emitter's shape into two lobes whose relative orientations change depending on z-positioning [80].

Multicolor localization microscopy is possible [81], but require a careful selection of highly specified fluorophores or fluorophore-activator complexes [82]. Although much slower than SIM, the localization is significantly improved with precision on the order of single or tens of nanometers [76-79], compared to SIM's maximum of ~120 nm, and the

instrumentation is typically much simpler and less expensive. However, it can be difficult to understand the meaning of many tiny dots without also having some context of where they are located in a cellular body as provided by wide or bright field imaging, especially during the acquisition process. Finally, it is important to note that the precision of localization provided by PALM and similar methods does not guarantee positioning accuracy.

Stimulated emission depletion (STED) microscopy

When orbital electrons are subjected to an external electric field, they can be induced to make an electronic transition to a higher (in the case of absorption) or lower (through stimulated emission of photons) energy state. The probability of this transition increases both by matching the frequency of the external field to the electron's dipole and by increasing the intensity of the field. With very high intensities, nearly every electron that transitions to the excited state can be forced to return to its ground state via stimulated emission instead of via spontaneous emission or non-radiative decay. The photons from stimulated emission will share the same properties as the external field, including frequency, phase, polarization, and direction of propagation.

STED microscopy utilizes this principle to 'cancel out' excitation light, artificially narrowing the excitation volume in a sample. STED setups operate similar to scanning confocal microscopes: a diffraction-limited excitation beam is scanned across a sample, and emitted light is captured with a point detector to generate an image pixel-by-pixel. With STED, however, a red-shifted depletion beam is combined with the excitation beam, forcing emission in all overlapping regions. Typically a donut-shaped depletion beam is used, which results in a symmetric PSF. The resolution of the generated image

can be tuned by narrowing the donut hole, which can be accomplished by increasing the STED beam intensity. Resolution using this technique can be approximated by:

$$d \approx \frac{\lambda}{2NA\sqrt{1 + I/I_s}}$$

Where I is the intensity of the applied STED beam, and I_s is a property of the fluorophore, namely the inverse of the product of the dye's transition cross section and lifetime [83]. When $I >> I_s$, the equation is reduced to the classical Abbe's diffraction limit.

The tunable resolution of STED is a major advantage, with resolutions reported on the order of single nanometers [65] and ~50 nm within a living cell [84]. However, STED requires very high intensities even for moderate resolution improvements, which can be very taxing on the sample. Furthermore, the dye needs to both have an ideal I_s and be relatively photostable. Alternative methods to narrow the effective excitation volume have been suggested, including using photoswitchable fluorophores, which require significantly less power but come with additional technical and labeling challenges.

Although frame rates of 28 Hz have been achieved [65], scanning techniques are inherently slower than wide field techniques such as SIM. Both techniques can be used to image in 3D, but the confocality of STED allows it to image significantly deeper in samples such as tissue, and images require no post-acquisition processing. Similar to SIM and localization microscopy, STED microscopy is two-color capable. When a single wavelength STED beam is used to deplete two fluorophores, the scanning nature of STED ensures accurate image registration, yielding an image with both precise and

accurate localization [85]. STED systems are comparatively complicated and expensive to set up, but offer distinct advantages over other methods in either speed or resolution.

3.6 Holographic optical tweezers (HOT)

Trapping of particles by radiation pressure was first reported in 1970 [86], and the first single-beam optical trap in 1986 [87]. When light travels through an interface, the light will bend according to Snell's Law:

$$\frac{\sin\theta_1}{\sin\theta_2} = \frac{n_2}{n_1}$$

Where θ_1 and θ_2 are the incidence angles of the light coming into the interface and n_1 and n_2 are the indices of refraction of the respective media. Because light has momentum which must be conserved, the bending of the light requires an equal and opposite change in momentum. Small objects with a higher index of refraction than the surrounding medium (such as polystyrene beads in water or cells in buffer) subjected to a focused beam of light feel a net attractive force that work to hold the object in the center of the beam, as shown in Figure 3.5. Axial positioning is determined both by scattering forces pushing the object away from the light source and by gradient forces, which must dominate in order to maintain a stable trap [88]. By moving the focal point of the beam, the object can be moved within the medium.

The optical force (F) felt by a trapped object is:

$$F = \Delta n \frac{Nh\nu}{c} = \Delta n \frac{P}{c}$$

Where Δn is the difference in the index of refraction between the media and the object, and P is the laser power. If for biological cells we assume Δn = 0.1 [59], and then a cell trapped by a 15 mW laser only feels a force of 5 pN. Although optical tweezers typically

only generate forces on the order of piconewtons [88, 89], the effect of the laser on the trapped object can vary with absorption. When bacteria were first trapped by Ashkin, et al. in 1987 [90], the 514 nm laser swiftly fried the trapped cells. In order to avoid hemoglobin and chlorophyll absorption, while avoiding significant absorption by water [89], they switched to a 1064 nm laser. With this biologically-friendly setup, Ashkin et al. were able to see bacterial and yeast cells split while trapped. Since then, optical tweezers have been used to study a variety of living cells using multiple (typically near-infrared) wavelengths [89, 91-93].

Traditionally, trapped objects were moved in 2 or 3D by either translating the sample stage [94] or by scanning the beam using an extra lens [90] or mirrors [95]. With these techniques, multiple, independently-controlled beams were needed in order to simultaneously manipulate multiple objects or to squeeze or compress them. Holographic optical tweezers (HOT) removes the need for independent beams by using a spatial light modulator (SLM) or other diffractive elements to split a single beam for many traps.

HOT works by replicating interference patterns from multiple-beam traps at the objective pupil. When individually generated, coherent beams interfere at the pupil and create a diffraction pattern. If the same pattern, including phase and relative amplitude, is generated elsewhere and imaged onto the pupil using a pair of lenses, the image at the objective focus would be the same as if the two individually-generated beams had been used. Spatial light modulators can reform a single, polarized beam into any holographic phase pattern, so a computer-controlled SLM positioned at the image of the objective pupil can be used to create nearly any pattern at the objective focus, including

multiple optical traps. These holographic optical tweezers can be manipulated at the refresh rate of the SLM, allowing for rapid, simultaneous manipulation of individual traps [96, 97].

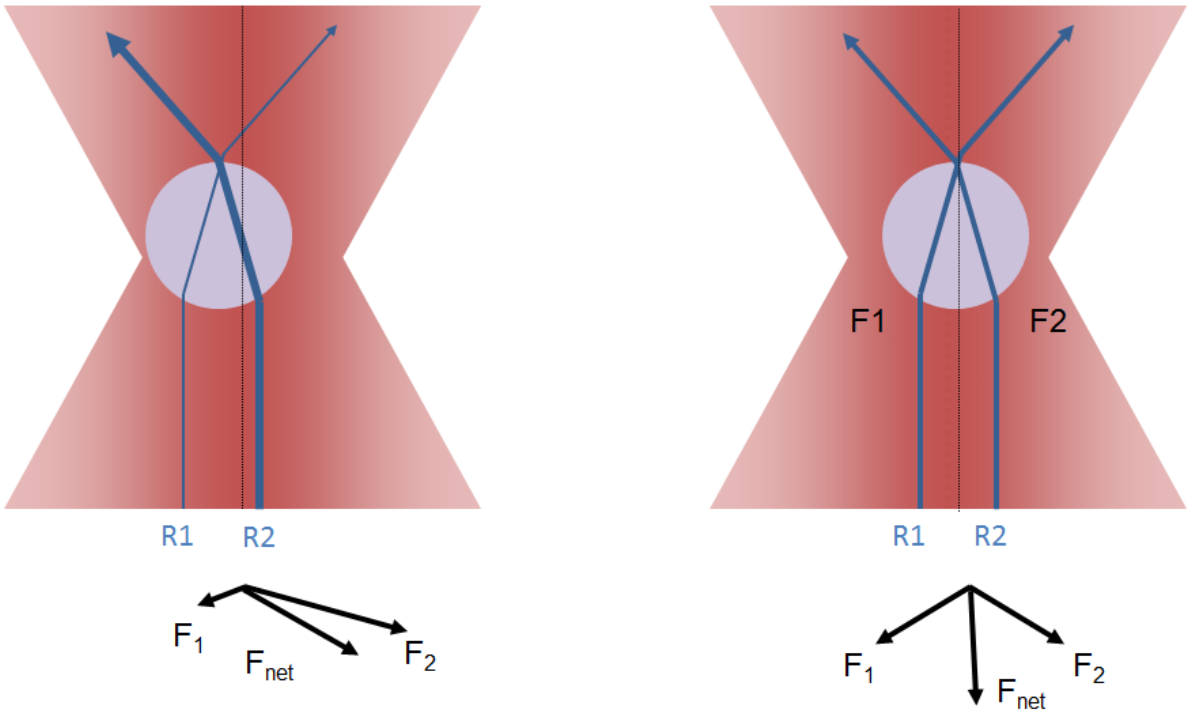

Figure 3.5 Optical trapping forces. The bending of light rays (R1 and R2) at the interface between media with different refractive indices has an associated change in momentum and thus force (F1 and F2). For small objects with a higher index than the surrounding media, this results in a net force that works to keep the object trapped near the center of a focused beam of light. (Left) Higher intensities near the center of a focused beam result in a greater magnitude force directed opposite the direction of displacement of a trapped bead. (Right) Even when a bead is located at the center of a focused beam, it still feels a net force towards the beam source due to changes in momentum. Axial positioning is determined both by these gradient forces and by scattering forces (not pictured).

Chapter 4 Development of an instrument to fluorescently image optically trapped cells in three dimensions

Live cell imaging has led to a much greater understanding of inter- and intra-cellular mechanisms. However, many types of cells are natively found suspended in solutions and mobile, rather than adhered to a stable substrate. Any sort of motion, passive or active, makes long-term and 3D imaging of these cells challenging if not completely impossible.

Many techniques have been developed to compensate for cellular drift, but each has its own drawbacks. Mechanical manipulation using pipettes, needles, and wires can be difficult to control, risk damaging or activating the cell, and pose greater risk to the researcher particularly when working with infectious or pathogenic material. Software to track and compensate for cell movement is limited by the field of view and the speed of the motion, as well as the reliability of the tracking algorithm itself. Finally, optical tweezers have been useful to hold cells in place, but this often precludes 3D imaging and the effects on the cell are still poorly studied.

A particular problem of the combination of optical tweezers with confocal microscopy is that in order to change the axial position of the focus/optical section the objective lens is typically translocated. This, however, will affect both parameters simultaneously, and thus it would be impossible to use this concept to optically trap a cell and also determine its 3D morphology. Here, we have solved this problem by utilizing the fact that holographic optical tweezers based on a spatial light modulator can be freely adjusted based on diffractive optics. Thus, we have developed a feedback mechanism that enables us to ensure that the cell's axial and lateral position in the

optical trap will not change while the objective lens is translocated to change the plane of the optical section.

4.1 Optical layout

A spinning disk confocal microscope was combined with holographic optical tweezers (HOT) as shown in Figure 4.1. Excitation for the fluorescence imaging path is provided by an Innova 70C multiline ArKr ion gas laser (Coherent), with line selection provided by an acousto-optic tunable filter (AOTF) (Andor). Excitation light is spatially filtered through a 630 nm, 0.11 NA, single mode fiber (ThorLabs) and spectrally filtered through single or multiband cleanup filters, before entering a CSU-10 spinning disk confocal unit (Yokogawa) with a 405/488/568/647 nm quad-band dichroic mirror (Semrock). The light path can be switched to collect brightfield images using one CCD (Guppy, Allied Vision Technologies) or sent through a motorized filter wheel (Ludl Electronics)with user-selectable emission filters (607/36, Semrock, used here) before being focused on a 512 x 512 pixel EMCCD camera (iXon 897, Andor).

A 1064 nm, CW, diode pumped solid state laser (Shanghai Dream Lasers Technology Co.) provides up to 2.175 W of power, which is controlled using a λ/2 waveplate and polarizing beam splitter to dump excess power. The polarization can be adjusted using another λ/2 waveplate. The beam is then expanded using a 3x beam expander (Edmund Optics) and reflected at a low incidence angle onto a phase-only spatial light modulator (SLM) (Boulder Nonlinear Systems via Arryx Inc.). A pair of 2” achromatic lenses is used to translate the hologram onto the imaging plane of the microscope. 0^{th} order effects are minimized by maintaining the low incidence angle and by matching the incoming beam polarization to the SLM axis.

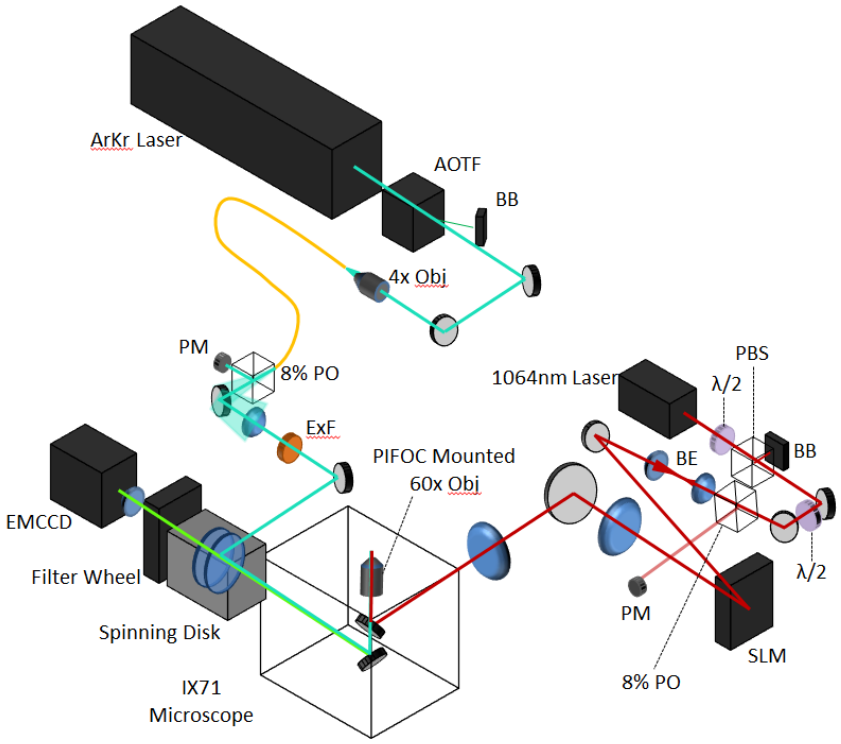

Figure 4.1 Optical layout. Separate imaging and trapping paths combine through a single, 60x oil-immersion objective. In the imaging path (upper), laser lines are selected by an acousto-optical tunable filter (AOTF) before being coupled into a single mode fiber. After exiting the fiber, the relatively flat center of the beam is collimated and spectrally filtered. The excitation beam is reflected by a multi-band dichroic within the spinning disk unit into the IX71 microscope. Emission light returning through the spinning disk is filtered before being focused onto the EMCCD camera. In the optical trapping pathway (right), power is controlled by a λ/2 waveplate and polarizing beamsplitter (PBS). The polarization is rotated using another λ/2 waveplate and the beam is expanded before being reflecting off the spatial light modulator (SLM) at a low incident angle. 2" optics are used to preserve the resolution of the hologram as it is translated through the microscope to the imaging plane. In both pathways, power is monitored using 8% beam pickoffs (8% PO) and power meters (PM).

The imaging path (right side port) combines with the trapping path (rear port) at a dichroic mirror just below the objective on an IX71 inverted microscope (Olympus). The 60X, 1.42 NA oil immersion objective (Olympus) is mounted on a 100 nm-range PIFOC piezo objective controller (Physik Instrumente), which is also controlled by the Andor iQ

software. An 842 nm shortpass filter (Semrock) below the dichroic mirror blocks reflected 1064 nm light from reaching the cameras.

4.2 Software description

The HOT.GUI was written in LabView using functions from the HOT software development kit purchased with the SLM. X and Y calibration between the SLM positioning and the camera field of view (FOV) can be performed through a subroutine that asks users to locate and identify three laser trap positions on the FOV. Additional modifications are possible, including in Z, by manually adjusting calibration parameters as needed.

The HOT and corresponding GUI are run through a separate computer than the spinning disk system. The only interaction between the two is a voltage readout from the SD-controlled piezo objective holder running to the HOT setup. When desired, the software uses this readout to adjust the z-plane to counter the objective motion. If this option is not selected, then as the objective moves to a new imaging plane, the trapped object will be dragged along and the same plane of the object will be continuously imaged. When selected, simultaneous trapping and full 3D imaging is enabled.

To create a trap, the user only needs to hold the CTRL key and click on the location in the FOV where they want the trap to be placed. Many functions use the same commands commonly used is in other programs, such as left-clicking and dragging to select all traps in the boxed area. Traps can be controlled individually or as a selection group for moving in x, y, or z; inactivation; deletion; or following a pre-defined motion path. Right-clicking on the FOV will move selected paths to that position. In addition to indicators on the FOV, each created trap is listed in a panel next to the

FOV along with its parameters including z-height and relative intensity. Unless otherwise specified in this panel, the trapping power will be split equally between each active trap.

4.3 System calibration

To ensure the trapping plane and the imaging plane remained collinear throughout the range of the piezo objective, the system was calibrated daily prior to use using 6 μm fluorescent polystyrene beads (FocalCheck, Invitrogen). A bead was trapped and the coordinates of the center monitored while it was moved in z over a range of approximately 30 μm. X and y offset values were modified using the HOTGUI until the bead remained centered throughout the z-stack, and no skew appeared with fluorescence imaging. The z offset value was adjusted so that a fluorescence image of a trapped bead appeared spherical, with 6 μm diameters in x, y, and z, as shown in Figure 4.2.

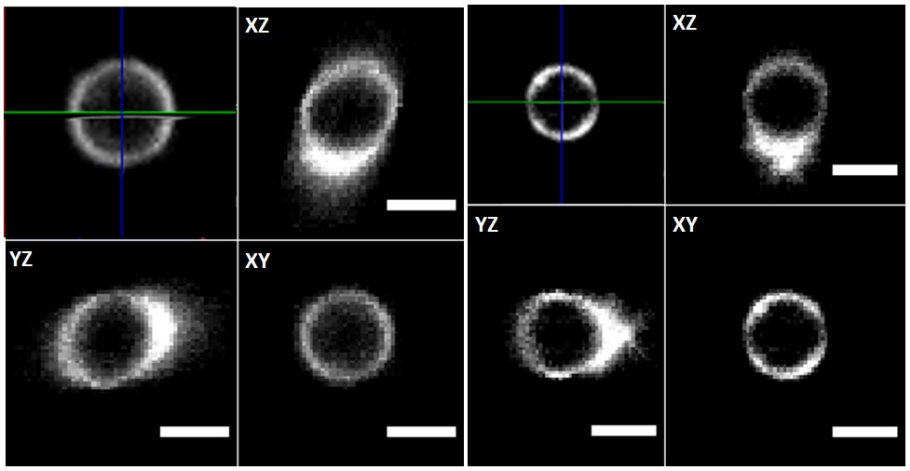

Figure 4.2 Skew correction. A slight angle between the trapping and imaging beams results in a skewed image. This can be corrected in the hologram generation software, and is calibrated using spherical, fluorescent polystyrene beads. Orthogonal plane views of the beads before (left) and after (right) skew correction. Scale bars are 5 μm.

For experiments, the power of the 1064 nm trapping beam was monitored through an 8% beam pickoff before the SLM. A multiplying factor was used that compared the pickoff power to power measured after the objective with the HOTGUI off. Trapping power was also measured with various configurations of optical traps. Compared to maximum power with the interface off, simply opening the software led to a 14% drop in power at the objective. When traps were created near the center of the field of view (FOV), very little additional power loss was noted, with only 15% (compared to HOTGUI off) loss for 1 trap and 18% loss for 20 total traps. However, when traps were moved further away greater losses were observed. Traps located in the middle of the edges of the FOV led to 18-25% losses, while traps located at the corners had 22-57% losses. Up to 20 traps were measured, and while the number of traps did not appear to affect total trapping power, distributions closer to the upper left of the FOV experienced greater overall losses. Demonstration using beads and cells

Positioning and holding cells for site-specific interactions

Adherent cells *in vitro*, or even non-adherent cells simply resting on cover glass, cannot mimic the interactions that occur in blood *in vivo*. Jurkat cells are used to study T cell immune interactions, such as virological synapses [50, 94, 98]. However, Jurkat cells will quickly settle and stick to cover glass, eliminating the mobility seen *in vivo*. Coating the surface with bovine serum albumin will reduce this effect, but only minimally. OT can be used to prevent contact with the cover glass, as well as manipulate cells to initiate contact and control the number of cells in a field of view. Figure 4.3 shows three polystyrene beads held at different depths to demonstrate the ability of this system to precisely position objects of interest relative to one another.

Additionally, the traps are very stable; Figure 4.4 shows a bead held at the same position for 50 minutes without wavering.

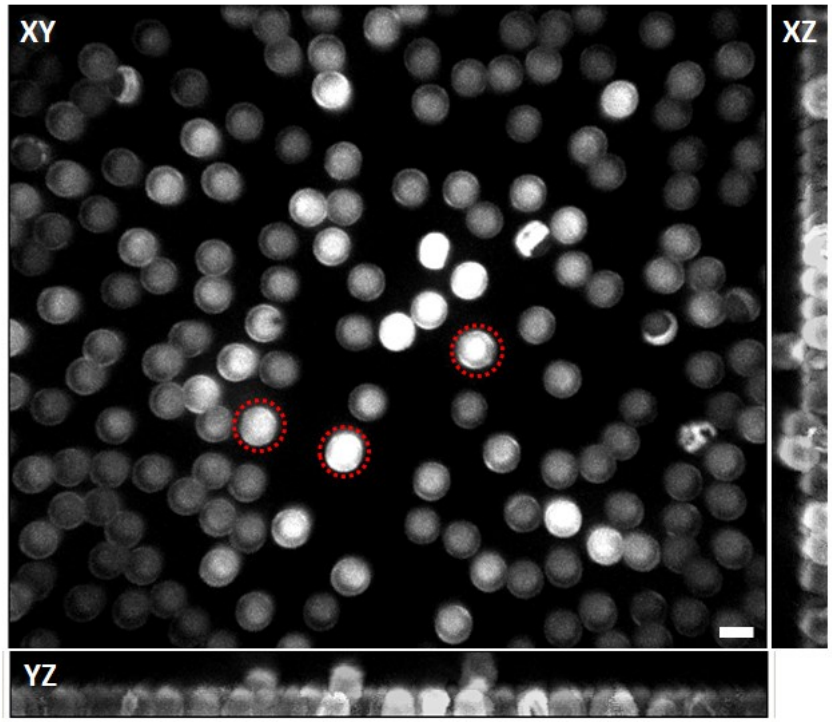

Figure 4.3 Multiplane trapping. XY, YZ, and XZ projection images of 6 μm fluorescent polystyrene beads trapped at multiple depths. Three beads are held at different z-planes just above the coverslip. Scale bar is 5 μm.

While OTs hold objects at a certain position, they do not prevent rotation within the trap. To highlight this, we imaged trapped and imaged Jurkat cells labeled with CellMask Orange (CMO). Unlike fluorescent beads, these cells are asymmetric making rotation within a trap easy to detect. Figure 4.5 shows four time points of a trapped cell slowly and unevenly rotating over a period of 18 minutes. Notably, the cell appears unharmed despite the long exposure to the trapping beam, which is consistent with other reports of optical trapping in near infrared at low powers [59, 99, 100].

There are many situations in which the orientations of trapped objects are important. When studying cellular interactions, for example, cells may need to be in

contact at areas with higher or lower levels of specific surface markers. In such cases, the cells may be rotated by using two traps instead of one. Objects held at two points will not rotate freely, and by changing the relative positions of each trap, the object can be turned to the desired orientation. In Figure 4.6, a single trap was used as a pivot and a second trap was placed at the edge of a CMO-labeled Jurkat cell. By moving the second trap around the pivot trap, we were able to rotate the cell by 90°.

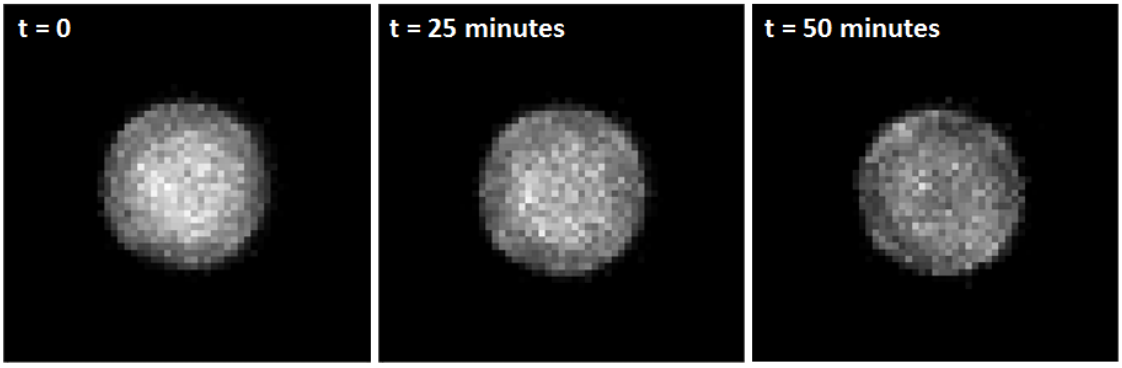

Figure 4.4 Trap stability. Z-projection images of a 6 μm, fluorescent, polystyrene bead held in a single, 10mW optical trap for 50 minutes.

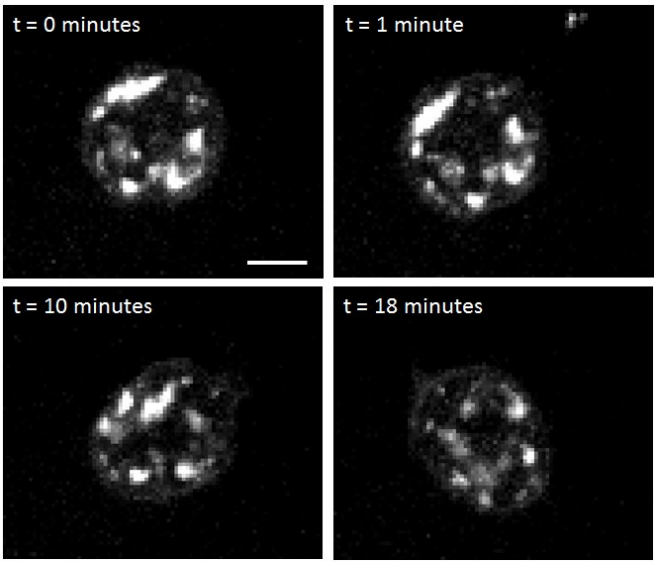

Figure 4.5 Passive rotation in an optical trap. A cell rotates while held in a single, 10 mW optical trap. Images are maximum intensity projections, scale bar is 5 μm.

Potential effects of optical trapping on cellular interactions

Although the tweezers are not likely to harm the cell, they may prevent or enhance cellular behavior or interactions. Previous studies using tweezers to look at synapses [94, 101] released the trapped particle before imaging, reducing some of the potential disruption. If a negative influence is detected or suspected, one solution would be to use indirect trapping: beads or other cells could be used to corral the target cells and keep them from drifting during imaging. This would provide the necessary control without directly influencing the system of interest. Additionally, if any cellular structures (on the membrane or within the cell) are reoriented due to the trap, this could interfere with intercellular interactions, and trapping could possibly induce T cell activation. Although releasing the cell before imaging may not restore the native orientation, indirect trapping would likely eliminate both of these effects. Alternatively, the effects of optical tweezers could be utilized to better characterize properties of the cells or interactions, such as studied by multiple groups [34, 102, 103] in detecting diseased red blood cell states.

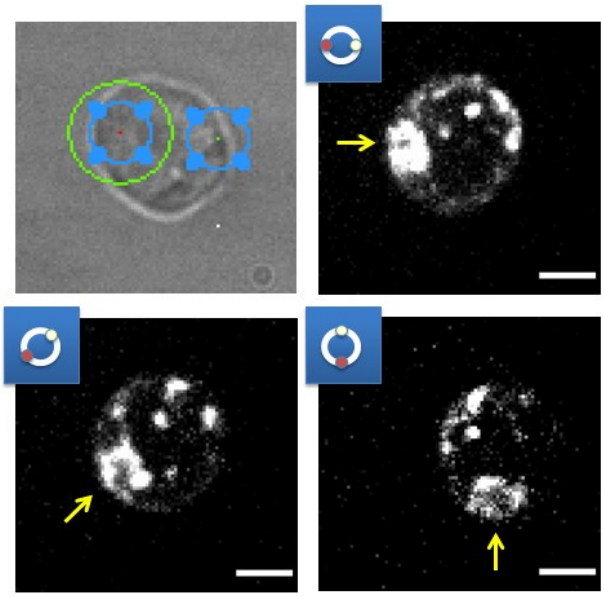

Figure 4.6 Directed rotation with two traps. A single cell held by two traps can be rotated by moving the trap positions relative to one another. Insets show relative positioning of the two traps. Images are maximum intensity projections, scale bar is 5 µm.

Chapter 5 Methods for visualizing and quantifying cell-to-cell transfer of HIV using fluorescent clones of HIV

The transfer of HIV by cell-cell transfer is highly efficient; virally infected T cells begin forming synapses with uninfected primary T cells almost immediately after the initiation of coculture *in vitro* and 20-30% of target cells are infected within just a few hours [104]. Recent research suggests that direct transfer may be the predominant mode of HIV spread between T cells [17, 49, 50]. Cell-to-cell spread of HIV was originally described using HIV infected Jurkat cells as donor cells and primary CD4+ T lymphocytes as acceptor cells [12, 105, 106]. In these studies, virus was detected in fixed cells using antibody staining. With the development of the green fluorescent protein (GFP), internal and external proteins can now be labeled by fusing them with fluorescent proteins, which enables cells to be imaged while still alive and physiologically relevant. To track the transfer of virus from cell to cell in live cells, we exploited recombinant, infectious molecular clones of HIV, particularly HIV Gag-iGFP [1], and other clones as noted below and in [3]. These clones carry GFP inserted internally into the Gag protein between the MA and CA domains, while maintaining infectivity without the need for helper virus. When used in conjunction with inert cell-tracking fluorescent dyes, recipient cells can be discriminated from input donor cells, and allow one to visualize the transfer of HIV from an infected T cell to an uninfected T cell [55]. Described below are methods for visualizing and otherwise quantifying the transfer of HIV from cell-to-cell cell. These techniques are especially useful in studies concerning the assembly and cell-to-cell transfer of HIV.

Studies were performed using the spinning disk setup described in Chapter 4.1 and, where mentioned specifically, other methods including scanning confocal microscopy and flow cytometry. Techniques for fluorescent clone generation and imaging on the spinning disk microscope are also available in a visualized publication format [104]. The video published in the Journal of Visualized Experiments (JoVE) demonstrates transfection of a human T cell line with HIV Gag-iGFP; preparation of a coculture with fluorescently labeled, uninfected CD4+ T cells; sample imaging, and representative results. Detailed protocols for the preparation, imaging, quantitation, and analysis are available below [3, 104]. Transfection of fluorescent HIV iGFP proviral DNA into T cells produces replication-competent HIV. As such, all procedures were undertaken only by trained laboratory personnel in certified biosafety level 2+ tissue culture rooms, under the appropriate biological use authorization.

5.1 Preparation of fluorescent HIV clones and target cells

Human CD4+ T cell lines Jurkat CE6.1 and MT4 were obtained from the American Type Culture Collection (ATCC, Manassas, VA) [3, 104]. Jurkat cells were prepared by carefully maintaining the cells at a concentration between 2 x 10^5 and 8 x 10^5 cells/mL in Jurkat culture media (RPMI 1640, 10% fetal bovine serum, 100 units/mL penicillin, and 100 µg/mL streptomycin. Culturing Jurkat cells at concentrations in excess of 8 x 10^5 cells/mL resulted in a reduction in transfection efficiency.

HIV Gag-iGFP and HIV Gag-iCherry, infectious variants of pNL4-3, have a fluorescent protein inserted between the matrix and capsid domains of Gag [107]. Jurkats were transfected with the viral plasmid using the Amaxa nucleofection method (Lonza, Walkersville, MD). 5 x 10^6 cells were pelleted by centrifugation for 10 minutes at

150 x g, aspirated, washed in sterile phosphate buffered saline (PBS), and pelleted again. The pellet was resuspended in 97 µL of pre-warmed, nucleofector solution V containing the manufacturer's supplement. 3 µL of endotoxin free HIV plasmid (1 µg/µL) was added to the cell suspension and mixed gently. The cell suspension was gently transferred to a cuvette, nucleofected using program S-18, and immediately transferred to 3 mL of prewarmed Jurkat culture media without antibiotics.

To prepare CD4+ target cells for virological synapses, we obtained human peripheral blood mononuclear cells from buffy coats by using a standard Ficoll-Paque (GE Healthcare, Uppsala, Sweden) protocol. CD4+ T cells were then negatively selected using a magnetic bead isolation kit (Miltenyi Biotec, Auburn, CA). These could be cryogenically stored in liquid N_2 in aliquots of 5 x 10^6 cells/500 µL of freezing media (90% fetal bovine serum/10% DMSO). Thawed primary CD4+ T cells were cultured in RPMI 10% FBS, supplemented with 10 units/mL of IL-2.

The Jurkat cells were allowed to recover from the transfection overnight. Cellular debris was removed by centrifugation over 1.5 mL of a ficoll hypaque density gradient material at 400 x g for 20 minutes at room temperature with the brake off. The cell layer was carefully transferred a new 15 mL conical tube, then diluted with RMPI to a total volume of 15 mL before centrifugation at 300 x g for 10 minutes. The pellet was resuspended in 3 mL of Jurkat culture media in a 2 cm well (6-well plate) and the cells were returned to the tissue culture incubator.

To distinguish target cells from donor cells in cell-cell transfer experiments we prelabeled the CD4+ target cells with fluorescent dyes with cell. Primary CD4+ T cells were labeled the evening before use with CellTracker Orange or Blue (Invitrogen,

Carlsbad, CA) or DDAO Far Red with minor modifications from the manufacturer's protocol. 4 x 10^6 primary CD4+ T cells were pelleted at 400 x g for 10 minutes, then washed with 5 mL of PBS and resuspended in 2 mL of PBS. CellTracker Orange was added to a final concentration of 1.5 μM and incubated at 37°C for 20 minutes, 10-20 μM of CellTracker Blue for 30 minutes, or 0.7 μM of DDAO for 6 minutes. 8 mL of complete Jurkat media was added before centrifugation at 400 x g for 10 minutes. The cells were resuspended in 3 mL of complete media supplemented with 10 units/mL of IL-2 and placed in the tissue culture incubator overnight [3, 104].

Additional fluorescent clones were prepared in a similar manner [3]. pEGFP-Vpr, a gift of Dr. Warner Greene (UCSF, San Francisco, CA), and pmm310, a gift of Dr. Michael Miller (Merck Research Laboratories), are available at the AIDS Research and Reference Reagent Program (Cat#11386 and Cat#11444, respectively). HIV Gag-iGFP Pr(-) and HIV Gag-iCherry Pr(-) were made by site-directed mutagenesis and are protease catalytic mutants carrying a double-alanine (D25A/T26A) mutation [108]. pNL4-3 MA/p6 was a gift of Christopher Aiken (Vanderbilt University, Nashville, TN). When needed, free viral particles were produced using standard calcium phosphate-mediated transfection of 293T cells [109]. Where noted, viral particles were produced in the presence of 2 μM Indinavir (AIDS Research and Reference Reagent Program, Division of AIDS, NIAID, NIH). Viral supernatants were quantitated by p24 ELISA and routinely yielded p24 concentrations of 400–1,000 ng/ml [3].

5.2 Live 3D imaging of HIV Gag-iGFP cell-to-cell transfer

Approximately 48 hours post-transfection, Jurkats expressing the fluorescent HIV clone were counted, washed with CO_2-independent media (Invitrogen, Carlsbad, CA),

and resuspended in live cell imaging media (CO_2independent media, 10% Fetal Bovine Serum, 100 U/mL penicillin, and 100 µg/mL streptomycin, 10 units/mL IL-2) at a concentration of 1-3 x 10^7 cells/mL. Primary, labeled CD4+ T cells were similarly washed and resuspended at a concentration of 1-3 x 10^7cells/mL in live cell imaging media. HIV-transfected Jurkats were mixed with primary CD4+ T cells at a 1:2 or 1:3 ratio and 30 µL of this mixture was loaded into a tissue culture treated, gas permeable, microchamber slide (Ibidi, Verona, WI) and sealed with plugs secured by wrapping the interface with parafilm.

Prepared slides were immediately mounted onto the spinning disk microscope described in Chapter 4.1, with a few minor modifications. Although live-cell imaging commonly uses expensive incubation chambers to maintain a stable 37°C environment, this was achieved using a simple and economical thermostatic heater (ASI 400, Nevtek, Williamsville, VA) along with a T-type thermocouple tip mounted next to the sample for proper temperature feedback. We have found using CO_2-independent media allows us to maintain high cell viability while avoiding the use of a CO_2 chamber. To buffer the platform against temperature fluctuations in the room and to block out background room light, a large black shroud is draped over the whole microscope/heater setup creating an insulated air pocket around the system. This greatly reduces temperature variation and associated temperature-related sample drift, but requires pre-heating for 30 minutes prior to mounting the sample.

To maximize the speed of acquisition to approximately 1.2-1.9 seconds per 3D image stack, we cropped the recording region of the EMCCD camera down to the cell-pair's immediate area. Furthermore, at the expense of some information in z, a large z-

step between 0.45-0.75 μm could be used to speed up acquisition. Cell-to-cell adhesions could typically be seen within 15 minutes of coculture, and imaging under these conditions could last up to 6 hours with continuous 20-60 minute imaging segments and minimal photobleaching. When two fluorescent markers were tracked, we simultaneously recorded both of them without slowing down acquisition by using a "split screen mode." We directly inserted an image splitter (OptoSplit II, Cairn, Kent, UK) that separates a single image into two by emission wavelength directly before the EMCCD camera. Each image is then independently filtered using fluorescence filters (Semrock) and projected side-by-side on the camera at once creating the "split-screen" effect. The images are later cropped and aligned manually. Altogether, each data segment typically occupied 5-20 Gb of space as tens of thousands of images were taken. To facilitate the transport and analysis of the large data files, each acquisition set was broken down and exported as 1 Gb TIFF image file segments using the Andor iQ v1.8 software [104].

Image analysis was performed using Volocity (PerkinElmer, Waltham, MA), an image processing program. Images were first adjusted in their intensity to correct for photobleaching, then deconvolved with Volocity. Intensity measurements and tracking of Gag puncta was performed with the Volocity Quantification module. For image sets where the movement relative to a pre-formed synapse needed to be calculated, an automated tracking algorithm was employed to tracks the synaptic button throughout the entire sequence. Manual inspection of the regions of interest defined by the autotracking software were performed to confirm that the software has correctly tracked the desired object. For objects where the contrast with the surrounding objects was too weak, manual tracking was performed on a frame-by-frame basis. The Volocity software

package allows the export of XYZ location, volume and integrated signal within the desired objects. The distance from the synapse and velocity of the tracked object were calculated by normalizing movements to the center of the synaptic button [104].

5.3 Monitoring viral membrane fusion by live cell imaging

For analysis of cell-free fusion, 293T cells were cotransfected with HIV Gag-iCherry and GFP-Vpr at a 3:1 ratio as described above. Approximately 500 ng/ml of filtered viral supernatant was added to adherent HeLa CD4+ cells for 2 hours at 17° C, a temperature that allows for binding but not fusion of the virus [110]. Cells were then washed gently and incubated at 37° C for 2 hours, fixed, and mounted on glass slides as described above. Analysis of viral membrane fusion was performed using Volocity image analysis software. Viral particles were identified using an automated image segmentation process that identified particles with a mean GFP fluorescence at least 30-fold over background. To quantitate membrane viral fusion in T cell cocultures, Jurkat T cells were cotransfected with HIV Gag-iCherry and GFP-Vpr at a 3:1 ratio and mixed with CellTracker Blue-labeled primary CD4+ T cells. Cells were incubated together for the indicated amount of time, trypsinized, sorted by flow cytometry (FACSAria, Becton Dickinson), and fixed on poly-L-lysine-coated glass coverslips. Viral particles were identified using the same criteria used in cell-free experiments, with the additional requirement that particles had a mean blue fluorescent signal at least 200-fold over background, indicative of their association with the cytoplasm of a target cell. After identification, all particles were visually inspected in three dimensions to confirm localization in acceptor cells. To image live viral fusion in acceptor cells engaged in a virological synapse, Jurkat T cells were cotransfected with HIV Gag-iCherry and GFP-

Vpr at a 3:1 ratio and mixed with primary CD4+ T cells in CO_2-independent media supplemented with 10% FBS and IL-2 (10 units/ml). Cells were loaded into Ibidi imaging chambers and imaged for up to 1 hour at various time points after initiating coculture. Cells were imaged at 37° C on the spinning disk microscope described in Chapter 4 to allow for rapid 3D time-lapse confocal imaging. To further reduce 3D imaging time to 1.5–3 seconds, we reduced the active area of the EM-CCD to the cell-pair region, approximately one-quarter of the 512 × 512 pixel area. iGFP and iCherry fluorescence emission were separated using the OptoSplit II image splitter described above [3].

5.4 Quantitation of viral membrane fusion by the BLaM assay

Cell-free viral fusion was quantitated as described in [111]. Briefly, HIV-1 virus was produced by cotransfecting 293T cells with wild-type proviral DNA (pNL4-3) and a plasmid (pMM310) that encodes β-lactamase fused to the amino terminus of Vpr at a 3:1 ratio. Fusion assays with cell-free virus were performed by adding virus (30 ng) to 2×10^5 cells in a volume of 200 μl for the indicated amount of time. Cells were washed and loaded with BLaM substrate CCF2-AM (1.5 μM) for 90 minutes at 25° C. Cells were then washed and incubated at 18° C in CO_2-independent media for 12 hours to allow for substrate cleavage. Finally, cells were washed in PBS, fixed in 3.7% formaldehyde, and read on an LSR II flow cytometer (Becton Dickinson, Franklin Lakes, NJ). Cleavage of CCF2-AM was determined by exciting cells with a 405 nm laser and recording emission at 450 nm (+/− 50 nm) and 525 nm (+/− 50 nm). Flow cytometry data was exported and analyzed using FlowJo software (Tree Star, Ashland, OR). Gates were set using untransfected cocultures. All conditions were background-subtracted. In

each experiment, control conditions were normalized to 100% and experimental conditions were expressed as a percentage of control. To assess cell-mediated fusion, 7×10^6 Jurkat T cells were transfected with pNL4-3/Vpr-BLaM (30 ng) at a 3:1 ratio. After 24 hours, transfected Jurkat cells were purified by Ficoll density gradient centrifugation as described above, and used as donor cells. These donor cells were mixed with Far Red-labeled CD4+ cells at a 2:1 ratio for the indicated amount of time. Cell cultures were then trypsinized, loaded with CCF2-AM, and processed for flow cytometry as described above [3].

5.5 Viral particle maturation assays as assessed by p17 staining

Jurkat T cells were transfected with HIV Gag-iGFP and mixed with Far Red-labeled CD4+ T cells; viral transfer was quantitated as described previously [18]. To measure the fraction of mature virus in acceptor cells, trypsinized cocultures were fixed in 3.7% formaldehyde, permeabilized in 0.05% saponin, and stained with a monoclonal antibody that recognizes p17 only in the context of mature virus [112, 113]. p17 staining was detected with a phycoerythrin (PE)-labeled secondary antibody that allowed for simultaneous detection of viral transfer (GFP) and maturation (PE) [3].

5.6 Viral particle maturation assays as assessed by FRET

For analysis of cell-free virus, 293T cells were cotransfected with HIV Gag-iGFP and HIV Gag-iCherry at a 1:1 ratio. Filtered viral supernatant was spotted onto poly-L-lysine coated glass coverslips and allowed to adhere for 15 minutes. Viral particles were fixed in 3.7% paraformaldehyde at room temperature for 15 minutes, rinsed with PBS, and mounted onto glass slides with ProLong Gold (Invitrogen, Carlsbad, CA). To measure particle maturation in acceptor cells following transfer across the VS, Jurkat

cells were cotransfected with HIV Gag-iGFP and HIV Gag-iCherry at a 1:1 ratio. These cells were mixed with CellTracker Blue (Invitrogen)-labeled primary CD4+ T cells at a 2:1 donor:acceptor cell ratio in the presence of AMD3100. Intracellular viral particles were identified in an automated fashion based on their colocalization with the cytoplasmic dye CellTracker Blue and confirmed visually in all three dimensions. Viral particles were imaged using a Leica SP5 DMI confocal microscope. Excitation lasers were 488 nm (GFP) and 561 nm (Cherry). Emissions were captured between 500 and 580 nm (donor) and between 590 and 650 nm (acceptor and FRET). Donor and acceptor bleedthrough constants were 2.7% and 10.4%, respectively [3]. Normalized FRET values were calculated as described previously [114].

Chapter 6 Cell-Cell Transfer of HIV-1 Promotes Efficient Viral Fusion with Kinetics and Inhibitor Sensitivity that Are Distinct from Cell-free Virus

Cell-to-cell transfer of HIV-1 via virological synapses leads to endosomal virion maturation that activates viral membrane fusion. During acute HIV-1 infection, patients experience a high-plasma viremia that is partially controlled by a vigorous but ultimately inadequate cellular and humoral immune response. Antibodies that can neutralize cell-free virus are detected in patient sera, but generally are ineffective against contemporaneous viral isolates circulating in patients [115]. How HIV-1 replication persists in the face of a vigorous immune response remains a perplexing and important question. Although most studies have focused on cell-free viral infection, direct cell-cell transfer of HIV-1 is more efficient and can resist neutralization by patient antibodies [16, 18]. Direct HIV-1 spread from T cell to T cell occurs through intercellular adhesive structures known as virological synapses (VS) [12, 18, 105] (see also Chapter 0 Chapter 5). VS formation is initiated when the viral envelope (Env) on the surface of an infected (donor) cell interacts with CD4 on an uninfected (acceptor) cell. Stabilization of the synapse requires Env/CD4 interactions, a dynamic cytoskeleton, and membrane cholesterol [116]. In addition, integrins, tyrosine kinases, and tetraspanin proteins accumulate at the VS [15, 51, 117]. These studies show that adhesion and cell signaling are important in mediating highly efficient HIV-1 dissemination from infected donor cells to acceptor CD4+ cells.

Following VS formation, the bulk of virus is transferred over several hours, resulting in the accumulation of virus in internal endocytic compartments of the acceptor cell [16]. However, the capacity of this intracellular virus to induce fusion has not been

examined. HIV-1 fusion is pH-independent. Early studies with cell-free virus indicated that fusion did not require endocytosis and was likely to occur predominantly at the plasma membrane [118, 119]. More recent studies have indicated that the endosomal compartment may play a significant role in promoting viral entry. Inhibition of the endocytic apparatus by expressing the dominant-negative forms of eps15 or dynamin reduced cell-free viral infection by 40%–80% [120]. More recently, Miyauchi et al. have used peptide inhibitors and live cell imaging to demonstrate that cell-free HIV-1 fusion occurs prominently in endosomes [22].

We used a combination of flow cytometry and fluorescence microscopy to demonstrate that HIV-1 particles undergo viral membrane fusion following transfer across the VS. We unexpectedly found that cell-mediated viral fusion occurs with a substantial kinetic delay compared to cell-free virus. Detailed analysis using immunostaining and viral mutants demonstrated that HIV-1 particles transfer across the VS in an immature form and then mature within the endosome. Furthermore, we find that viral maturation plays an essential regulatory role in activating viral membrane fusion within this intracellular compartment. Our results support a model whereby the activation of Env fusogenicity occurs primarily within the T cell endosome and may sequester key fusogenic epitopes from recognition by neutralizing antibodies.

6.1 Cell-to-cell transfer of HIV-1 promotes efficient viral fusion with kinetics and inhibitor sensitivity that are distinct from cell-free virus

To study the ability of HIV-1 particles to induce viral membrane fusion after internalization through the VS, we employed the Vpr-β-lactamase (Vpr-BlaM) enzymatic assay for measuring viral fusion [111, 121]. In this assay, expression of Vpr-BlaM in

HIV-infected cells results in packaging the enzyme into nascent virus particles. Fusion of these particles with substrate-loaded target cells releases the enzyme into the cytoplasm, where the sequestered BlaM substrate is cleaved. Detection of the cleaved substrate by flow cytometry provides an indicator of viral fusion activity. We first measured the ability of high-titer, cell-free virus, which was produced by transfection of 293T cells, to initiate viral membrane fusion with CD4+ T cells. We note that the levels of cell-free virus that produce a robust fluorescence shift are typically 50- to 100-fold higher than that released from transfected Jurkat cells during a routine 4–8 hour coculture experiment. When MT4, a highly permissive T cell line, was exposed to cell-free Vpr-BlaM HIV-1, we detected viral fusion activity in 5%–10% of cells as a fluorescence wavelength shift using flow cytometry (Figure 6.1 A).

To measure viral membrane fusion following cell-to-cell transfer of HIV-1, we used Jurkat T cells, cotransfected with pNL4-3/Vpr-BlaM, as HIV-expressing donor cells. These cells were cocultured with DDAO Far Red-labeled MT4 cells and viral fusion activity was similarly detected in the T cell line (Figure 6.1 B). Separation of the donor and acceptor cells with a porous membrane that is permeable to virus but impermeable to the MT4 cells reduced fusion activity to background levels, suggesting that cell contact or close proximity was required (Figure 6.1 C). Interestingly, BlaM activity in target cells increased faster following exposure to cell-free virus compared to cell-associated virus. Fusion of cell-free virus was rapid; approximately 50% of maximal fusion activity occurred within 2 hours and greater than 80% of all fusion occurred within 4 hours (Figure 6.1 D). In contrast, the kinetics of fusion following transfer across the VS was comparatively slow, with only approximately 10% of maximal fusion activity

occurring within the first 2 hours and less than 50% of maximal fusion activity was observed within 4 hours (Figure 6.1 D). In addition to measuring viral membrane fusion activity with the CD4+ T cell line, MT4, as the VS-target cell (Figure 6.1), we also observed viral membrane fusion activity after exposure of primary CD4+ T cells to either cell-free or cell-associated HIV-1 (Figure 6.2).

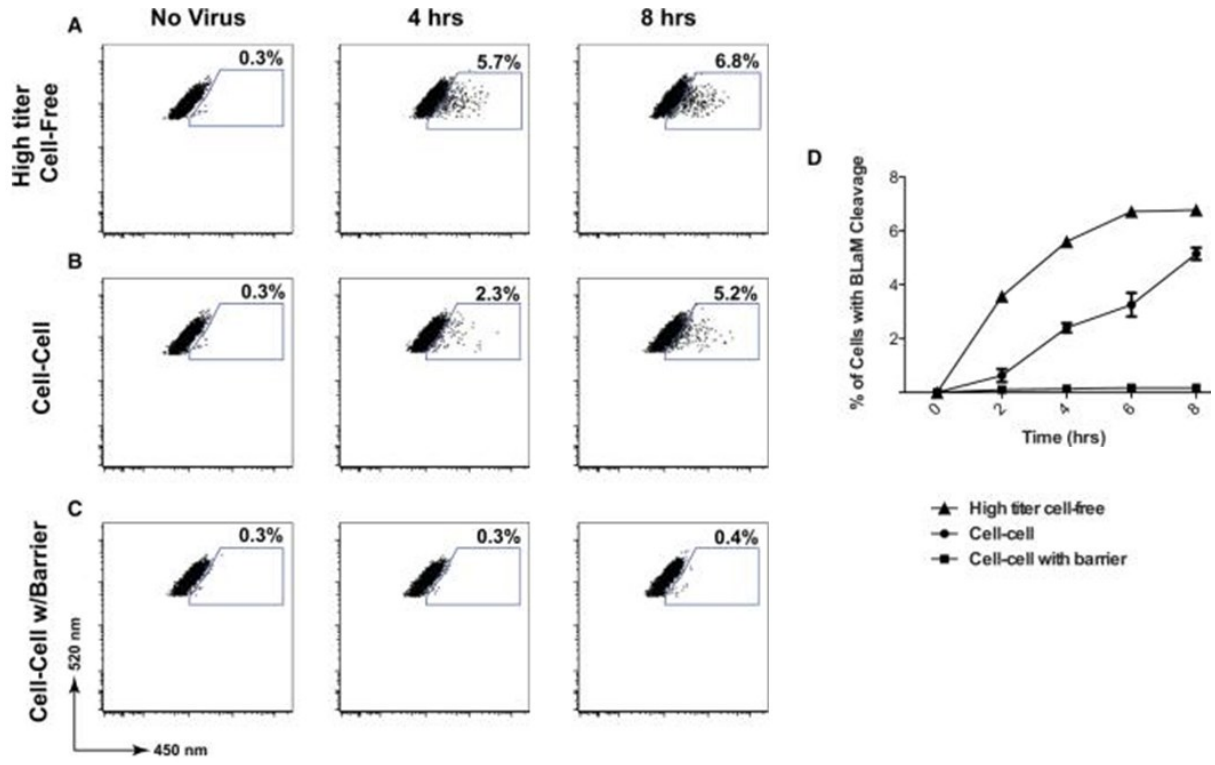

Figure 6.1 Cell-cell transfer of HIV-1 promotes efficient viral fusion with kinetics that are distinct from cell-free virus. (A–D) The CD4+CXCR4+ T cell line MT4 was incubated with either 30 ng (150 ng/ml) of HIV-1/Vpr-BlaM cell-free virus particles (A), Jurkat cells expressing HIV-1/Vpr-BlaM (B), or Jurkat cells expressing HIV-1/Vpr-BlaM separated by a porous membrane that is permeable to virus yet impermeable to T cells (C). After incubation for the indicated amount of time, viral fusion was detected by the fluorescence shift associated with cleavage of the BLaM substrate CCF2-AM as described in Experimental Procedures. Representative FACS plots are shown in (A–C) and a time course is shown in (D). Results in (A–C) are representative of four independent experiments. Data in (D) are results from a representative experiment, done in triplicate and depicting the mean fusion for each time point ± SEM after subtracting from background values (left column, A–C). See also Figure 6.2.

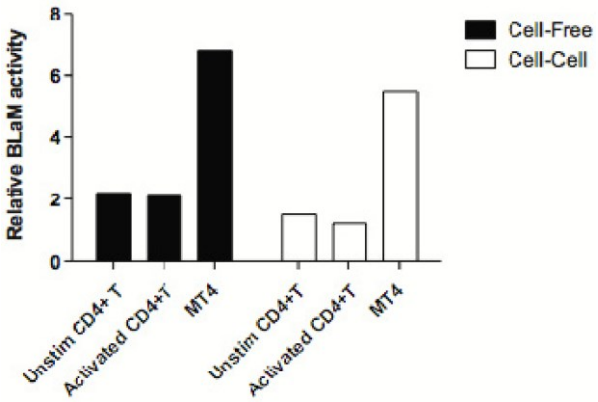

Figure 6.2 Viral membrane fusion in primary CD4+ T cells occurs following exposure to cell-free and cell-associated HIV-1. Aliquots of $2x10^5$ unstimulated primary human CD4+ T cells, PHA-activated primary human CD4+ T cells, or MT4 cells were incubated with either HIV-1/Vpr-BLaM viral particles (cell-free, 150 ng/ml) or Jurkat cells expressing HIV-1/Vpr-BlaM (Cell-Cell) for eight hours. Viral fusion was assessed with the BLaM substrate CCF2-AM as described in Chapter 5. Results are representative of 3 independent experiments.

We next sought to test the ability of patient sera and a fusion inhibitor to block viral fusion after exposure to cell-free and cell-associated HIV-1. As expected, the CXCR4-targeted fusion antagonist AMD3100 was able to block viral membrane fusion from both cell-free virus and VS-transferred HIV-1 (Figure 6.3 B and E). Importantly, AMD3100 does not affect the bulk, CD4-dependent transfer of HIV-1 between T cells [18]. We have previously demonstrated that patient sera that neutralize 90%–100% of cell-free infection can have little or no effect on the bulk transfer of HIV-1 particles from T cell to T cell [18]. At the same concentration, the same patient sera are capable of blocking only 40%–50% of cell-mediated productive infection [16]. Here, employing the Vpr-BlaM assay, we found that polyclonal patient sera at a 1:50 dilution was able to block nearly 100% of cell-free viral fusion but only approximately 50% of viral fusion following transfer across the VS (Figure 6.3 C and 2 E). Control human sera had no inhibitory effect on viral fusion induced by either cell-free or cell-associated virus at this concentration (Figure 6.3 D and 2 E). Taken together, these results suggest that a

polyclonal mixture of HIV-1 antibodies is less effective at blocking viral fusion when the virus transfers across a synapse.

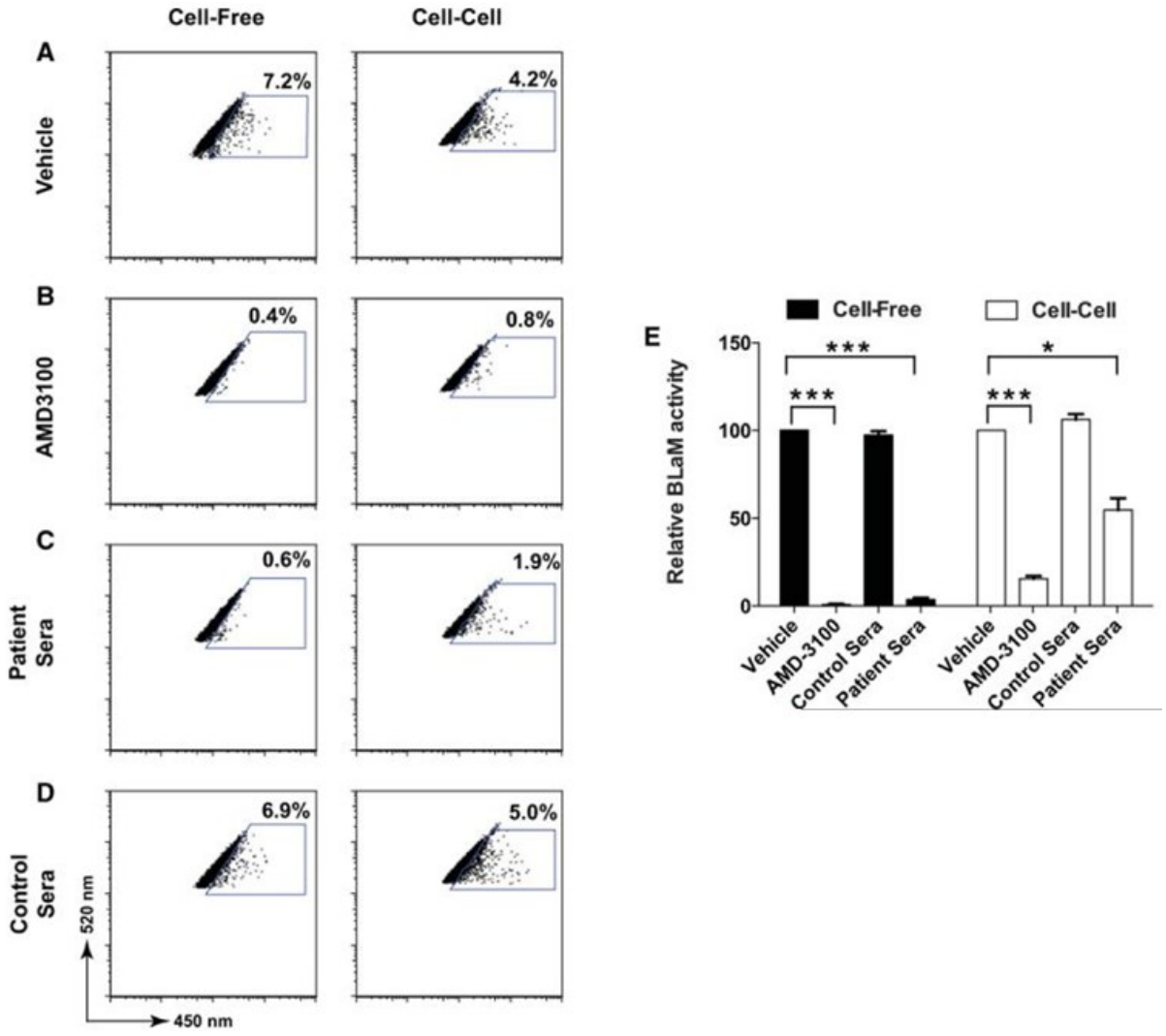

Figure 6.3 Viral fusion in target cells after exposure to cell-free and cell-associated virus exhibit distinct sensitivities to patient sera. MT4 cells were incubated with either 30 ng (150 ng/ml) of HIV-1/Vpr-BlaM viral particles (cell-free) or Jurkat cells expressing HIV-1/Vpr-BlaM (cell-cell). After a 6 hour coculture, viral fusion was assessed with the BLaM substrate CCF2-AM as described in the experimental procedures. (A) Control fusion assay treated with vehicle (DMSO) alone. (B) Fusion assay treated with fusion antagonist AMD3100. (C) Fusion assay treated with neutralizing nonimmune antisera. (D and E) (D) Fusion assay treated with control patient antisera. Representative FACS plots are shown in (A–D) and a summary of data pooled from five independent experiments is shown in (E). All data was corrected for a background of 0.4% and normalized to control conditions. Data in (E) represent mean ± SEM (n = 5). *p < 0.05; **p < 0.01; ***p < 0.001.

The ability of Env to mediate viral membrane fusion is regulated by the maturation state of the virus particle [122-125]. Immature viral particles were reported to be poorly fusogenic, and cleavage of the Gag protein correlated with enhanced fusion activity. To determine whether the delay in fusion kinetics of cell-associated HIV-1 reflects a requirement for particle maturation, we used the HIV-1 protease inhibitor Indinavir (IDV) to disrupt the viral maturation process. IDV had little effect on the fusion induced by mature cell-free virus (Figure 6.5 B and D). This was expected because virus harvested from transfected 293T cells (typically at 48 hours post-transfection) is for the most part already fully processed and should not be sensitive to protease inhibitors [107]. Surprisingly, IDV blocked 70% of viral fusion following infection with cell-associated HIV-1 (Figure 6.5 B and D). The requirement for viral protease activity in viral fusion during both cell-free and cell-mediated infection is further supported by the observation that protease-deficient viral mutants were unable to mediate fusion (Figure 6.4 A).

To control for the possibility that the incorporation and/or maximal activity of BlaM in viral particles may require viral protease, we used pNL4-3 MA/p6, a pNL4-3 clone that not only has wild-type protease but also carries Gag mutations that prevent its cleavage by HIV-1 protease [125]. The pNL4-3 MA/p6 virus produced viral particles with efficiency similar to that of wild-type virus but the particles did not undergo maturation (Figure 6.4 B). Both cell-free and cell-mediated viral fusion assays with pNL4-3 MA/p6 confirmed that cleavage of Gag by viral protease was essential for viral fusion after infection with cell-free or cell-associated HIV-1 (Figure 6.5 C and D). Consistent with our viral fusion data, we found that IDV inhibited productive infection by coculture with cell-

associated HIV-1 but not by exposure to mature cell-free virus that had already undergone proteolytic maturation (Figure 6.4 C).

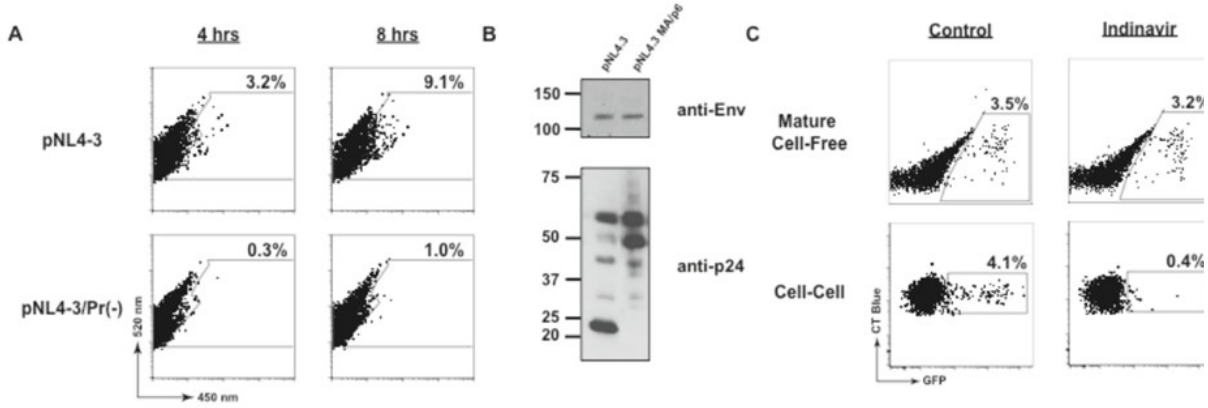

Figure 6.4 Viral protease is essential for cell-mediated viral membrane fusion and productive infection. (A) Jurkat T cells were co-transfected with either pNL4-3/Vpr-BlaM or pNL4.3Pr(-)/Vpr-BlaM and cocultured with MT4 cells. Viral membrane fusion was assessed with the BlaM assay as described in Experimental Procedures. Results are representative of three independent experiments. (B) Preparation of pNL4-3 and pNL4.3 MA/p6 viral particles. Virus particles were purified by pelleting through a 20% sucrose cushion, resolved on 4-12% NuPage gradient gels (Invitrogen), transferred to nitrocellulose, and immunoblotted with antibodies against Env (Top) or p24 (Bottom). (C) (Top) Mature cell-free GFP-expressing HIV-1, clone NL-GI, was used to infect MT4 cells in the presence and absence of Indinavir. Cells were exposed to virus at a concentration of 200 ng/ml for 2 hours before washing and culturing for an additional 28 hrs. (Bottom) Jurkat T cells were transfected with NL-GI as described in and co-cultured with CellTracker Blue labeled MT4 cells for 30 hours in the presence and absence of Indinavir. Infection of CellTracker Blue stained target cells is shown. Quantitation is described in Chapter 5. Results are representative of two independent experiments.

6.2 The virological synapse promotes the transfer of immature viral particles to acceptor cells, where they undergo protease-dependent maturation

Multiple factors could partially account for the kinetic delay seen in VS-promoted fusion, including the time that it takes to form cell-cell contacts. However, the requirement for viral protease in viral membrane fusion (Figure 6.5 B–D and Figure 6.4 A) suggested to us that HIV-1 particles are transferred to CD4+ T cells in an immature

state and subsequently undergo maturation within target cell endosomes over a period of hours. Importantly, published pulse-chase studies have demonstrated that full HIV-1 viral maturation takes place over time periods up to 8 hours [126]. To test whether viral maturation could occur in intracellular compartments of acceptor cells following transfer across the VS, we monitored particle maturation following transfer across the VS with a monoclonal antibody that recognizes cleaved p17 but not the p55 Gag precursor [112, 113].

Jurkat T cells transfected with HIV Gag-iGFP, a GFP-tagged infectious clone of HIV-1, were mixed with uninfected Far Red-labeled primary CD4+ cells. Monitoring the GFP and anti-p17-phycoerythrin (PE) signals in the Far Red-labeled acceptor cells allowed us to simultaneously monitor the transfer and maturation of virus following transfer across the VS. As assessed by the percentage of acceptor CD4+ T cells with a GFP signal, cell-cell transfer of HIV-1 was efficient and nearly achieved a steady state at 4 hours. For example, 40.8% of acceptor cells were GFP+ at 4 hours and 44.8% of acceptor cells were positive at 8 hours (Figure 6.6 B and F). During this time frame, the fraction of p17+ cells increased modestly (from 11.0% to 13.9%) and only a fraction of the cells that took up virus showed strong intracellular p17 staining (Figure 6.6 B and G). In stark contrast, cells treated with AMD3100 showed an increase in p17 staining (from 18.9% to 36.7%) over this time period, providing evidence of maturing virus within cell confines (Figure 6.6 C and G). Thus, blocking fusion with AMD3100 enhanced the accumulation of mature virus particles in acceptor cells. IDV blocked the accumulation of cleaved p17 in acceptor cells at all time points (Figure 6.6 D and G), confirming the specificity of this monoclonal antibody. Likewise, examination of a protease-deficient

virus revealed no accumulation of p17 (Figure 6.6 E and G). Thus, accumulation of mature virus in intracellular compartments was completely dependent upon HIV-1 protease and was further increased by preventing viral fusion. To rule out the effect of the Gag-iGFP on particle maturation, we also conducted the same maturation experiments with a non-GFP tagged wild-type virus and demonstrated viral maturation in acceptor cells with kinetics similar to the HIV-Gag-iGFP virus, available in [3]. Combined with the kinetic data shown in Figure 6.1, these data strongly suggest that HIV-1 undergoes protease-dependent maturation over a period of hours following transfer across the VS and before undergoing viral membrane fusion.

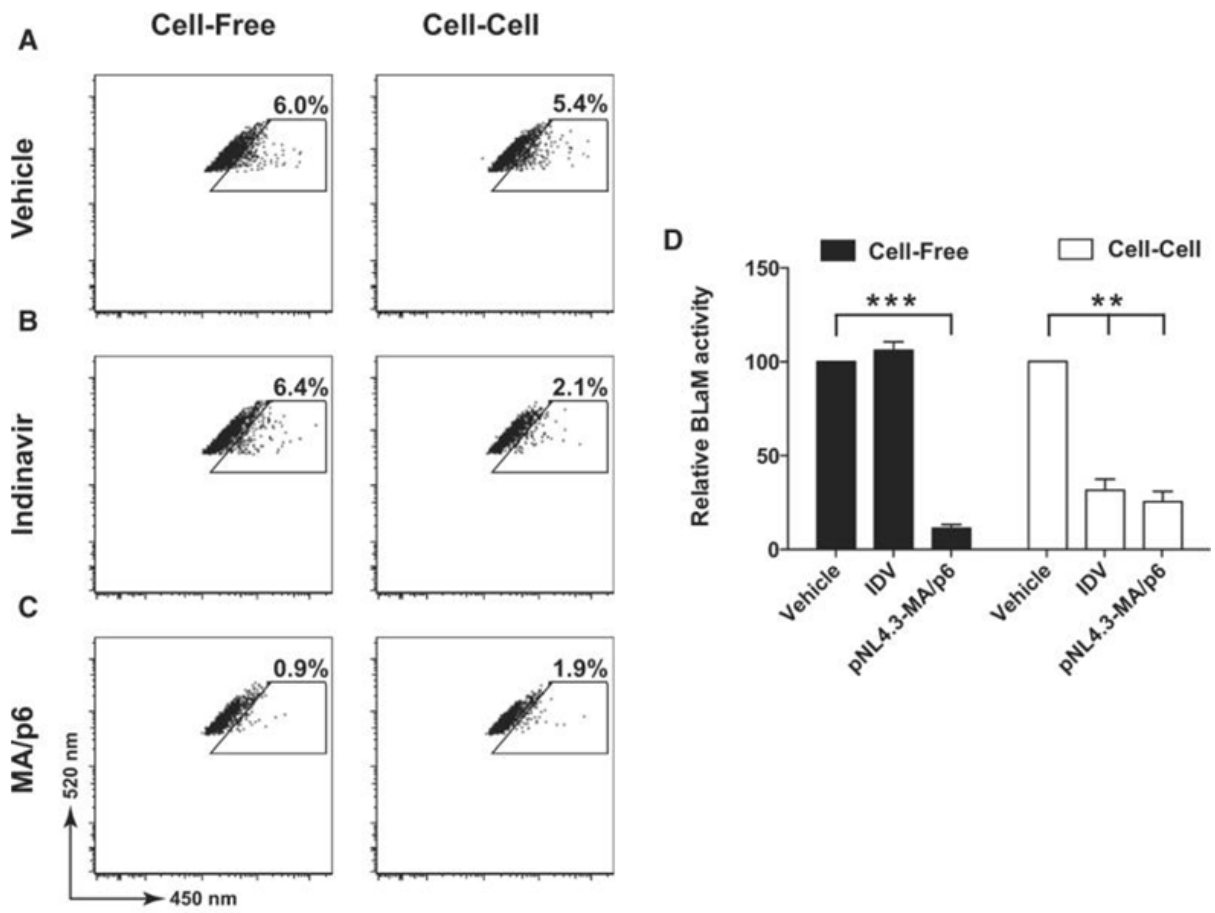

Figure 6.5 Viral fusion in target cells after exposure to cell-free and cell-associated virus exhibits distinct sensitivities to protease inhibitor. Fusion assays were performed as in Figure 2. (A) Control fusion assay treated with vehicle (DMSO) alone. (B) Fusion assay treated with Indinavir, an HIV protease inhibitor. (C) Fusion assay performed using a mutant virus with MA-p6a, a noncleavable Gag. Representative FACS plots are shown in (A–C), (D) A summary of data pooled from five independent experiments is shown. Data in (D) represent mean ± SEM (n = 5). *p < 0.05; **p < 0.01; ***p < 0.001. All data were corrected for a background of 0.4% and normalized to control conditions. See also Figure 6.4.

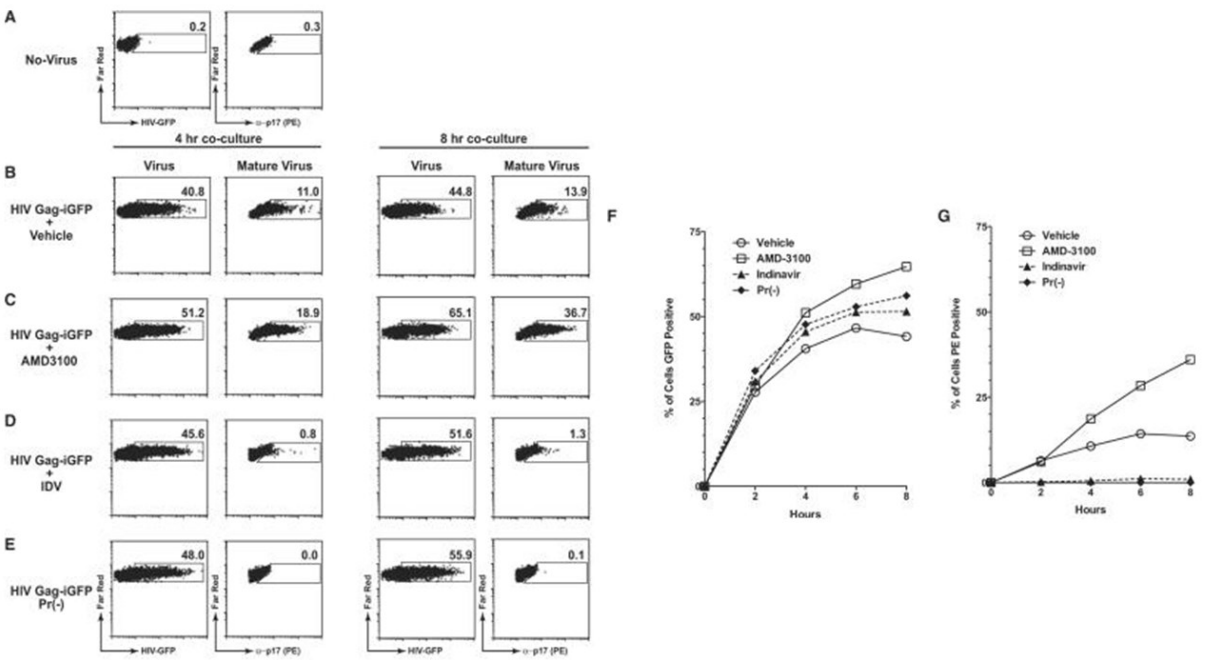

Figure 6.6 HIV-1 undergoes maturation in acceptor cells over time following transfer across the virological synapse. Jurkat T cells were transfected with HIV Gag-iGFP and mixed with Far Red-labeled primary CD4+ cells as described in Experimental Procedures. At the indicated times, cells were permeabilized and stained with a monoclonal antibody that recognizes the viral protein p17 only in the context of mature virus. Representative FACS plots illustrate the total virus transferred and the mature virus transferred at 4 or 8 hours. (A) Primary CD4+ target cells after mixture with untransfected Jurkat cells. (B) HIV-1 cell-cell transfer and maturation assays treated with vehicle (DMSO) alone. (C) Assay conducted in the presence of fusion antagonist AMD3100. (D) Assay conducted in the presence of Indinavir (IDV), a protease inhibitor. (E) Assays performed with a viral mutant carrying a mutation in the catalytic site of protease, Pr(−). (F) Time course of virus transfer. (G) Time course of virus maturation. Data in (F) and (G) are results from a representative experiment done in triplicate, depicting the mean values ± SEM. In all conditions, SEM < 1 and is smaller than the symbol size. Time course experiments are representative of four independent experiments.

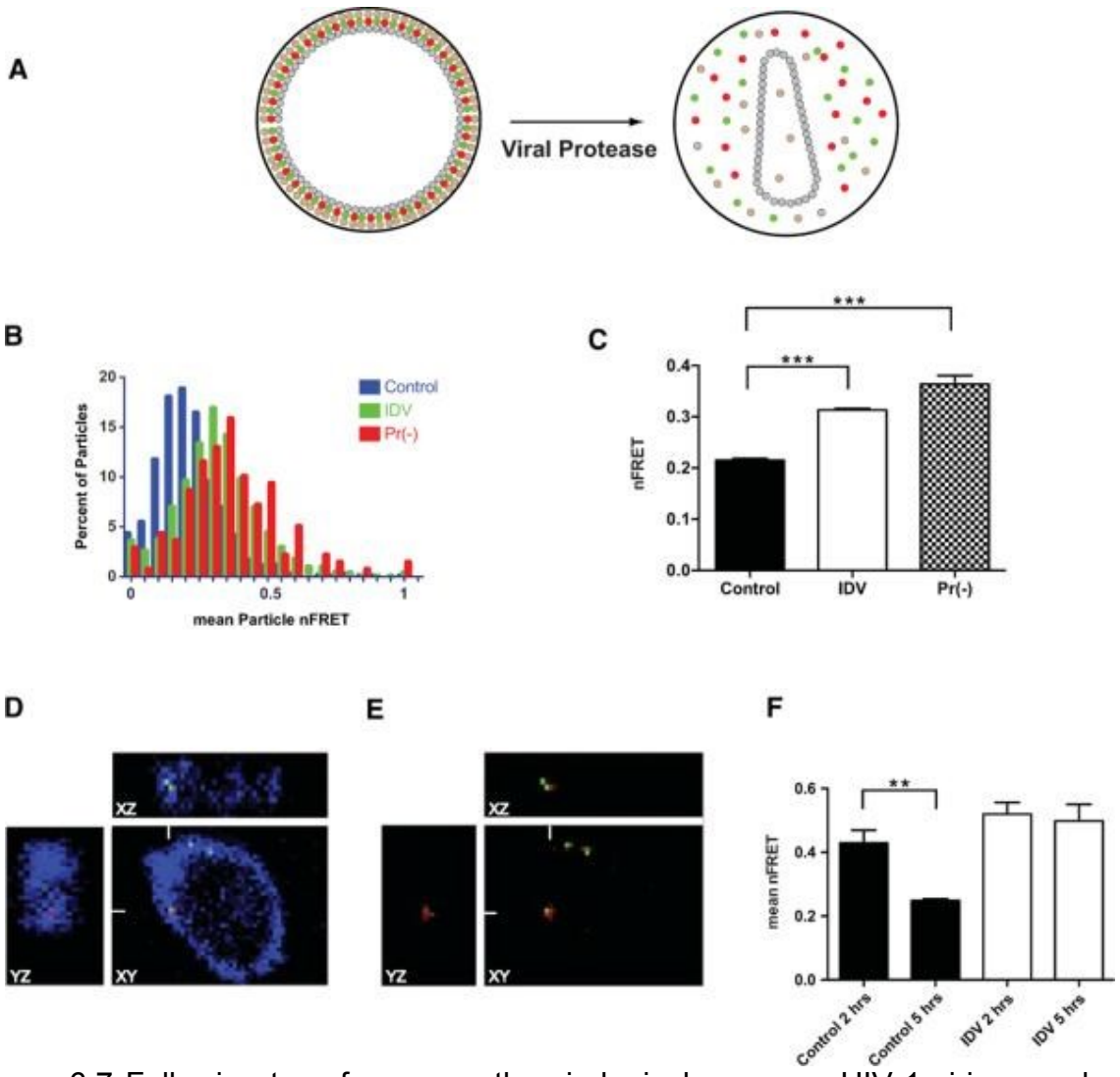

Figure 6.7 Following transfer across the virological synapse, HIV-1 virions undergo maturation in intracellular compartments. (A) Diagram depicting the arrangement of fluorescent monomers in viral particles made from HIV Gag-iGFP and HIV Gag-iCherry. FRET is predicted to be highest in immature particles and lower following cleavage at protease sites during maturation. (B and C) 293T cells were cotransfected with HIV Gag-iGFP and HIV Gag-iCherry at a 1:1 ratio (n = 1,400). Viral particles were harvested and imaged as described in Experimental Procedures. The distribution of nFRET values for the particles is shown in (B) and the mean nFRET values for each condition is shown in (C). (D–F) Jurkat T cells were cotransfected with HIV Gag-iGFP and HIV Gag-iCherry at a 1:1 ratio and mixed with CellTracker Blue-labeled primary CD4+ T cells for 2 or 5 hours in the presence of AMD3100. Cells were fixed and imaged as described in Experimental Procedures. A representative acceptor cell is shown in (D and E), and the quantification of particle nFRET values (n = 60) in acceptor cells following coculture is shown in (F). Data in (B), (C), and (F) are from single experiments that were each representative of three independent experiments. (C) and (F) are represented as an experimental mean ± SEM. *p < 0.05; **p < 0.01; ***p < 0.001.

6.3 Protease-dependent maturation occurs in an intracellular compartment following transfer across the virological synapse

To determine where in the target cell the maturation of virus particles takes place, we developed an additional maturation assay that is based upon fluorescence resonance energy transfer (FRET). We used HIV Gag-iGFP and HIV Gag-iCherry, which respectively carry GFP or Cherry fluorescent protein fused internally into Gag. Because GFP and Cherry can function as a donor acceptor FRET pair, the FRET signal between these fluorophores provides a measure of Gag-Gag interactions [107]. In a dual-labeled immature viral particle, fluorophores are packed within a Gag lattice that generates a maximum FRET signal **(**Figure 6.7 A). Because GFP in Gag-iGFP is flanked by protease recognition sites, it is cleaved apart from the Gag polypeptides during the maturation process, releasing it from the constraints of a tight Gag lattice [107]. Thus, the level of FRET in mature viral particles would likely be lower than in immature particles. We tested this first by examining viral particles that had been produced in 293T cells by cotransfection of HIV Gag-iGFP and HIV Gag-iCherry. Blocking the virus maturation process, either by using a protease-deficient virus or treating producer cells with IDV, significantly enhanced viral particle FRET (Figure 6.7 B and C). We then used these observations to directly test our hypothesis that viral maturation takes place in intracellular compartments of acceptor CD4+ T cells. Jurkat T cells were cotransfected with HIV Gag-iGFP and HIV Gag-iCherry and mixed with primary CD4+ T cells. Cocultures were incubated at 37°C for 2–5 hours prior to imaging by confocal microscopy (Figure 6.7 D and E). After particles were transferred across VS, they exhibited a time-dependent decrease in nFRET from 2 to 5 hours, consistent

with progressive Gag processing over time (Figure 6.7 F). Target cells treated with IDV showed no change in nFRET over time, suggesting that the loss of nFRET that we observed is dependent on viral protease activity (Figure 6.7 F). These results suggest that the particle maturation seen in acceptor cells takes place in an endocytic compartment.

6.4 HIV-1 fusion can occur within an intracellular compartment following transfer across the virological synapse

We next sought to further examine how and where viral particles transferred across the VS into endosomes may undergo viral membrane fusion. We made use of the fact that HIV Vpr associates with the viral core following viral membrane fusion [127]. Infection of cells with virus that has packaged a GFP-Vpr fusion protein enables one to track the movement of the viral core through the cytoplasm to the nucleus [128]. We generated dual-labeled (HIV Gag-iCherry and GFP-Vpr) fluorescent virus that served as a real-time reporter of viral fusion. Because the Cherry molecule cleaves away from Gag during particle maturation [107], we expect that a fusion event is characterized by the Cherry signal's loss of colocalization with GFP-Vpr, due to the release of the contents of the viral particle. Thus, during a fusion event, a dual-labeled (yellow) particle undergoes a loss of Cherry signal associated with the GFP-VPR associated core (Figure 6.8 A and D). A similar labeling strategy that generates fluorescent protein cleaved from Gag protein has been employed to monitor HIV fusion in HeLa CD4+ T cells (MA-GFP-CA virus [22]. We validated our approach by producing HIV Gag-iCherry/GFP-Vpr particles from 293T cells and incubating them with HeLa CD4+ cells, allowing viral membrane fusion to proceed for 2 hours at 37°C. Quantitative

confocal imaging of the cells allowed us to assess the relative intensity of GFP and Cherry in viral puncta, which may represent individual or small clusters of viral particles. In a typical control experiment, approximately 1,400 viral particles are identified by the presence of a GFP-Vpr signal using an automated image segmentation algorithm, and the mean Cherry fluorescence associated with each of these particles was calculated (Figure 6.8 B and C). In the presence of AMD3100, the mean Cherry particle fluorescence was 21% greater than that in the control conditions (Figure 6.8 C). This result is consistent with AMD3100-sensitive fusion events occurring in the HeLa target cells.

In addition to observing a change in the mean fluorescence of all viral puncta, we observed a shift of some individual viral puncta to a lower level of mean red fluorescence compared to cells treated with AMD3100. This was especially notable when examining particles with a lower GFP signal, which more likely may represent single particles. In control conditions, 6.7% of puncta were found to be low in Cherry fluorescence compared to 1.1% in those treated with AMD3100 (Figure 6.8 B). This analysis suggests that we may be able to detect some fusion events that lose nearly the entire Cherry signal.

To determine if viral fusion can be detected in individual particles following viral transfer across the VS, Jurkat T cells were cotransfected with HIV Gag-iCherry and GFP-Vpr and cocultured with primary CD4+ cells in the presence or absence of AMD3100. Importantly, under these conditions HIV-1 is predominantly intracellular, as assessed by trypsin sensitivity or antibody accessibility [18, 107]. Cells were fixed after either 2 or 6 hours and examined for Cherry signal associated with GFP-Vpr signal

within target cells. When comparing control conditions to AMD3100-treated conditions, we observed no difference in the Cherry signal associated with the GFP-Vpr signal at 2 hours (data not shown). However, at 6 hours the mean Cherry fluorescence signal associated with GFP-Vpr puncta in AMD3100 conditions was 24% greater compared to control conditions (Figure 6.8 F). Thus, we observed an AMD3100-sensitive loss of Cherry from viral puncta, with kinetics similar to those observed using the Vpr-BlaM fusion assays (Figure 6.1). In contrast to the HeLa cells, the appearance of puncta with low levels of red fluorescence was less prominent in CD4+ T cells. When considering the particles with the lowest Vpr-GFP signal (which are more likely to be single particles), 6.5% of puncta in the untreated conditions had low Cherry fluorescence (indicative of viral fusion) compared with 3.1% of puncta in AMD3100-treated cells (Figure 6.8 E). Therefore, we conclude that AMD3100 inhibits the dissociation of Cherry signal from GFP-Vpr puncta in VS target cells after 6 hours. We interpret this as additionally supportive of viral membrane fusion occurring from an intracellular location.

To directly visualize individual fusion events following cell-to-cell transfer of HIV, we conducted live cell 3D spinning disk microscopy on dual-labeled particles after they crossed the VS, focusing our attention on tracking smaller viral puncta in acceptor-cell endosomes rather than larger clusters of virus (Figure 6.8 G). We imaged approximately 60 hours of live viral transfer across the VS, tracking 225 viral particles. We collected data on cells that had been in coculture over a wide time frame (0–8 hours), with particular emphasis on later time points, when acceptor cells had accumulated mature virus particles (Figure 6.6). Five putative fusion events were identified, all observed during a 4–6 hours window following cell-cell mixing. These fusion events were

identified by a rapid loss of Cherry signal relative to neighboring viral puncta; neighboring puncta displayed no such loss of Cherry signal (Figure 6.8 H–K). One putative fusion event occurred in two stages over a period of 5 minutes, perhaps indicative of two fusion events occurring from the same virus-containing compartment (Figure 6.8 I, video available at [3]). In all cases, the Cherry fluorescence of nearby particles remained stable, as did the GFP signal, suggesting that our observations could not be explained by photobleaching (Figure 6.8 J). Other putative fusion events showed a very rapid loss of Cherry (Figure 6.8 K). Four of the five putative fusion events exhibited a loss of more than 80% of the Cherry signal, while a fifth event exhibited a loss of 50% of the signal and then stabilized. We determined the distance of each fusion event from the center of the Gag synaptic button and mapped them schematically on a diagram of two synapsing cells. This map depicts our finding that four of the five fusion events occurred within intracellular compartments, microns away from the synaptic button, and one occurred in closer proximity to the VS (Figure 6.8 L). Although the detection of fusion at a distance from the synaptic button suggests these particles do not fuse at the synaptic interface, it should be noted that intense fluorescence from the donor cell could obscure the visualization of dim fusion events near the synaptic junction.

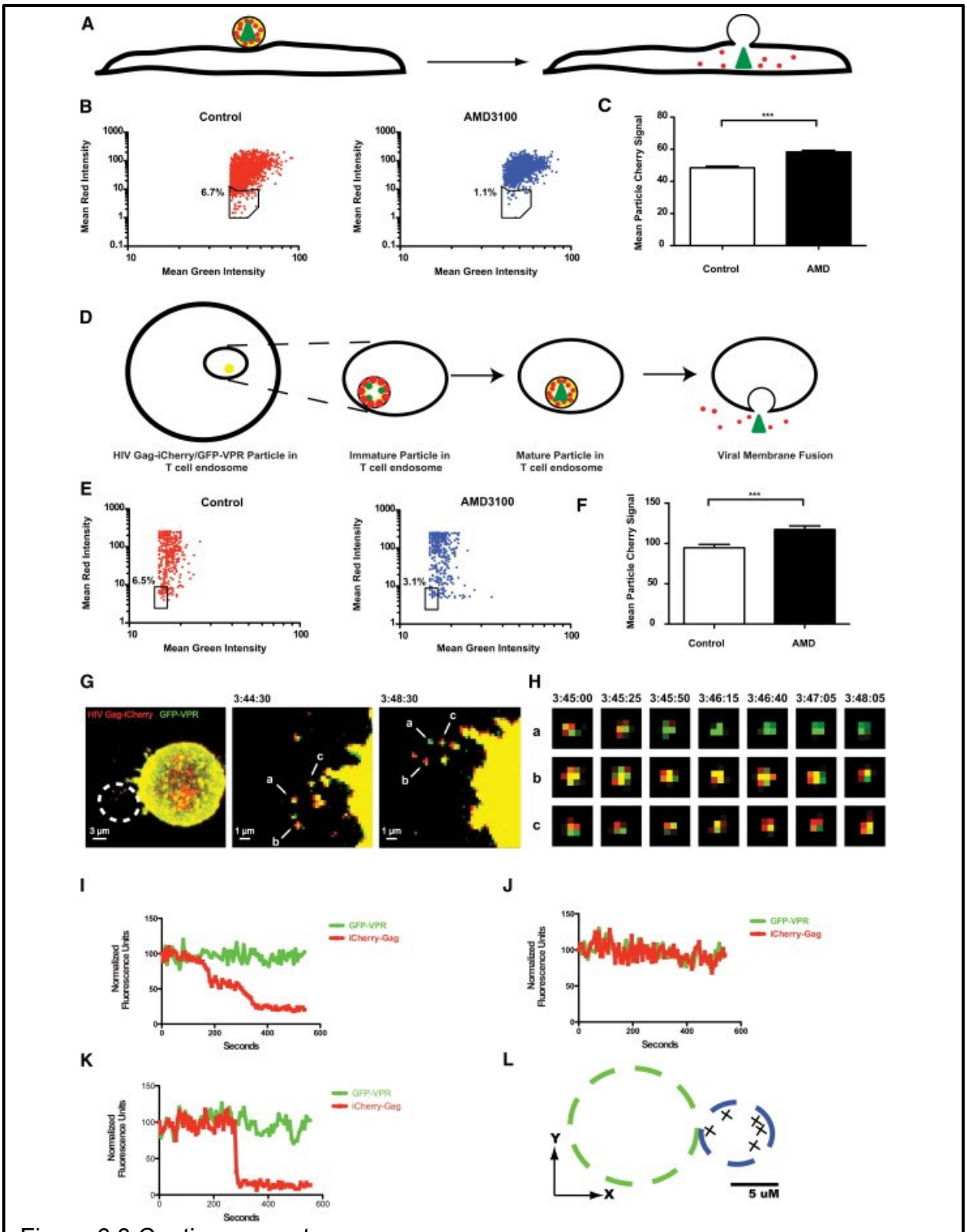

Figure 6.8 Caption on next page.

Caption for Figure 6.8. Fusion of HIV-1 from endosomes following transfer across the virological synapse. (A) Schematic depiction of HIV Gag-iCherry/GFP-Vpr during cell-free fusion with a HeLa CD4+ cell. In a mature virus particle, Cherry fluorescent protein is cleaved from Gag monomers but remains within the virus particle. Upon viral membrane fusion, the Cherry signal diffuses away while the GFP-Vpr remains associated with the viral core. (B and C) HeLa CD4+ cells were treated with HIV Gag-iCherry/GFP-Vpr (500 ng/ml) and automated image analysis was used to measure the Cherry signal associated with the GFP signal. Results are shown on a single-particle basis (B) or as the mean Cherry signal associated with each particle (C). Control mean, 48.5; AMD3100 mean, 58.4; n = 1,416; $p < 0.001$. (D) Schematic depiction of HIV Gag-iCherry/GFP-Vpr following transfer across the VS. After transfer, particles undergo maturation and then viral membrane fusion. (E and F) Jurkat T cells expressing HIV Gag-iCherry and GFP-Vpr were cocultured with CellTracker Blue-labeled primary CD4+ T cells for 5 h. The cells were trypsinized and purified by FACS sorting, then imaged using confocal microscopy. Results from automated image analysis of the Cherry signal are shown on a single particle basis (E) or as the mean signal associated with each particle (F). Control mean, 94.7; AMD3100 mean, 117.3; n = 382; $p < 0.001$. (G–L) Live-cell imaging of particle fusion at the VS. A cotransfected Jurkat T cell is shown forming a VS with an acceptor CD4+ T cell (dotted line) (left) (G). Several particles were chosen for tracking (particles a, b, and c). An extended focus view of the particles at the beginning (G, center) and end (G, right) of a tracking period is shown, and a series of frames for the three particles is shown in (H). Particles a and b are quantitated in (I and J), respectively. (K and L) A putative single viral membrane fusion event showing the rapid loss of Cherry signal from the viral particle (K). The two-dimensional diagram in (L) shows the approximate localization, relative to VS, that 5 of 225 fusion events transferred particles during live cell imaging. See also the video in [3].

6.5 Discussion

To better understand how virological synapse-mediated infection differs from cell-free infection, we have followed the fate of viral material that is transferred across synapses into target CD4+ T cells. An earlier investigation showed that HIV-1 localizes in trypsin-inaccessible intracellular compartments shortly after it moves across the VS [18, 105]. Although the exact nature of this compartment is unknown, recent data suggest that HIV-1 is transferred to nonlysosomal compartments [24] (G.P.M., B.M.D., and B.K.C., unpublished data). This suggests that, following transfer across the VS, HIV-1 can access a compartment in acceptor CD4+ T cells that is compatible with

maturation and fusion. Given the tight temporal linkage of virus assembly with internalization into the target cell, we found that the internalized viral particles are initially immature and nonpermissive for viral membrane fusion. Following a delay that included HIV-1 protease-dependent processing, we observed efficient viral membrane fusion. Overall, our study supports a model whereby the process of particle maturation is critical for the activation of viral membrane fusion following transfer across a virological synapse (Figure 6.9).

Because virus particle morphogenesis and transfer into a target cell occur almost simultaneously, the maturation of HIV-1 particles occurs within the confines of an endocytic compartment. Compelling studies by the Aiken and Murakami groups have found that particle fusogenicity is tightly linked with the maturation state of the virus particle when considering cell-free virus particles [123, 125]. Our study places this model of maturation-induced fusion into a unique context where maturation occurs after the virus has already engaged CD4 and is sequestered within an internal compartment. When reconsidered in this manner, the proteolytic maturation of the HIV-1 particle plays a dominant role in regulating the fusogenicity of the virus particle so that it occurs with a set time delay after synaptic transfer.

The intra-endosomal maturation of virus particles could directly affect the susceptibility of viral membrane fusion to neutralizing antibodies. Although many broadly neutralizing monoclonal antibodies can block VS-promoted viral infection [18, 129], we have shown that polyclonal antibodies from patient sera can only partially block VS-promoted viral fusion (Figure 6.3) and productive infection [16], while maintaining strong inhibitory activity against cell-free virus. This implies that a subset of

antibodies within patient sera block cell-free fusion more efficiently than VS-induced fusion. In further agreement with this notion, recent studies have identified a monoclonal antibody that neutralizes cell-free infection with much greater efficiency than VS-promoted infection (N. Durham and B.K.C., manuscript in preparation). Because Env epitopes exposed on the surface of the cell will be nonfusogenic, they may be less likely to react with antibodies that target epitopes associated with mature, cell-free virions (Figure 6.9). The initial engagement of Env and CD4 occurs during synapse formation, where viral assembly is subsequently recruited to the site. In this early stage, Env is held in a prefusogenic conformation that does not induce cell-cell fusion. It follows that CD4-Env engagement is not the immediate driving force that activates viral membrane fusion during VS-mediated infection; rather, it is more likely that the maturation process occurring within the virus particle triggers particle fusogenicity. Thus, even if antibodies can gain access to the endocytic compartment, the relevant viral epitopes may be hidden, sterically obstructed by the preformed Env/CD4 interaction, or only very transiently exposed when viral membrane fusion is activated by particle maturation. This unique order of events during VS-mediated infection may explain how VSs exhibit distinct sensitivity to patient neutralizing antibodies.

The cellular localization of HIV-1 fusion during infection with cell-free virus remains a subject of intense study. Unlike pH-dependent viruses such as alphaviruses and flaviviruses, HIV-1 undergoes a pH-independent viral membrane fusion [119, 130, 131]. While early literature suggested that the plasma membrane is the primary site of viral fusion, more recent evidence suggests that HIV-1 fusion can occur in an endosomal compartment. A compelling study by Miyauchi et al. used C52L, a late-stage

inhibitor of viral membrane fusion, in combination with a temperature block to demonstrate that a substantial portion of HIV-1 fusion can occur from an intracellular compartment in HeLa and T cell line models of infection [22]. Intriguingly, the majority of the fusion events imaged by Miyauchi et al. were suggested to occur at endocytic locations, not the plasma membrane. These results strongly suggest that endocytic compartments can serve as an efficient intermediate state during viral entry, even with cell-free viral innoculums.

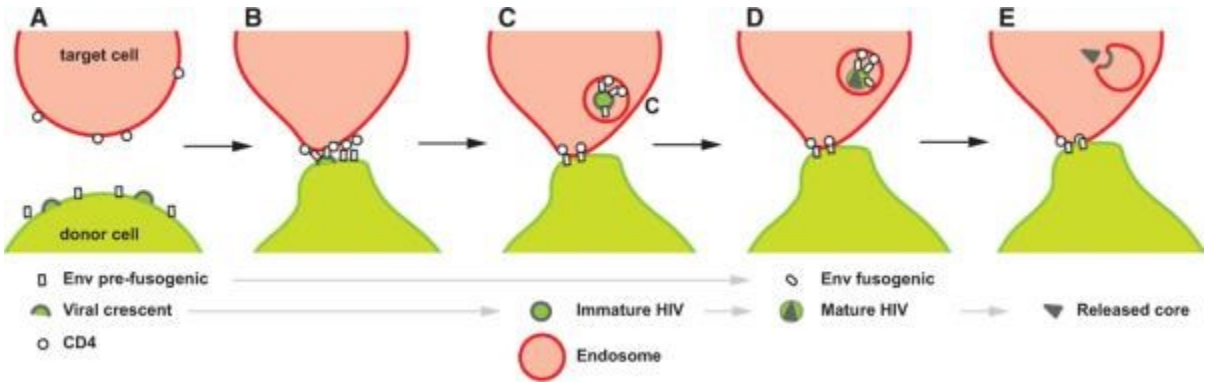

Figure 6.9 Model for maturation-induced fusion at the virological synapse. (A) In the steady state, an HIV-1 infected T cell has a diffuse distribution of Env and Gag. (B) The engagement of Env on the infected donor cell, with CD4 on the target cell, induces an adhesion event and results in the recruitment of Gag, Env, and CD4 to the VS. (C) An endocytic event is triggered resulting in CD4-dependent uptake of immature virus into acceptor cell intracellular compartments. (D) Bound to CD4, virus particles undergo protease-dependent maturation over time. (E) Viral particle maturation triggers viral membrane fusion, releasing the capsid to the cytoplasm.

The localization of HIV-1 fusion following transfer across the VS appears to occur predominantly through an endocytic pathway. We have previously documented the rapid translocation of HIV-1 within the target cell to a location distal to the synaptic button. Given that the time delay for particle fusion is on the order of 2 hours, it is likely that most fusion occurs from endosomes that are physically distant from the synaptic button. Indeed, our single-particle imaging experiments found that four of five single-

particle fusion events occurred at a distant site. Particle maturation and fusion in the target cell endosomes followed similar protease-sensitive kinetics, further suggesting that the viral particles do not fuse predominantly at the synaptic junction. The time delay for particle maturation is consistent with reports that HIV-1 maturation takes place over a period of hours [126, 132]. It is attractive to speculate that endocytic entry may allow the released core to find itself in a position in the cell that favors the subsequent steps of uncoating, reverse transcription, and nuclear import.

Transmission electron micrographs (TEM) of T cell virological synapses have revealed nascent, crescent-shaped viral buds, directly apposed to the target cell membrane without particles found in the synaptic space [16]. Other TEM images of synapses show free virus particles in a space between donor and target cells [12]. It is possible that the latter images depict distinct synaptic structures, which can form between chronically infected cells that have accumulated virions at the cell surface. Using acutely transfected donor cells to form synapses, we found that the vast majority of virus entering cells is immature, suggesting that newly budded virus particles internalized are very rapidly.

The regulation of Env fusogenicity during synapse-mediated infection is critical because it allows the virus to transfer from cell to cell in a conformation immunologically distinct from cell-free virus. It also allows Env to remain in a prefusogenic state during synapse formation. Thus, the virological synapse does not merely provide an adhesive contact to concentrate cell-free virus but also provides a unique method of regulating the exposure of sensitive fusogenic epitopes, revealing them only transiently within a protected, fusion-competent compartment. Because antibodies are likely to target

epitopes on mature cell-free virus, conformational masking of these fusogenic epitopes on the cell-surface may allow cell-surface Env to escape detection by these antibodies. Future vaccine efforts may be designed to specifically target epitopes that block synapse formation at the surface of the infected T cell.

Chapter 7 Cytoskeletal and single virion imaging using structured illumination microscopy

In every stage of the infection cycle, the cytoskeleton plays a critical role [133]. As early as 1994, the cytoskeleton was shown to be important in both HIV-1 viral entry and productive infection [56]. More recently, Jolly, et. al. [15], showed that disruption of actin and tubulin reorganization interfered with localization of HIV-1 at the cell membrane, transfer of the virus at the synapse, and even production of new viral DNA. In an earlier paper [12], the same group showed a dependence on actin to reorganize receptor proteins on target cell membranes in order for productive infection to occur. Similarly, it has been shown that promoting actin activity through spinoculation increases infection, but when actin polymerization is inhibited in the same experiments the increase in infection is reduced [134].

Actin's ability to depolymerize may be just as important to HIV-1 infection as polymerization. The ability of HIV-1 to infect resting cells has been linked to signaling of the actin-depolymerizing protein cofilin, which is activated with HIV-1 binding to CXCR4 [133]. Artificial induction of cofilin signaling, and the accompanying increase in actin depolymerization, actually increases infection [135], while inhibition of cofilin can decrease it [134]. Additionally, local depletion of actin at the center of virological synapses has been linked to T cell receptor signaling from HIV-1 binding [136].

Microtubules play a similarly critical, but different, role in the infection process. Within target cells, HIV-1 viral particles have been imaged moving towards the nucleus at speeds indicating transport along microtubules, a motion that is complemented by actin-inferring motion closer to the plasma membrane and the nucleus [137].

Microtubules also support the formation of new HIV-1 virions in part by transporting Gag and viral RNA to the plasma membrane [138, 139]. In other retroviral systems, microtubule organizing centers (MTOCs) have been seen polarizing towards infectious synapses [14, 51, 136], a behavior which has been observed in a percentage of HIV-1 targeted cells as well [14, 136].

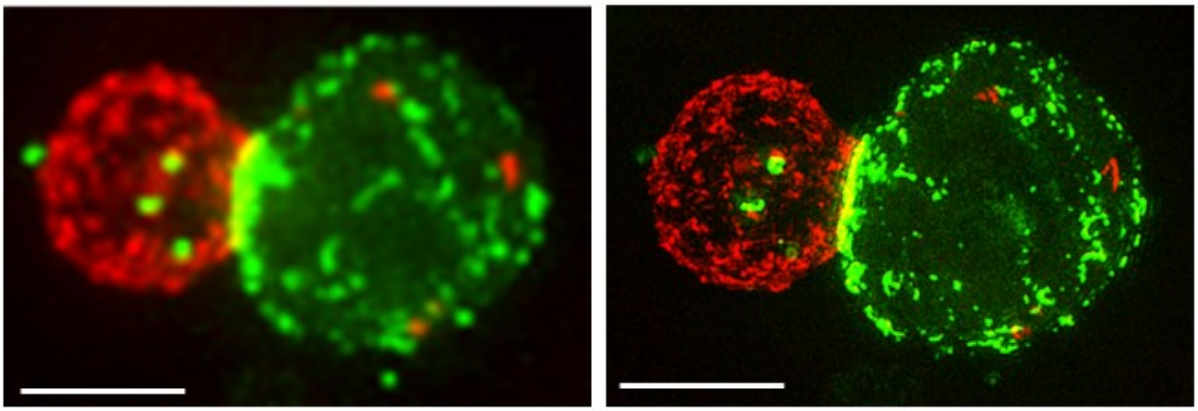

Figure 7.1 SIM improves both resolution and contrast over conventional imaging. A host cell transfers HIV (GFP-Gag, green) to a target cell. Actin structures (red, stained post-fixation) are much more clear in the SIM image (right) than with the conventional technique (left). Images are maximum intensity projections, and the scale bars are 5 μm. Conventional image was taken using 2 x 2 binning on a deconvolution microscope.

Actin and tubulin filaments are very thin, only 8 and 25 nm in diameter, respectively [61]. Neither they nor single HIV virions (~120 nm in diameter) can be individually identified using conventional microscopy, whose resolution is limited to 200-250 nm. Super resolution techniques, discussed in Chapter 3.5, help bridge the gap between the incredible resolution of x-ray- and electron-based microscopies and the highly-specific, physiologically-relevant flexibility of optical microscopy. Structured illumination microscopy (SIM) in particular improves resolution up to a factor of two, enabling single-virus imaging of HIV. Furthermore, it improves contrast over up to 8X over conventional widefield techniques, revealing more of the actin and tubulin network

microstructure within cells. Although the work shown here is all on fixed cells, recent advances in SIM will allow for live imaging of slower-moving samples in the future.

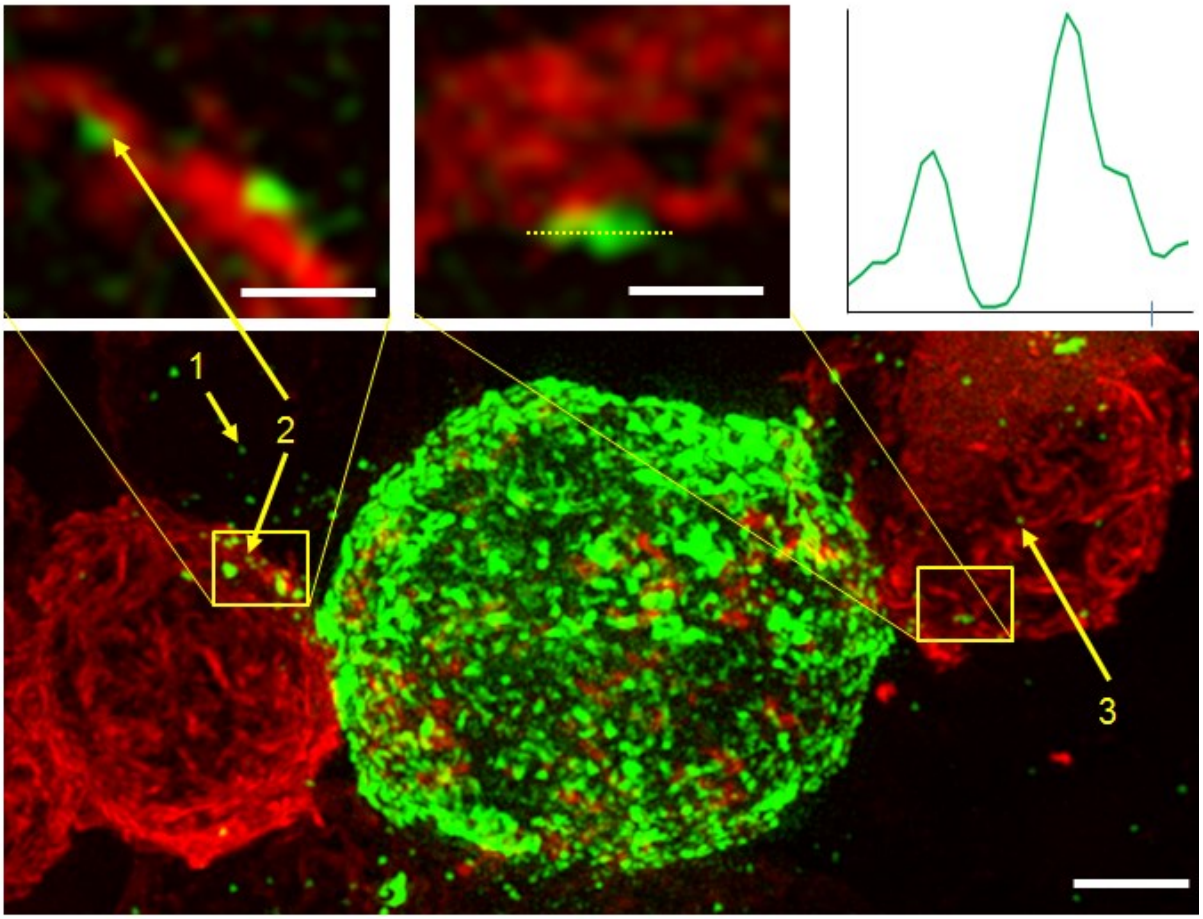

Figure 7.2 Structured illumination can discriminate individual viral particles. A cell transfers HIV (GFP-Gag, green) simultaneously to two target cells. Actin (red) was stained after fixation. Large image is a maximum intensity projection with a 5 μm scale bar. Video 7.1 shows a 3D rendering of this data. Cross sections of Individual particles (arrows 1, 2, 3) were fit to Gaussians and measured to be the approximate size of a known HIV virion (FWHM = 121, 110, 128 nm respectively).Insets are single-plane, magnified views of the boxed areas, with 1 μm scale bars. The plot is an intensity profile of the dashed line in the middle inset, with the distance (hash mark at 1 μm) along the x axis and relative intensity along y.

Data from SIM is both qualitatively and quantitatively better. In Figure 7.1, the qualitative enhancement is clear when comparing a SIM image side-by-side with a conventional-microscopy equivalent. While the virological synapse (VS) and multiple

viral particles are visible in both images, more individual viral particles are visible in the SIM image, as are many more structural details within the actin skeleton. Quantitatively the benefits can be seen when measuring the size or plotting the profile of viral particles. In a conventional image, a full width half max (FWHM) measurement of 250 nm is the minimum possible due to diffraction, and could indicate either a single or multiple virions. Figure 7.2 emphasizes (numbered arrows) three viral particles whose measurements clearly indicate they are individual viral particles, with FWHMs of 121, 110, and 128 nm. The profile of a separate viral cluster (dashed line, plot) clearly shows it is composed of multiple viral particles, which may not have been clear with conventional imaging.

Furthermore, the 3D capabilities of SIM provide critical information. Of the three individual viral particles in Figure 7.2 mentioned above, 3D rendering of the data (see Video 7.1) indicated that the virus was inside the cortical actin, one was outside the cortical actin, and a third was a free virus on the coverslip. 3D also visualization allows connections to be traced through multiple layers of cells. In Figure 7.3 (center) a single bundle of tubulin appears to stretch past several cells to reach its target. Rendering the data in 3D (see Videos 7.2-4) confirms that this thread is not interrupted and is transferring virus through a virological synapse with the distant cell, in addition to potentially maintaining a synapse with a nearby cell. This extension matches well with recent reports of HIV migration in a humanized mouse model, where a subset of infected T cells could stretch to distances of up to 100 μm while maintaining simultaneous virological synapses with multiple cells [140]. The tubulin bundle in Figure 7.3 (center) reaches approximately 30 μm; although this is shorter than many seen in

the mouse model, it is both within the range they observed and 3-4X longer than typical in our system. Furthermore, technical limitations on the field of view (40 μm) and the lack of a supportive tissue structure in our *in vitro* model may preclude the ability to see larger extensions.

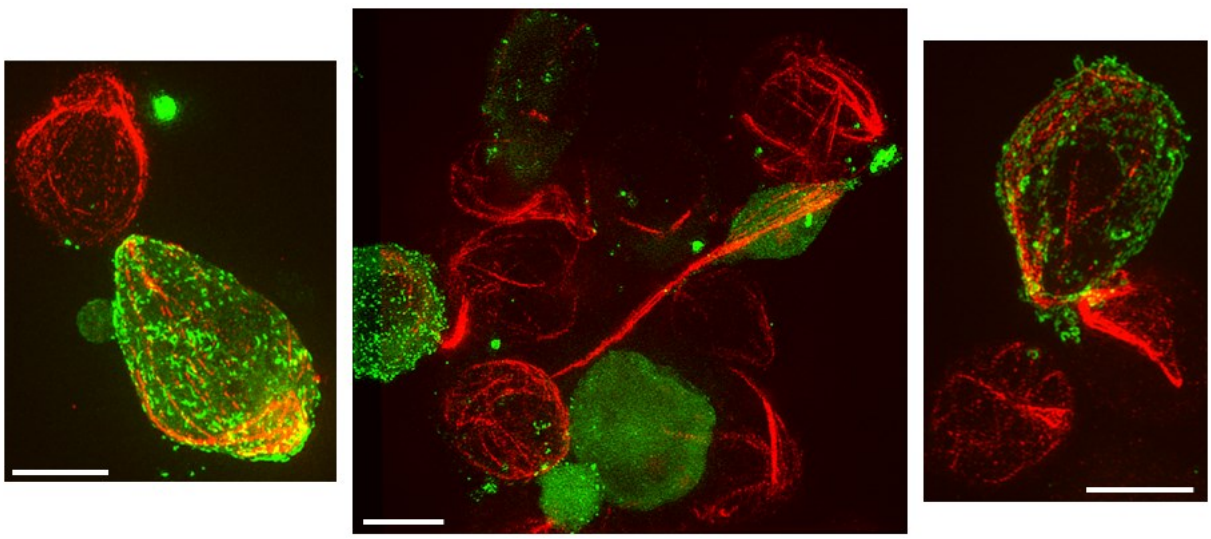

Figure 7.3 Structured illumination shows microtubule orientation during HIV infection. HIV (GFP-Gag, green) transferring to cells is thought to affect polarization of the MTOC (tubulin, red, stained post fixation). In the central image, a cell extends several times its body length to transfer the virus. Videos 7.2-4 rotate the data in 3D to more clearly display the orientation of the tubulin with respect to the synapses. Images are maximum intensity projections and the scale bars are 5 μm.

Although the data shown here neither supports nor contradicts previous studies suggesting polarization of the MTOC, this type of imaging has potential to be a powerful tool to differentiate cytoskeletal behavior at different time points during the infection process. In particular, SIM enables the ability to identify the positions of viral particles as either inside or outside boundaries, quantify the distribution of transferred particles, and clarify the microstructure of synaptic actin. Furthermore, the development of live cell SIM opens the door to a plethora of dynamic, single virion behavior studies, and offers the tantalizing possibility of imaging the essential dynamics of actin during HIV entry.

Chapter 8 Direct observation of multiple 3D shapes of healthy RBCs with and without optically-induced stress

Optical trapping (OT) has been used in a variety of ways to study red blood cells (RBCs). Deformability has been measured both by pulling beads attached to an RBC [103, 141, 142], and by directly trapping the RBC itself [95, 103]. Multiple mechanical properties have been measured, and various measurements using OT have shown promise in diagnosing medical abnormalities such as sickle cell disease or malaria [33, 102, 141]. Studies have shown that small trapping forces do not cause cell death [59, 100], making OT an excellent tool for studying live cells. Historically, however, OT has been combined only with limited imaging capabilities, leaving many of the histologically-based conclusions open for debate.

The classic model for healthy red blood cells is the donut shape, characterized by a thin, bi-concave disk approximately 7-8 μm in diameter [95, 141, 143] (see also Chapter 2.2). This particular shape is typically seen for resting cells, such as those imaged on a coverslip, and is seen as a flat, concave disk on pathologist's blood smears. However, when RBCs are experiencing flow conditions like they would inside a capillary, two new shapes become dominant: the parachute (concave) and the slipper (asymmetric parachute), named for their 2D cross-sectional appearances. Mechanical properties of the RBC, such as membrane elasticity, are linked with cellular age and are thought to affect the adoption of these additional shapes [33, 102]. Optical trapping studies of RBCs, both experimental and theoretical, have typically assumed the donut shape as the dominant form, but the work presented here shows that multiple RBC shapes are valid and need to be considered.

Furthermore, the direct effects of OT have been highly debated. Many studies have suggested that optical traps fold RBCs nearly in half [33, 59, 91, 144], potentially making OTs a useful tool to simulate the squeezing of an RBC through a capillary. Alternatively, it has been argued that cells are not folded within a trap, but rather realigned so that only the thinnest part of the cell is visible in the field of view [32]. Because earlier OT methods used only 2D fluorescence or brightfield imaging, the 3D shape could not be conclusively defined. By combining OT with 3D fluorescence imaging, we are now able to directly image the 3D shape of an optically trapped RBC, and our results below show that the primary effect of OT is to flip, rather than fold RBCs.

In addition to providing a conclusive answer as to whether RBCs flip or fold, our 3D characterization of RBCs is intended to highlight the heterogeneity of native RBC shapes, as well as provide the basis for a new tool in studying RBC abnormalities. Our goals were to observe and report both resting and trapped RBC morphologies in a manner that would not damage the cells, and investigate the effects of and variety of uses of optical tweezers. Our results below include the three main shapes of RBCs, an analysis of labeling methods on the cells, and the effects of optical trapping on RBC shapes.

8.1 Methods for collection, labeling, trapping, and imaging RBCs

All samples were collected fresh each day from the same healthy, adult male. A single drop of blood was deposited directly into either DPBS (Dulbecco's phosphate-buffered saline) or 20mM HEPES (N-2-hydroxyethylpiperazine-N'-2-ethanesulfonic acid) in calcium- and magnesium-free DPBS (-/- DPBS) at room temperature. Samples were diluted and then washed twice in the same media at 200 x g for 5 minutes. All samples

were collected and treated in accordance with University of California Davis Internal Review Board Protocol #233336-4.

Cells were added to a 1:1000 dilution of Cellmask Orange (CMO, Invitrogen) in either Calcium- and Magnesium-positive DPBS (+/+ DPBS) or 20mM HEPES in -/- DPBS, and incubated at room temperature for 10 minutes. The mixture was washed twice at 200 x g for 5 minutes before being used. Alternatively, 1:20 dilutions of CMO were added directly to the sample on the microscope for proof-of-concept testing. For Vybrant® DiI (DiI, Invitrogen) labeling, red blood cells (RBCs) in HEPES were suspended in a 1:200 dilution of DiI in 20mM HEPES for 1 hour at room temperature. The mixture was washed twice at 200 x g for 5 minutes before being used. For fixed RBCs, cell suspensions were mixed with an equal volume of 4% paraformaldehyde and incubated at room temperature for 15 minutes. They were then washed twice at 200 x g for 5 minutes in -/-DPBS.

A single droplet of cells in suspension was placed on a sterilized #1.5 thickness coverslip coated with bovine serum albumin (to prevent sticking). Samples were covered with a petri dish to reduce evaporation of the droplet, and room temperature was maintained throughout. All imaging was performed on the spinning disk confocal system described in Chapter 4. For the CMO and DiI labels, excitation with 568 nm laser light was used and emission was filtered with a 607/36 nm bandpass filter (Semrock). Autofluorescence imaging used the 488 nm laser line and a 695/70 nm bandpass filter (Semrock). Typical trapping power used (measured at the objective) was 15-20 mW, but due to the zero-order spot from the SLM and multiple traps frequently used, each cell was typically only exposed to ~5 mW while trapped.

Images were exported without modification from the Andor iQ software as TIFF files. In both FIJI (open source) and Volocity (Perkin Elmer), brightness and contrast were enhanced without gamma corrections. Single plane images were combined into hyperstacks to show the 3D shape, and images were cropped to the relevant timepoints and single-cell fields of view. XZ and YZ orthogonal views of the 3D image were generated with built-in functions, and 3D renderings used the 3D opacity feature of Volocity viewed under a 'fluorescence' setting. The brightfield video was edited using Windows Movie Maker.

8.2 Red blood cell shapes

In addition to the well-known donut shape [95, 141, 143], a number of other shapes of RBCs were observed while either suspended in optical traps or resting on a coverslip. Unsurprisingly, both spherical and jagged RBCs were seen when the cells were mistreated through the addition of certain dyes or lack of appropriate environmental conditions. Otherwise healthy cells were observed in the shapes of disks, bowls, and seashells (Figure 8.1). The bowl shape was observed approximately three times more frequently than the donut shape.

8.3 Laser trapping effects on red blood cell shape

RBCs imaged while resting on a glass coverslip were observed to typically adopt a round, bowl or donut-shaped profile in the XY (imaging) plane, and an oblong profile in the Z plane (XZ or YZ) (Figure 8.2 A). In 3D, this translates to both bowl and donut shapes. While suspended above the coverslip in an optical trap, cells had an oblong profile in XY but a donut-like profile in one of the Z planes (Figure 8.2 B). The dimensions of the cell in 3D were approximately the same after trapping. The basic

shape of the cell was maintained after optical trapping for both DiI-labeled and autofluorescence-imaged RBCs. Video 8.1 shows the reorientation of cells before, during, and after trapping as viewed two-dimensionally under brightfield illumination.

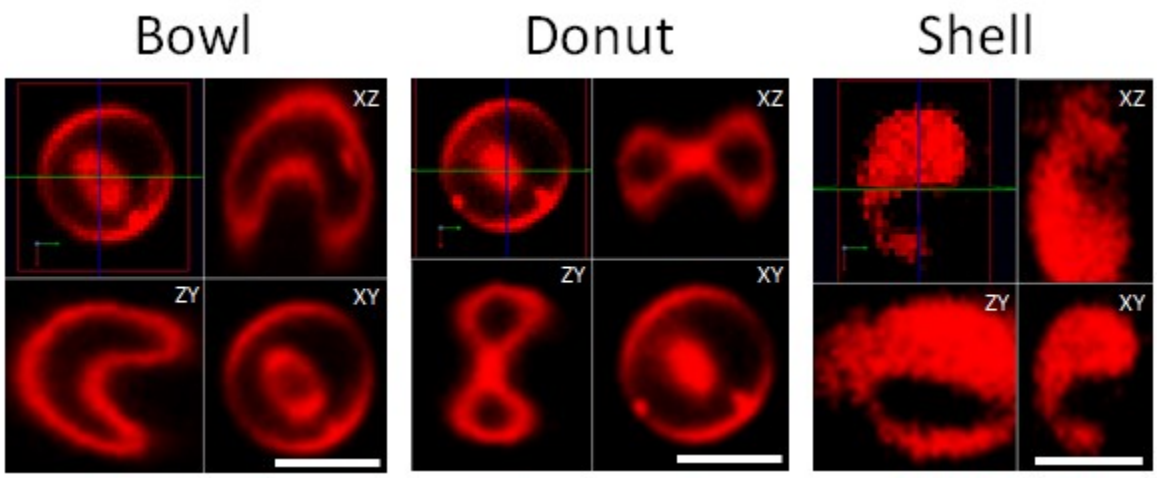

Figure 8.1 Healthy red blood cells are found in three basic shapes. When floating freely or resting on a coverslip, RBCs take on the shape of a bowl (left) or a donut or hubcap (middle). When trapped, they can also take on a third shape, similar to a seashell (right). The figures show orthogonal 2D cross sections of cells; 3D renderings are available as Videos 8.2-4. The bowl-and donut-shaped cells shown here were labeled with DiI, and the shell-shaped cell was imaged using autofluorescence only. Scale bars are 5 μm.

When cells were trapped, either from suspension or pulled off the coverslip they typically held the form of a bowl or donut (Figure 8.1 A, B). In a few cases, the lobes of trapped RBCs developed an asymmetric shape, with one lobe of the donut wider and thicker than the other. In more exaggerated examples, the cell begins to resemble a conch-type seashell (Figure 8.1 C). This effect was not seen for any untrapped cells lying flat on the coverslip. RBCs appeared to reorient and keep the same shape even while the trapping power was increased and decreased through a range of 3 mW to 50 mW, although continued exposure to higher powers did eventually damage the cells. Changing the objective magnification and NA also did not appear to change the effects

on the cells. When 40X, 0.65 NA air and 100X, 1.30 NA oil objectives were substituted for the 60X, 1.42 NA oil objective, no differences were noted.

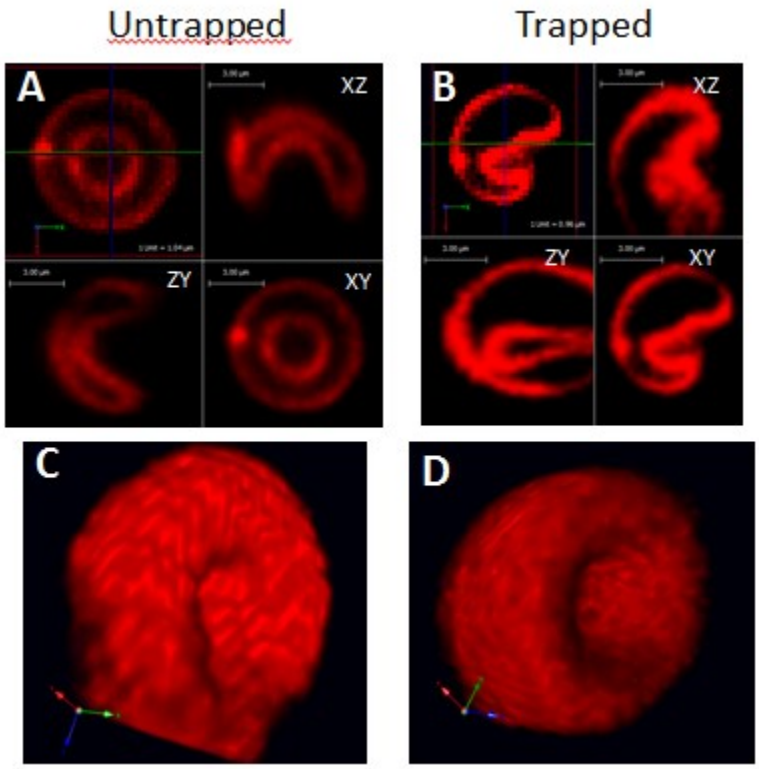

Figure 8.2 A red blood cell maintains its shape even while trapped. A DiI-labeled RBC is imaged in 3D before trapping (A,C) and while trapped (B,D). Although the classical donut shape is not visible in the XY, XZ, and ZY orthogonal views (A,B) of the trapped RBC, 3D renderings of the image data (C,D) rotated around the Y axis show that the cell retains its concave form even while trapped. The cross sections of the trapped cell (B) appear to show a folded cell, but a full 3D view (D) shows the cell to be simply reoriented. Differences in the 3D rendering are from artifacts and lower exposure time due to the wandering of the untrapped cell.

By holding a cell with one laser trap and adding a second trap nearby, we were able to further manipulate the cell. One laser spot acted as a fixed pivot point, and the second laser spot was moved around it to rotate the cell around the pivot while maintaining its shape (Figure 8.3). At the lower laser powers, we were unable to noticeably stretch the cell between the two spots before the cell was pulled away from one of the traps.

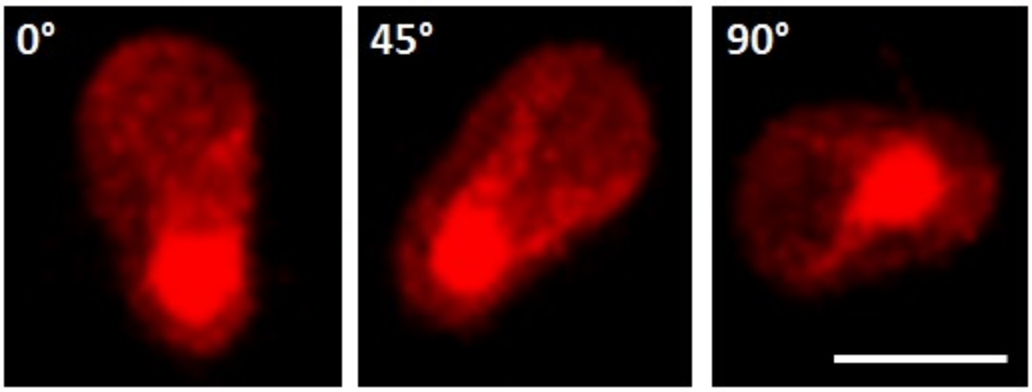

Figure 8.3 A red blood cell is rotated using two traps. One trap holds the cell in place while the second trap is moved radially around the first to rotate the cell. The image shows the same cell at 0°, 45° and 90° (left to right). The cell is labeled with DiI, the scale bar is 5 μm, and the image is a maximum intensity projection of the 3D data. The cause of the bright spot is unknown, but helps visualize relative position.

8.4 Effects of labeling

Our attempts to fluorescently stain the plasma membrane of red blood cells with CMO resulted in damaged RBCs, which swelled up and adopted a spherical and/or jagged shape (Figure 8.4 A, B). This occurred with the typical labeling protocol in both DPBS and HEPES as well as with reduced concentrations and incubation periods. When CMO was added at a low concentration to the sample already under the microscope, the cells quickly took up the dye and could be imaged, but began to swell within 15 minutes.

As a control, unlabeled cells were imaged using autofluorescence and the cell shapes were compared to labeled cells. Swelling, gentle ruffling, and general deformation were also seen with cells that were unlabeled, not centrifuged, and suspended in pure DPBS without HEPES (Figure 8.4 C). For all other experiments, cells were diluted and prepared in 20mM HEPES, which did not cause swelling (Figure 8.4 D). Cells that were labeled with 5 uM DiI in 20 mM HEPES showed no negative effects

from labeling when compared with unlabeled cells. This protocol provided a bright, generally uniform membrane stain that could easily be imaged with our shortest available exposure time (~30 ms) (Figure 8.4 E).

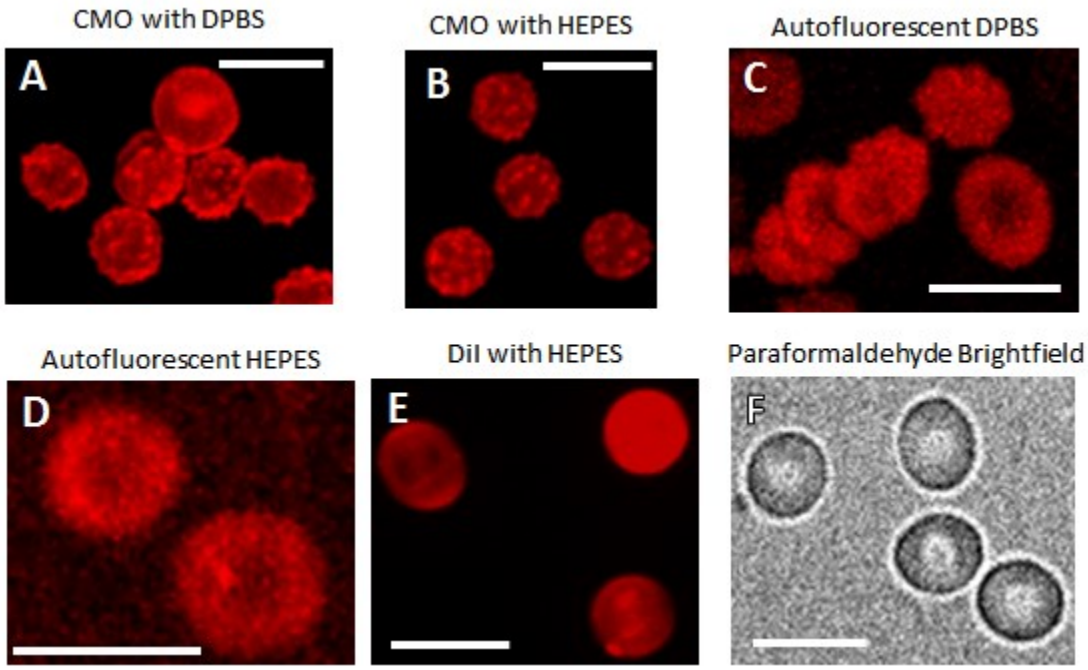

Figure 8.4 Labeling conditions dramatically affect RBC health. RBCs labeled with CellMask Orange (A,B) quickly adopted a spiky shape. The suspension media also affected the health of RBCs; dilution with DPBS alone (C, autofluorescence imaging) caused distortion of the cell shape, whereas dilution with 20mM HEPES in DPBS (D, autofluorescence imaging) maintained cellular integrity. Labeling of RBCs with DiI in HEPES (E) provided a bright and non-damaging method of imaging. Fixation of unlabeled cells produced uniform, bowl-like RBCs (F, brightfield imaging). Images are maximum intensity projections (A-E) or brightfield imaging (F) of cells resting on a glass coverslip, with 10 μm scale bars.

Because many other studies use fixed RBCs for trapping experiments, we also examined the shape of cells fixed in paraformaldehyde. Fixation quenched the autofluorescence, so only 2D brightfield images could be captured. The fixed RBCs appear to uniformly adopt a bowl shape while on the coverslip (Figure 8.4 F), but the true shape cannot be confirmed without 3D data.

8.5 Simultaneous laser trapping and 3D imaging reveal previously hidden effects of trapping

We found that many previous studies of red blood cells [33, 59, 91, 144] falsely observed red blood cells 'folding' due to the two-dimensional imaging techniques. In fact, our initial data including of partial 3D scans of RBCs appeared to show this folding phenomenon when viewed as 2D cross-sections, as did our brightfield images (Figure 8.5). Because the orthogonal axis of RBCs is significantly smaller than the round profile typically seen when imaging, if the cell flipping is not considered it may appear as if the cell has folded in half. Video 8.1 shows this ambiguity when trapping is viewed in two dimensions under brightfield. It was not until the data was visualized in 3D, with three orthogonal cross-sections and a rotatable 3D rendering, that we observed the cell shape to remain largely unchanged. Figure 8.4 A and B includes cross sections of an optically trapped cell compared to the same cell without the trap, showing what appears to be folding during trapping. However, Figure 8.4 4C and D shows 3D renderings of the same cell rotated in 3D space using software, after which the cell appears identical in shape whether trapped or untrapped. Cell flipping, rather than folding, was also observed using autofluorescence of unlabeled cells.

This method of analysis was previously unavailable because there have been no prior reports of microscopes capable of simultaneous trapping and 3D imaging. While 3D manipulation has been reported in combination with 3D fluorescence imaging [93], the trapped objects needed to be released prior to changing the imaging plane. This new technique will enable deeper study of the effects of trapping, including those whose durations are shorter than the time required to image a full 3D stack.

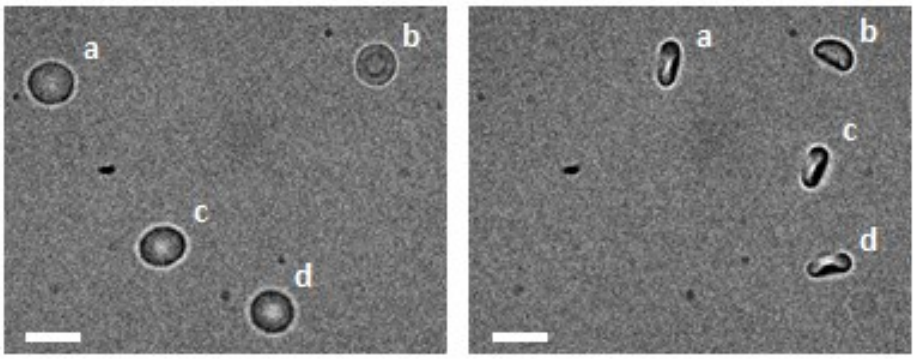

Figure 8.5 Flipping of RBCs appears to be folding when viewed only in two dimensions. DiI-labeled RBCs were imaged under brightfield before (left) and after (right) they were optically trapped and moved. Because only the narrow edge of the RBC disk is visible, without the 3D data the cells may incorrectly be assumed to have folded. Each cell is lettered to identify it before and after trapping. Scale is 10 μm.

8.6 Implications of multiple RBC shapes

Although the primary effect of optical trapping was to reorient cells, a subset of them also showed shape deformation, changing from a donut shape to a shell shape with unevenly-sized lobes. The nature of the optical setup makes images slightly prone to size distortions along the Z axis, but the orientation of these cells in 3D space rules out this artifact as the cause of the lobe distortion. Differences in cell shape appear during trapping despite all samples being gathered from the same healthy donor and treated using the same protocol. Experimental conditions, such as time between sample collection and imaging or length of time within a trap, may explain some of the variation. However, subpopulation features such as cell age and membrane composition are factors in cell deformability and thus likely impact trapped cell shape [33, 103]. Subpopulation features are also apparent through uneven cell staining with DiI (Figure 8.3), and the staining itself may also impact the trapped shape. Additionally, the direct object of trapping, whether it is the membrane of the cell, the inner contents, or a

combination of both, is still unknown. Depending on the mechanism, the influence of these specific RBC properties on trapped cell shape will be more or less pronounced.

When non-donut RBC shapes have been reported previously, they have been subjected to flow conditions [33, 102] such as those experienced by the cells within a capillary. Our cells were suspended in a droplet on a coverslip, and were not expected to be experiencing significant flow forces. Although not anticipated, it is possible the cells were in the path of currents caused by the shrinking of the droplet (although evaporation was minimized by keeping the sample covered) or potentially by currents generated by the optical traps as objects were pulled in. Neither explanation accounts for the large proportion of bowl-shaped cells found including on the coverslip. Furthermore, the concavity of the bowls was typically orthogonal to the coverslip, which precludes arguments that they are distorted by a flow in a direction parallel to the concavity.

8.7 Future directions for studying RBCs in optical traps

Although flow conditions cannot explain all of our results, they have been useful in detecting changes in RBC properties [33] and should be further investigated. A flow environment could be induced by dragging the cell at a specific velocity relative to a stable environment as shown by Mohanty, et. al [145] or by combining our current setup with a microfluidic chamber to generate actual flow conditions. Furthermore, future studies could attempt to block possible flow conditions by setting up a barrier wall of trapped objects surrounding the cell of interest.

Additional equipment modifications would be useful for other measurements. Delays between the imaging and trapping plane movements, which cause a slight

jerking motion while imaging, could be reduced or negated by combining all software into one system and pre-calculating the hologram patterns prior to imaging. Additionally, due to two separate laser paths for imaging and trapping, as well as refraction from the cells, there was a skew between the imaging and trapping planes that required manual correction and introduced an unknown scaling factor in the z-step size. Quantitative measurements would be much more reliable if this was resolved through the use of second objective, or through system characterization with automated correction, although diffraction through irregularly shaped RBCs might not allow for full correction of this issue.

While the data presented here was collected over several weeks with samples collected fresh each day, all of the samples were taken from a single healthy donor. Future research should involve a greater sample size both within the same demographic group (healthy, Caucasian, adult men) and from more diverse groups. Samples were prepared from untreated blood, but for clinical relevance these experiments should be repeated with samples from standard EDTA (ethylenediaminetetraacetic acid)-treated collection tubes. Alternative sample treatments could be tested, including dilution of samples in plasma or fetal bovine serum.

We have presented a new tool useful for characterizing the 3D shape of trapped cells. If optical trapping does indeed highlight differences within subpopulations of RBCs, analysis of 3D shape has potential as a diagnostic tool both for identifying disease and monitoring treatment; quantitative measurements could include the ratio of cellular lobe thickness to measure asymmetry in deformation, differences in minimum

thickness at the donut hole prior to and during trapping, or changes in eccentricity of the donut shape, both in steady state and in flow conditions. Disorders affecting iron content, for example, may impact the relative strength of the force felt by the inner contents of the cells, and thus change the amount of cellular deformation. Sickle cells might adopt yet another 3D shape within a trap. Alternatively, controlling subpopulation features by using disease factors could help identify the mechanism of trapping deformation, thus allowing for the development of an even more powerful diagnostic tool.

Chapter 9 Summary and outlook

In this dissertation I demonstrate how combining optical technologies can unlock previously hidden information about cellular characteristics and interactions. In Chapter 4, I describe the development and testing of a novel microscope that can optically trap and manipulate multiple cells while simultaneously imaging in 3D. By using feedback-driven holographic optical tweezers (HOT) combined with a high speed, high resolution, multichannel spinning disk confocal microscope (SDCM), we can now directly measure the effect of optical trapping on single cells. The first of many future breakthroughs using this system is described in Chapter 8, where we show that two common assumptions regarding red blood cell (RBC) morphology are either invalid or incomplete. By imaging both trapped and untrapped RBCs in 3D, we demonstrated that optical trapping does not fold RBCs in half but instead realigns them in the direction of the trapping laser. Additionally, we showed that the dominant morphology of a healthy, resting RBC was a bowl shape, rather than the presumed 'donut' shape. This new data and technique for studying RBCs can be used to develop better models for computational studies of RBC deformation, and to investigate a variety of RBC-related diseases, such as malaria or anemia.

The 3D trap microscope can enhance a plethora of biological research areas, and in fact was inspired by the HIV work in this dissertation. In Chapter 6, we use multicolor SDCM and flow cytometry to reveal a new pathway to productive HIV infection. Our data shows that viral entry through the virological synapse occurs through endocytosis of immature virions, followed by viral maturation and fusion with the endosomal membrane. The data used to prove this pathway required imaging individual

virological synapses for up to 2 hours each, with many more non-events captured for each productive experiment. Each cell pair imaged required up to two hours of imaging, with many instances of non-events for every active synapse captured. By using the combined HOT-SDCM, future experiments can increase the incidence of cell-to-cell contact to increase both the number of events captured within a field of view and the likelihood of synapse formation, such as was partially demonstrated with a single-trap, non-concurrent imaging system [94]. Alternatively, optical traps can be used to preferentially select a subpopulation of cells, such as those with polarized concentrations of cell-surface receptors, and to induce contact between receptor-enriched surfaces to study the impact of specific proteins on synapse formation.

In Chapter 7 we show that structured illumination microscopy (SIM) is yet another powerful tool that can be used to dissect the inter- and intracellular interactions of HIV. SIM improves resolution over the diffraction limit by a factor of two, allowing us to image and identify individual virions, while maintaining cellular context with multicolor, 3D imaging. The data presented in Chapter 7 highlight the variability in synapse-mediated HIV entry, with oppositely polarized acceptor cells and donor cells that infect both nearby and distant target cells, and provide a basis for further study of cytoskeletal involvement.

Major problems such as HIV cannot be solved with a single approach; even viral entry itself takes a multi-pathway approach. HIV spread can be slowed through education with or without the development of a vaccine, and neither approach should preclude the search for a cure. Research on RBC-related disease has benefitted from advances in understanding individual components such as hemoglobin, and from

whole-cell studies on morphology or deformation. Rather than single-minded focus, the best gains come from combining dissimilar methods to select for the highest advantages (resolution of SIM, speed of spinning disk microscopy, or control from optical trapping) while reducing the drawbacks (low speed, resolution, or control). This principle can naturally be expanded beyond simple instrumentation and methodology, and should be used to further encourage interactions between disciplines; indeed, the joining of biology with physics has been a demonstrably successful combination.

References

1. Hubner, W., et al., Sequence of Human Immunodeficiency Virus Type 1 (HIV-1) Gag Localization and Oligomerization Monitored with Live Confocal Imaging of a Replication-Competent, Fluorescently Tagged HIV-1. J. Virol., 2007. 81(22): p. 12596-12607.
2. Ganser-Pornillos, B.K., M. Yeager, and W.I. Sundquist, The structural biology of HIV assembly. Current Opinion in Structural Biology, 2008. 18(2): p. 203-217.
3. Dale, B.M., et al., Cell-to-cell transfer of HIV-1 via virological synapses leads to endosomal virion maturation that activates viral membrane fusion. Cell Host Microbe, 2011. 10(6): p. 551-62.
4. Davenport, D. and J.A.C. Nicol, Luminescence in Hydromedusae. Proceedings of the Royal Society of London. Series B - Biological Sciences, 1955. **144**(916): p. 399-411.
5. Lasers: Invention to Application, ed. J.R. Whinnery, J.H. Ausubel, and H.D. Langford. 1987: The National Academies Press.
6. Kim, M.J., et al., Generation of transgenic dogs that conditionally express green fluorescent protein. genesis, 2011. **49**(6): p. 472-478.
7. Brook, I., Approval of zidovudine (azt) for acquired immunodeficiency syndrome: A challenge to the medical and pharmaceutical communities. JAMA, 1987. **258**(11): p. 1517-1517.
8. Rerks-Ngarm, S., et al., Vaccination with ALVAC and AIDSVAX to Prevent HIV-1 Infection in Thailand. New England Journal of Medicine, 2009. **361**(23): p. 2209-2220.
9. Sato, H., et al., Cell-to-cell spread of HIV-1 occurs within minutes and may not involve the participation of virus particles. Virology, 1992. **186**(2): p. 712-724.
10. Blumenthal, R., S. Durell, and M. Viard, HIV Entry and Envelope Glycoprotein-mediated Fusion. Journal of Biological Chemistry, 2012. **287**(49): p. 40841-40849.
11. McDonald, D., et al., Recruitment of HIV and Its Receptors to Dendritic Cell-T Cell Junctions. Science, 2003. **300**(5623): p. 1295-1297.
12. Jolly, C., et al., HIV-1 Cell to Cell Transfer across an Env-induced, Actin-dependent Synapse. J. Exp. Med., 2004. **199**(2): p. 283-293.
13. Jolly, C. and Q. Sattentau, Retroviral spread by induction of virological synapses. Traffic, 2004. **5**(9): p. 643-650.
14. Piguet, V. and Q. Sattentau, Dangerous liaisons at the virological synapse. Journal of Clinical Investigation, 2004. **114**(5): p. 605-610.
15. Jolly, C., I. Mitar, and Q.J. Sattentau, Requirement for an Intact T-Cell Actin and Tubulin Cytoskeleton for Efficient Assembly and Spread of Human Immunodeficiency Virus Type 1. J. Virol., 2007. **81**(11): p. 5547-5560.
16. Hubner, W., et al., Quantitative 3D video microscopy of HIV transfer across T cell virological synapses. Science, 2009. **323**(5922): p. 1743-7.
17. Martin, N. and Q. Sattentau, Cell-to-cell HIV-1 spread and its implications for immune evasion. Current Opinion in HIV and AIDS, 2009. **4**(2): p. 143.
18. Chen, P., et al., Predominant Mode of Human Immunodeficiency Virus Transfer between T Cells Is Mediated by Sustained Env-Dependent Neutralization-

Resistant Virological Synapses. Journal of Virology, 2007. **81**(22): p. 12582-12595.
19. Uchil, P.D. and W. Mothes, HIV Entry Revisited. Cell, 2009. **137**(3): p. 402-404.
20. Levy, J.A., HIV and the Pathogenesis of AIDS. 2007: ASM Press Washington, DC.
21. Permanyer, M., E. Ballana, and J.A. Esté, Endocytosis of HIV: anything goes. Trends in Microbiology, 2010. **18**(12): p. 543-551.
22. Miyauchi, K., et al., HIV enters cells via endocytosis and dynamin-dependent fusion with endosomes. Cell, 2009. **137**(3): p. 433-444.
23. Miyauchi, K., M. Kozlov, and G. Melikyan, Early Steps of HIV-1 Fusion Define the Sensitivity to Inhibitory Peptides That Block 6-Helix Bundle Formation. PLoS Pathogens, 2009. **5**(9): p. 12.
24. Bosch, B., et al., A clathrin-dynamin-dependent endocytic pathway for the uptake of HIV-1 by direct T cell-T cell transmission. Antiviral Research, 2008. **80**(2): p. 185-193.
25. Chen, B., T cell virological synapses and HIV-1 pathogenesis. Immunologic Research, 2012. **54**(1-3): p. 133-139.
26. Lacroix, J., et al., The Age of Blood Evaluation (ABLE) randomized controlled trial: study design. Transfusion medicine reviews, 2011. **25**(3): p. 197-205.
27. Glynn, S.A., The red blood cell storage lesion: a method to the madness. Transfusion, 2010. **50**(6): p. 1164-1169.
28. Schmaier, A.H. and H.M. Lazarus, Concise guide to hematology. 2011: Wiley-Blackwell.
29. Cluitmans, J.C., et al., Red blood cell deformability during storage: towards functional proteomics and metabolomics in the Blood Bank. Blood Transfusion, 2012. **10**(Suppl 2): p. s12.
30. Steiner, M.E., et al., Addressing the question of the effect of RBC storage on clinical outcomes: The Red Cell Storage Duration Study (RECESS) (Section 7). Transfusion and Apheresis Science, 2010. **43**(1): p. 107-116.
31. Sanders, J., et al., Red blood cell storage is associated with length of stay and renal complications after cardiac surgery. Transfusion, 2011. **51**(11): p. 2286-2294.
32. Gu, M., S. Kuriakose, and X.S. Gan, A single beam near-field laser trap for optical stretching, folding and rotation of erythrocytes. Optics Express, 2007. **15**(3): p. 1369-1375.
33. Basu, H., et al., Tank Treading of Optically Trapped Red Blood Cells in Shear Flow. Biophysical Journal, 2011. **101**(7): p. 1604-1612.
34. Dao, M., C.T. Lim, and S. Suresh, Mechanics of the human red blood cell deformed by optical tweezers Journal of the Mechanics and Physics of Solids, 2003. **53**(2): p. 493-494.
35. Suresh, S., Mechanical response of human red blood cells in health and disease: Some structure-property-function relationships. Journal of Materials Research, 2006. **21**(8): p. 1871-1877.
36. Global report: UNAIDS report on the global AIDS epidemic 2012. 2012.
37. Liao, H.-X., et al., Vaccine Induction of Antibodies against a Structurally Heterogeneous Site of Immune Pressure within HIV-1 Envelope Protein Variable Regions 1 and 2. Immunity, 2013. **38**(1): p. 176-186.

38. Sankaran, S., et al., Rapid onset of intestinal epithelial barrier dysfunction in primary human immunodeficiency virus infection is driven by an imbalance between immune response and mucosal repair and regeneration. Journal of virology, 2008. **82**(1): p. 538-545.
39. Levy, J.A., HIV Pathogenesis: Knowledge Gained after Two Decades of Research. Advances in Dental Research, 2006. **19**(1): p. 10-16.
40. Macal, M., et al., Effective CD4+ T-cell restoration in gut-associated lymphoid tissue of HIV-infected patients is associated with enhanced Th17 cells and polyfunctional HIV-specific T-cell responses. Mucosal immunology, 2008. **1**(6): p. 475-488.
41. Guadalupe, M., et al., Severe CD4+ T-cell depletion in gut lymphoid tissue during primary human immunodeficiency virus type 1 infection and substantial delay in restoration following highly active antiretroviral therapy. Journal of virology, 2003. **77**(21): p. 11708-11717.
42. Brenchley, J.M., D.A. Price, and D.C. Douek, HIV disease: fallout from a mucosal catastrophe? Nature immunology, 2006. **7**(3): p. 235-239.
43. Structure of HIV. HIV/AIDS 2009 April 1, 2009 [cited 2009 December 9, 2009]; Available from: http://www3.niaid.nih.gov/topics/HIVAIDS/Understanding/Biology/structure.htm.
44. Gomez, C. and T.J. Hope, The ins and outs of HIV replication. Cellular Microbiology, 2005. **7**(5): p. 621-626.
45. Ryser, H.J.P. and R. Flückiger, Keynote review: Progress in targeting HIV-1 entry. Drug Discovery Today, 2005. **10**(16): p. 1085-1094.
46. Cullen, B.R., Journey to the Center of the Cell. Cell, 2001. **105**(6): p. 697-700.
47. Ogg, G.S., et al., Quantitation of HIV-1-Specific Cytotoxic T Lymphocytes and Plasma Load of Viral RNA. Science, 1998. **279**(5359): p. 2103-2106.
48. Quinn, T.C., et al., Viral Load and Heterosexual Transmission of Human Immunodeficiency Virus Type 1. N Engl J Med, 2000. **342**(13): p. 921-929.
49. Dimitrov, D., et al., Quantitation of human immunodeficiency virus type 1 infection kinetics. Journal of Virology, 1993. **67**(4): p. 2182.
50. Chen, P., et al., Predominant Mode of Human Immunodeficiency Virus Transfer between T Cells Is Mediated by Sustained Env-Dependent Neutralization-Resistant Virological Synapses. J. Virol., 2007. **81**(22): p. 12582-12595.
51. Rudnicka, D., et al., Simultaneous Cell-to-Cell Transmission of Human Immunodeficiency Virus to Multiple Targets through Polysynapses. J. Virol., 2009. **83**(12): p. 6234-6246.
52. Cameron, P.U., et al., Dendritic cells exposed to human immunodeficiency virus type-1 transmit a vigorous cytopathic infection to CD4+ T cells. Science (New York, NY), 1992. **257**(5068): p. 383.
53. Sato, H., et al., Cell-to-cell spread of HIV-1 occurs within minutes and may not involve the participation of virus particles. Virology, 1992. **186**(2): p. 712.
54. Sowinski, S., et al., Membrane nanotubes physically connect T cells over long distances presenting a novel route for HIV-1 transmission. Nature Cell Biology, 2008. **10**(2): p. 211-219.
55. Hubner, W., et al., Quantitative 3D Video Microscopy of HIV Transfer Across T Cell Virological Synapses. Science, 2009. **323**(5922): p. 1743-1747.

56. Pearce-Pratt, R., D. Malamud, and D.M. Phillips, Role of the cytoskeleton in cell-to-cell transmission of human immunodeficiency virus. J. Virol., 1994. **68**(5): p. 2898-2905.
57. Janas, A., et al., Productive infection of human immunodeficiency virus type 1 in dendritic cells requires fusion-mediated viral entry. Virology, 2008. **375**(2): p. 442-451.
58. Ruggiero, E., et al., Virological Consequences of Early Events Following the Cell-Cell Contact between HIV-1 Infected and Uninfected CD4+ Cells. J. Virol., 2008: p. JVI.00695-08.
59. A. Ghosh, S.S., J. A. Dharmadhikari, S. Roy, A. K. Dharmadhikari, J. Samuel, S. Sharma, D. Mathur, Euler buckling-induced folding and rotation of red blood cells in an optical trap. Physical Biology, 2006. **3**: p. 67-73.
60. Garrett, G.H. and C.M. Grisham, Biochemistry. 3rd ed. 2005: Thomson Brooks/Cole.
61. Karp, G., Cell and Molecular Biology. 4th ed. 2005: John Wiley & Sons.
62. Lim H. W., G., M. Wortis, and R. Mukhopadhyay, Stomatocyte–discocyte–echinocyte sequence of the human red blood cell: Evidence for the bilayer– couple hypothesis from membrane mechanics. Proceedings of the National Academy of Sciences, 2002. **99**(26): p. 16766-16769.
63. Lakowicz, J.R., Principles of fluorescence spectroscopy. Vol. 1. 2006: Springer.
64. Prasad, P.N., Bioimaging: Principles and Techniques, in Introduction to Biophotonics. 2004, John Wiley & Sons, Inc. p. 203-254.
65. Sauer, M., J. Hofkens, and J. Enderlein, Super-Resolution Fluorescence Imaging, in Handbook of Fluorescence Spectroscopy and Imaging. 2011, Wiley-VCH Verlag GmbH & Co. KGaA. p. 219-240.
66. Schermelleh, L., R. Heintzmann, and H. Leonhardt, A guide to super-resolution fluorescence microscopy. The Journal of Cell Biology, 2010. **190**(2): p. 165-175.
67. Tkaczyk, T.S., Field guide to microscopy. Vol. 13. 2010: Society of Photo Optical.
68. Inoué, S., Foundations of Confocal Scanned Imaging in Light Microscopy, in Handbook Of Biological Confocal Microscopy, J.B. Pawley, Editor. 2006, Springer US. p. 1-19.
69. Prasad, P.N., Basics of Biology, in Introduction to Biophotonics. 2004, John Wiley & Sons, Inc. p. 50-91.
70. Oda, T., et al., Effect of the length and effective diameter of F-actin on the filament orientation in liquid crystalline sols measured by x-ray fiber diffraction. Biophysical Journal, 1998. **75**(6): p. 2672-2681.
71. Gustafsson, M.G.L., Extended resolution fluorescence microscopy. Current Opinion in Structural Biology, 1999. **9**(5): p. 627-628.
72. Heintzmann, R. and G. Ficz, Breaking the resolution limit in light microscopy. Briefings in Functional Genomics & Proteomics, 2006. **5**(4): p. 289-301.
73. Gustafsson, M., Surpassing the lateral resolution limit by a factor of two using structured illumination microscopy. Journal of Microscopy, 2000. **198**(2): p. 82-87.
74. Gustafsson, M.G.L., Nonlinear structured-illumination microscopy: Wide-field fluorescence imaging with theoretically unlimited resolution. Proceedings of the National Academy of Sciences of the United States of America, 2005. **102**(37): p. 13081-13086.

75. Gustafsson, M.G.L., et al., Three-Dimensional Resolution Doubling in Wide-Field Fluorescence Microscopy by Structured Illumination. Biophysical Journal, 2008. **94**(12): p. 4957-4970.
76. Bates, M., B. Huang, and X. Zhuang, Super-resolution microscopy by nanoscale localization of photo-switchable fluorescent probes. Current Opinion in Chemical Biology, 2008. **12**(5): p. 505-514.
77. Betzig, E., et al., Imaging Intracellular Fluorescent Proteins at Nanometer Resolution. Science, 2006. **313**(5793): p. 1642-1645.
78. Rust, M.J., M. Bates, and X. Zhuang, Sub-diffraction-limit imaging by stochastic optical reconstruction microscopy (STORM). Nature Methods, 2006. **3**(10): p. 4.
79. Huang, B., et al., Three-Dimensional Super-Resolution Imaging by Stochastic Optical Reconstruction Microscopy. Science, 2008. **319**(5864): p. 810-813.
80. Pavani, S.R.P., et al., Three-dimensional, single-molecule fluorescence imaging beyond the diffraction limit by using a double-helix point spread function. Proceedings of the National Academy of Sciences, 2009. **106**(9): p. 2995-2999.
81. Bock, H., et al., Two-color far-field fluorescence nanoscopy based on photoswitchable emitters. Applied Physics B, 2007. **88**(2): p. 161-165.
82. Bates, M., et al., Multicolor Super-Resolution Imaging with Photo-Switchable Fluorescent Probes. Science, 2007. **317**(5845): p. 1749-1753.
83. Hell, S.W., Far-Field Optical Nanoscopy. Science, 2007. **316**(5828): p. 1153-1158.
84. Hein, B., K.I. Willig, and S.W. Hell, Stimulated emission depletion (STED) nanoscopy of a fluorescent protein-labeled organelle inside a living cell. Proceedings of the National Academy of Sciences, 2008. **105**(38): p. 14271-14276.
85. Bückers, J., et al., Simultaneous multi-lifetime multi-color STED imaging for colocalization analyses. Opt. Express, 2011. **19**(4): p. 3130-3143.
86. Ashkin, A., Acceleration and Trapping of Particles by Radiation Pressure. Physical Review Letters, 1970. **24**(4): p. 156-159.
87. Ashkin, A., et al., OBSERVATION OF A SINGLE-BEAM GRADIENT FORCE OPTICAL TRAP FOR DIELECTRIC PARTICLES. Optics Letters, 1986. **11**(5): p. 288-290.
88. Block, S.M., MAKING LIGHT WORK WITH OPTICAL TWEEZERS. Nature, 1992. **360**(6403): p. 493-495.
89. Ashkin, A., History of optical trapping and manipulation of small-neutral particle, atoms, and molecules. Selected Topics in Quantum Electronics, IEEE Journal of, 2000. **6**(6): p. 841-856.
90. Ashkin, A. and J.M. Dziedzic, Optical trapping and manipulation of viruses and bacteria. Science, 1987. **235**(4795): p. 1517-1520.
91. Dharmadhikari, J.A. and D. Mathur, An optical trap to fold and align single red blood cells. Current Science, 2004. **86**(10): p. 1432-1437.
92. Tam, J.M., et al., Control and Manipulation of Pathogens with an Optical Trap for Live Cell Imaging of Intercellular Interactions. PLoS ONE, 2010. **5**(12): p. e15215.
93. Tam, J.M., et al., Use of an Optical Trap for Study of Host-Pathogen Interactions for Dynamic Live Cell Imaging. J Vis Exp, 2011(53): p. e3123.

94. McNerney, G.P., et al., Manipulating CD4+ T cells by optical tweezers for the initiation of cell-cell transfer of HIV-1. Journal of Biophotonics, 2010. **3**(4): p. 216-223.
95. Bronkhorst, P.J.H., et al., A new method to study shape recovery of red blood cells using multiple optical trapping. Biophysical Journal, 1995. **69**(5): p. 1666-1673.
96. Grier, D.G., A revolution in optical manipulation. Nature, 2003. **424**(6950): p. 810-816.
97. Dufresne, E.R., et al., Computer-generated holographic optical tweezer arrays. Review of Scientific Instruments, 2001. **72**(3): p. 1810-1816.
98. Mazurov, D., et al., Quantitative Comparison of HTLV-1 and HIV-1 Cell-to-Cell Infection with New Replication Dependent Vectors. PLoS Pathogens, 2010. **6**(2).
99. Zhang, H. and K.-K. Liu, Optical tweezers for single cells. Journal of The Royal Society Interface, 2008. **5**(24): p. 671-690.
100. Ashkin, A., J.M. Dziedzic, and T. Yamane, Optical trapping and manipulation of single cells using infrared laser beams. Nature, 1987. **330**(6150): p. 769-771.
101. Oddos, S., et al., High-Speed High-Resolution Imaging of Intercellular Immune Synapses Using Optical Tweezers. Biophysical Journal, 2008. **95**(10): p. L66-L68.
102. Kaoui, B., G. Biros, and C. Misbah, Why Do Red Blood Cells Have Asymmetric Shapes Even in a Symmetric Flow? Physical Review Letters, 2009. **103**(18): p. 188101.
103. Fontes, A., et al., Mechanical and electrical properties of red blood cells using optical tweezers. Journal of Optics, 2011. **13**(4).
104. Dale, B., et al., Visualizing Cell-to-cell Transfer of HIV using Fluorescent Clones of HIV and Live Confocal Microscopy. J Vis Exp, 2010(44): p. e2061.
105. Blanco, J., et al., High level of coreceptor-independent HIV transfer induced by contacts between primary CD4 T cells. Journal of Biological Chemistry, 2004. **279**(49): p. 51305-51314.
106. Sourisseau, M., et al., Inefficient human immunodeficiency virus replication in mobile lymphocytes. Journal of virology, 2007. **81**(2): p. 1000-1012.
107. Hubner, W., et al., Sequence of human immunodeficiency virus type 1 (HIV-1) Gag localization and oligomerization monitored with live confocal imaging of a replication-competent, fluorescently tagged HIV-1. J Virol, 2007. **81**(22): p. 12596-607.
108. Loeb, D.D., et al., Complete mutagenesis of the HIV-1 protease. Nature, 1989. **340**(6232): p. 397-400.
109. Pear, W.S., et al., Production of high-titer helper-free retroviruses by transient transfection. Proc Natl Acad Sci U S A, 1993. **90**(18): p. 8392-6.
110. Markosyan, R.M., F.S. Cohen, and G.B. Melikyan, Time-resolved imaging of HIV-1 Env-mediated lipid and content mixing between a single virion and cell membrane. Mol Biol Cell, 2005. **16**(12): p. 5502-13.
111. Cavrois, M., C. De Noronha, and W.C. Greene, A sensitive and specific enzyme-based assay detecting HIV-1 virion fusion in primary T lymphocytes. Nature biotechnology, 2002. **20**(11): p. 1151-1154.
112. Ono, A., J.M. Orenstein, and E.O. Freed, Role of the Gag matrix domain in targeting human immunodeficiency virus type 1 assembly. J Virol, 2000. **74**(6): p. 2855-66.

113. Zhou, W. and M.D. Resh, Differential membrane binding of the human immunodeficiency virus type 1 matrix protein. J Virol, 1996. **70**(12): p. 8540-8.
114. Xia, Z. and Y. Liu, Reliable and global measurement of fluorescence resonance energy transfer using fluorescence microscopes. Biophys J, 2001. **81**(4): p. 2395-402.
115. Frost, S.D., et al., Antibody responses in primary HIV-1 infection. Curr Opin HIV AIDS, 2008. **3**(1): p. 45-51.
116. Jolly, C., I. Mitar, and Q.J. Sattentau, Adhesion molecule interactions facilitate human immunodeficiency virus type 1-induced virological synapse formation between T cells. J Virol, 2007. **81**(24): p. 13916-21.
117. Sol-Foulon, N., et al., ZAP-70 kinase regulates HIV cell-to-cell spread and virological synapse formation. EMBO J, 2007. **26**(2): p. 516-526.
118. Maddon, P.J., et al., HIV infection does not require endocytosis of its receptor, CD4. Cell, 1988. **54**(6): p. 865-74.
119. Stein, B.S., et al., pH-independent HIV entry into CD4-positive T cells via virus envelope fusion to the plasma membrane. Cell, 1987. **49**(5): p. 659-668.
120. Daecke, J., et al., Involvement of clathrin-mediated endocytosis in human immunodeficiency virus type 1 entry. J Virol, 2005. **79**(3): p. 1581-94.
121. Munk, C., et al., A dominant block to HIV-1 replication at reverse transcription in simian cells. Proc Natl Acad Sci U S A, 2002. **99**(21): p. 13843-8.
122. Jiang, J. and C. Aiken, Maturation-dependent human immunodeficiency virus type 1 particle fusion requires a carboxyl-terminal region of the gp41 cytoplasmic tail. J Virol, 2007. **81**(18): p. 9999-10008.
123. Murakami, T., et al., Regulation of human immunodeficiency virus type 1 Env-mediated membrane fusion by viral protease activity. J Virol, 2004. **78**(2): p. 1026-31.
124. Murakami, T. and E.O. Freed, Genetic evidence for an interaction between human immunodeficiency virus type 1 matrix and alpha-helix 2 of the gp41 cytoplasmic tail. J Virol, 2000. **74**(8): p. 3548-54.
125. Wyma, D.J., et al., Coupling of human immunodeficiency virus type 1 fusion to virion maturation: a novel role of the gp41 cytoplasmic tail. J Virol, 2004. **78**(7): p. 3429-35.
126. Pettit, S.C., et al., The p2 domain of human immunodeficiency virus type 1 Gag regulates sequential proteolytic processing and is required to produce fully infectious virions. J Virol, 1994. **68**(12): p. 8017-27.
127. Fassati, A. and S.P. Goff, Characterization of intracellular reverse transcription complexes of human immunodeficiency virus type 1. J Virol, 2001. **75**(8): p. 3626-35.
128. McDonald, D., et al., Visualization of the intracellular behavior of HIV in living cells. J. Cell Biol., 2002. **159**(3): p. 441-452.
129. Martin, N., et al., Virological synapse-mediated spread of human immunodeficiency virus type 1 between T cells is sensitive to entry inhibition. J Virol, 2010. **84**(7): p. 3516-27.
130. McClure, M.O., M. Marsh, and R.A. Weiss, Human immunodeficiency virus infection of CD4-bearing cells occurs by a pH-independent mechanism. EMBO J, 1988. **7**(2): p. 513-8.

131. Sanchez-San Martin, C., C.Y. Liu, and M. Kielian, Dealing with low pH: entry and exit of alphaviruses and flaviviruses. Trends Microbiol, 2009. **17**(11): p. 514-21.
132. Mervis, R.J., et al., The gag gene products of human immunodeficiency virus type 1: alignment within the gag open reading frame, identification of posttranslational modifications, and evidence for alternative gag precursors. J Virol, 1988. **62**(11): p. 3993-4002.
133. Spear, M., J. Guo, and Y. Wu, The trinity of the cortical actin in the initiation of HIV-1 infection. Retrovirology, 2012. **9**(1): p. 45.
134. Guo, J., et al., Spinoculation triggers dynamic actin and cofilin activity that facilitates HIV-1 infection of transformed and resting CD4 T cells. Journal of virology, 2011. **85**(19): p. 9824-9833.
135. Yoder, A., et al., HIV Envelope-CXCR4 Signaling Activates Cofilin to Overcome Cortical Actin Restriction in Resting CD4 T Cells. Cell, 2008. **134**(5): p. 782-792.
136. Vasiliver-Shamis, G., et al., Human Immunodeficiency Virus Type 1 Envelope gp120-Induced Partial T-Cell Receptor Signaling Creates an F-Actin-Depleted Zone in the Virological Synapse. J. Virol., 2009. **83**(21): p. 11341-11355.
137. Challenges, O., Quantitative four-dimensional tracking of cytoplasmic and nuclear HIV-1 complexes. Nature Methods, 2006. **3**: p. 817-824.
138. Lehmann, M., et al., Intracellular Transport of Human Immunodeficiency Virus Type 1 Genomic RNA and Viral Production Are Dependent on Dynein Motor Function and Late Endosome Positioning. Journal of Biological Chemistry, 2009. **284**(21): p. 14572-14585.
139. Nishi, M., et al., Requirement for microtubule integrity in the SOCS1-mediated intracellular dynamics of HIV-1 Gag. FEBS Letters, 2009. **583**(8): p. 1243-1250.
140. Murooka, T.T., et al., HIV-infected T cells are migratory vehicles for viral dissemination. Nature, 2012.
141. Dao, M., C.T. Lim, and S. Suresh, Mechanics of the human red blood cell deformed by optical tweezers (vol 51, pg 2259, 2003). Journal of the Mechanics and Physics of Solids, 2003. **53**(2): p. 493-494.
142. Henon, S., et al., A new determination of the shear modulus of the human erythrocyte membrane using optical tweezers. Biophysical Journal, 1999. **76**(2): p. 1145-1151.
143. Grover, S., R. Gauthier, and A. Skirtach, Analysis of the behaviour of erythrocytes in an optical trapping system. Optics Express, 2000. **7**(13).
144. Dharmadhikari, J., et al., Torque-generating malaria-infected red blood cells in an optical trap. Opt. Express, 2004. **12**(6): p. 1179-1184.
145. Mohanty, S.K., K.S. Mohanty, and P.K. Gupta, Dynamics of interaction of RBC with optical tweezers. Optics Express, 2005. **13**(12).